

Electronic Thesis and Dissertation Repository

11-12-2020 2:30 PM

Joint Wind and Ice Effects on Transmission Lines in Mountainous Terrain

Daniel Davalos Arriaga, *The University of Western Ontario*

Supervisor: Hangan, Horia M., *The University of Western Ontario*

A thesis submitted in partial fulfillment of the requirements for the Master of Engineering Science degree in Civil and Environmental Engineering

© Daniel Davalos Arriaga 2020

Follow this and additional works at: <https://ir.lib.uwo.ca/etd>



Part of the [Aerodynamics and Fluid Mechanics Commons](#), [Civil Engineering Commons](#), [Dynamics and Dynamical Systems Commons](#), and the [Structural Engineering Commons](#)

Recommended Citation

Davalos Arriaga, Daniel, "Joint Wind and Ice Effects on Transmission Lines in Mountainous Terrain" (2020). *Electronic Thesis and Dissertation Repository*. 7441.
<https://ir.lib.uwo.ca/etd/7441>

This Dissertation/Thesis is brought to you for free and open access by Scholarship@Western. It has been accepted for inclusion in Electronic Thesis and Dissertation Repository by an authorized administrator of Scholarship@Western. For more information, please contact wlsadmin@uwo.ca.

Abstract

Atmospheric icing on mountainous terrain can produce catastrophic damages to transmission lines when incoming particles impinge and accrete on the cable surface of the system. The first challenge in wind-ice loading is determining joint statistics of wind and ice accretion on transmission lines. This study analyzes the weather characteristics for a specific site of study using 15 years of historical data to use as inputs for ice accretion modeling. The joint wind and ice hazard is characterized by simulating 500 years of icing events from the fitted probability distributions of ice accretion and wind on ice velocities. The second challenge of wind and ice loading is to deal with the wind induced vibrations when the iced conductors present complex asymmetrical shapes. The vertical galloping, characterized by high amplitude and low frequency motions, produce extra tension to the transmission towers which is not considered in the Canadian standard (CSA-C22.3) for the design of wind and ice loads for overhead transmission lines. For the dynamic analysis, the Den Hartog's principle is applied to identify potential instabilities and the linear theory of free vibrations of a suspended cable is performed for the estimation of the extra tension produced by the free stream velocity acting on the one-degree-of-freedom iced conductor. The static and dynamic loading resulting from the present study are compared with the wind and ice design cases based on the Canadian standard (CSA-C22.3).

Keywords

Joint wind and ice hazard, Atmospheric icing, Probability distributions, Vertical galloping, Structural dynamics, Reliability based design

Summary for Lay Audience

When transmission lines are exposed to harsh weather conditions, such as strong winds and intense ice storms, the system may experience serious damage if it is not previously design to withstand these conditions. The ice may accrete on the cable surface of the system giving place to undesired behavior of the wire, potentially creating overloading which may lead to transmission line failures. Failures may produce economic losses, long blackouts, and unfortunately human deaths in the worst scenario. There is thus a need to conduct research of the wind and ice effects on transmission lines located in mountainous terrain. Although the effects of wind speed and atmospheric icing have been widely studied separately, little attention has been given to both acting simultaneously. For this reason, the present work attempts to reduce uncertainties when dealing with the joint wind and ice hazard, by quantifying its contribution to the total tension transmitted to the transmission towers. The resulting effects from the present study are compared with existing guidelines for the design of wind and ice loading on overhead transmission lines (The Canadian standard CSA-C22.3).

Co-Authorship Statement

Chapter two and chapter three of the present thesis will be submitted as individual manuscripts to the Journal of Wind Engineering and Industrial Aerodynamics for publication under the co-authorship of Davalos D., Jubayer C., and Hangan H.

Davalos D. conducted the literature review, and the data process and analysis. Davalos D. also produced the figures, tables, and results, and wrote the overall manuscript. Hangan H. and Jubayer C. recommended the literature review and helped with evaluating the results. Hangan H. and Jubayer C. also helped with reviewing both manuscripts. Hangan H. supervised the research and helped with the final discussions.

Acknowledgments

I would like to express my deepest gratitude to my supervisor Professor Horia M. Hangan for his invaluable advice and support. His extensive expertise and knowledge encouraged me throughout the completion of my master's studies. It is of my great pleasure and honour to be part of his research group.

My sincere gratitude to Consejo Nacional de Ciencia y Tecnologia (Conacyt), and Alianza para la Formacion e Investigacion en Infraestructura para el Desarrollo de Mexico (Alianza FiiDEM) for providing financial support. The financial support provided by the Department of Civil and Environmental Engineering at The University of Western Ontario is also greatly appreciated.

I would also like to express my sincere gratitude to my co-supervisor and co-author Dr. Jubayer Chowdhury for his support and guidance during my research project.

An acknowledgement is extended to Dr. Ayan Sadhu, Dr. Horia Hangan, and Dr. Gregory Kopp for their commitment and enthusiasm sharing their extensive knowledge in the courses I attended.

I would like to take the opportunity to express my gratitude to all my colleagues and friends from the Wind Engineering group with whom I share an office, especially to my good friends Kamran Shirzadeh, Andrea Ballestracci, Hiroaki Shoji, Federico Canepa, and Junayed Chowdhury, for the exchange of scientific thoughts and for the moments we shared during our stay at The University. A special thanks to my good friend Dr. Raul Sanchez, for sharing his thoughts about the second chapter of my thesis despite of his busy schedule as a Ph.D. candidate himself.

Lastly and foremost, my profound gratitude goes to my family. To my mother and sister Antonieta Arriaga and Paola Davalos, for their unconditional support during my professional studies, for teaching me to be brave, and for their significant contribution in every stage of my life. To Thalia Crocker, for bringing peace to my life, for her patience, for overcoming adversity with me, and for her encouraging words during my academic stay. To Mariano Arriaga, Cox, and my two little cousins, Elias and Max, for their invaluable support and wise advice since the first moment I arrived in Canada, and for the memorable moments we shared during my master's degree. To

Elena Arriaga, Mariana Galindez, Esteban Galindez, Jorge Arriaga, Jose Jorge Arriaga, and Manuel Gongora, for giving me strength whenever I was feeling discouraged. And to Nancy Mendoza, and Luis Castillo, for always be there for me.

Table of Contents

Abstract.....	ii
Summary for Lay Audience	iii
Co-Authorship Statement	iv
Acknowledgments.....	v
Table of Contents.....	vii
List of Tables	x
List of Figures	xi
List of Appendices.....	xiii
Nomenclature	xiv
1 Introduction.....	1
1.1 Ice accretion on wires	2
1.2 Wind induced vibrations	5
1.3 Types of atmospheric icing.....	7
1.4 Scope	9
1.5 Site of study.....	10
1.6 Organization of the thesis	10
1.7 References.....	11

2	Joint wind and ice hazard for transmission lines in mountainous terrain	15
2.1	Weather stations.....	16
2.2	Goodness of fit	20
2.3	Data analysis.....	21
2.3.1	Inverse Distance Weighted interpolations	22
2.3.2	K Nearest Neighbors Imputation	25
2.3.3	Artificial Neural Network	27
2.4	Ice accretion model.....	35
2.5	Probability distributions.....	39
2.6	Results and discussion.....	40
2.7	Conclusions.....	50
2.8	References.....	51
3	Vertical galloping on complex shapes of iced conductors	57
3.1	Ice profiles	58
3.1.1	Rime ice profile	58
3.1.2	Glaze ice profile.....	59
3.2	CFD Setup	61
3.3	Structural Analysis.....	66
3.3.1	Static loads	66

3.3.2	Natural Frequencies of the system.....	68
3.3.3	Galloping Conditions.....	70
3.3.4	Extra tension on the onset of galloping.....	72
3.4	Results and discussion.....	73
3.5	Conclusions.....	79
3.6	References.....	80
4	Conclusions and future work.....	83
4.1	Summary	83
4.2	Conclusions.....	84
4.3	Future work	87
4.4	References.....	88
	Appendices.....	90

List of Tables

Table 1.1. Characteristics of the different types of ice accretion on overhead transmission lines (El-Fashny, 2002).....	8
Table 2.1. Weather Stations selected from the pre analysis phase.	20
Table 2.2. Most popular activation functions (Afshar, 2016).	28
Table 2.3. Characteristics of the network.....	34
Table 2.4. Goodness of fit and probability distribution parameters.	42
Table 2.5. Information of the most severe storms. u_{max}) Maximum velocity presented during the evolution of the storm, u) Mean velocity presented, T) Mean temperature presented, p) Mean precipitation presented.....	44
Table 2.6. Wind and Gust velocities from physical and ANN analyses.....	44
Table 2.7. Distribution parameters and goodness of fit measured in terms of r) Correlation coefficient, MAE) Mean Absolute Error, MSE) Mean Square Error, RMSE) Root Mean Square Error.	45
Table 2.8. 50-year return levels for wind speed and ice accretion.	46
Table 2.9. Reliability levels and C1 and C2 combined values from the CSA-C22.3.	49
Table 3.1. Sensitivity analysis for the rime ice profile.	63
Table 3.2. Natural frequencies of the conductor.	70
Table 3.3. Galloping conditions analysis.	76
Table 3.4. Static and dynamic loads for the three profiles tested and three reliability levels.....	78
Table 3.5. Static loads calculated from the standard (CSA-C22.3) procedure.	79

List of Figures

Figure 1.1. 305 (kg/m) of rime ice accumulated on an overhead line in Norway the 18 th of April of 1961 (Makkonen, 2000).....	2
Figure 1.2. Cd and Cl curve with respect to the angle of attack for a non-circular profile (Den Hartog, 1932).....	6
Figure 1.3. a) Wet growth process and b) Dry growth process (Makkonen, 2000).	8
Figure 1.4. a) Location of the transmission line system and b) location of the highest elevated tower (from Google Earth).....	10
Figure 2.1. Top) All the weather stations in the MTI database (blue dots) and HE (small red circle). Bottom left corner) 50 km radius around HE, and Bottom right corner) 120 km radius around HE.	18
Figure 2.2. 16 selected weather stations after the pre analysis phase (MD < 30%).	19
Figure 2.3. Spatial trend and weather stations (blue dots) for the month of a) February ($L = 0.45$ °C/100 m), $r^2 = 0.80$, and b) March ($L = 0.59$ °C/100 m), $r^2 = 0.93$	24
Figure 2.4. Laps rate (L) per 100 m of elevation for each month.....	25
Figure 2.5. Precipitation data and its correlation with the nearby weather stations, $Prcp_n$, where n is the number of the weather stations indicated in Table 2.1.	26
Figure 2.6. Loss function gradient descent (Pereira & Borysov, 2019).	32
Figure 2.7. Architecture of the network.	34
Figure 2.8. a) Fitted Weibull distribution for wind speed historical records, b) Box plots for wind speed historical records, c) Fitted Normal distributions for temperature historical records, and d) Box plots for temperature historical records.	41

Figure 2.9. Ice density (ρ_i) and types of ice histogram based on the classifications reported in Table 1.1.....	44
Figure 2.10. a) Generalized Pareto PDF, b) Generalized Pareto CDF, c) Q-Q plot, and d) Theoretical return levels vs fitted Generalized Pareto return levels.....	45
Figure 2.11. a) Joint Frequency histogram and b) Joint Probability of Exceedance curve.....	47
Figure 2.12. Joint scatter plot for the historical and simulated data pairs.....	48
Figure 2.13. Hazard contours characterizing the joint wind and ice hazard.....	49
Figure 3.1. Rime ice profile (Poots & Skelton, 1995).....	59
Figure 3.2. a) S1 profile for $u = 10$ m/s, and $T = -10$ °C in semi wet growth conditions, and b) S2 profile for $u = 10$ m/s, and $T = -5$ °C in wet growth conditions (Fu et al., 2006).	60
Figure 3.3. Boundary Layer near the wall (Sijal, 2019).....	63
Figure 3.4. a) Boundary conditions and b) final mesh considered for the rime ice profile with a total of $\approx 60,000$ elements, $y^+ = 10$, average element quality = 0.97, and average skewness = 0.03.	64
Figure 3.5. Mesh metrics for the rime ice profile: a) Element Quality, and b) Cells Skewness....	65
Figure 3.6. Rotation of the ice profiles.	66
Figure 3.7. Selected ice accretion data pair for a 10 m/s wind gust velocity.....	68
Figure 3.8. Graphic representation of the non-zero roots of Equation (3.11).	70
Figure 3.9. Aerodynamic lift and drag coefficients for the different profiles tested.	75
Figure 3.10. Den Hartog's coefficient vs angle of attack for the three different ice profiles.....	75
Figure 3.11. Static and dynamic loads for the three profiles tested and three reliability levels.	78

List of Appendices

Appendix A: Figures supporting the lapse rate and the most intense icing events from Chapter 2	90
Appendix B: Figures of the mesh and metrics for S1 and S2 profiles from Chapter 3	100

Nomenclature

Abbreviations

ANN	Artificial Neural Network
CDF	Cumulative Density Function
CFD	Computational Fluid Dynamics
GPD	Generalized Pareto Distribution
HE	Highest Elevation
IDW	Inverse Distance Weighted interpolations
JCDF	Joint Cumulative Density Function
JCCDF	Joint Complementary Cumulative Density Function
JPDF	Joint Probability Density Function
KNNI	K Nearest Neighbour Imputation
MAE	Mean Absolute Error
MD	Missing Data
MPF	Modal Participation Factor
MSE	Mean Square Error
MTI	Ministry of Transportation and Infrastructure data base
PDF	Probability Density Function
RANS	Reynolds-Averaged and Navier-Stokes equations
RMSE	Root Mean Square Error
WRF	Weather Research and Forecast

Symbols

A	Area of the cable	m^2
-----	-------------------	-------

A_c	Tension transmitted to the transmission towers due to horizontal loads	kN
A_n	Specific amplitude	m
a	Scale parameter of the Weibull distribution	m/s
a_g	Den Hartog's coefficient	-
a_i	Radiation linearization constant	K ³
b	Bias	-
C_d	Drag coefficient	-
C_f	Skin friction coefficient	-
C_l	Lift coefficient	-
C_p	Specific heat of air	J/kg °C
C_w	Specific heat of water	J/kg °C
D	Diameter of the cable	m
d	Droplet median volume diameter	µm
d_c	Characteristic length of the iced conductor	m
d_i	Euclidean distance between weather stations and the site of interest	m
E	Elevation	masl
E_c	Modulus of elasticity of the cable	Pa
e_a	Saturation water vapor pressure at atmospheric temperature	mbar
e_s	Saturation water vapor pressure at 0 °C	mbar
f_n	Natural frequency	Hz
G_c	Combined wind factor	-
G_L	Span factor	-
g_t	Loss function gradient	-
H	Tension transmitted to the transmission towers due to vertical loads	kN
h	Heat transfer coefficient	W/m ² °C
I_u	Turbulence intensity	-
K	K Nearest Neighbour	-
K_n	Inertia parameter	-

k	Shape parameter of the Weibull distribution	-
L	Lapse rate	°C
L_e	Latent heat of evaporation at 0 °C	J/kg
L_f	Latent heat of fusion at 0 °C	J/kg
L_i	Length of the span	m
m_n	Modal mass	kg
m_s	Structural mass	kg
m_{tot}	Total mass considering cable and ice mass per unit length	kg/m
m_i	First moment related to the expected value	-
\widehat{m}_i	First moment biased corrected	-
P	Probability of an event occurring once every t years	%
P_i	Air pressure	mbar
p	Water precipitation rate	mm/h
R	Macklin's parameter	-
R_{ed}	Droplet Reynolds number	-
R_e	Reynolds number	-
R_{eq}	Radial ice accretion	cm
$R_{eq,t}$	t -year return period radial ice accretion	cm
r	Correlation coefficient	-
r_i	Recovery factor for viscous heating	-
S_c	Scruton number	-
s	Sag of the cable at the mid span	m
T	Atmospheric temperature	°C
t_s	Cable surface temperature	°C
U	The mode of extreme value distribution	m/s
u	Wind speed	m/s
u_o	Impact droplet velocity	m/s
u_{max}	Wind on ice velocity	m/s
u_{ref}	Reference wind speed	m/s

u_τ	Friction velocity	m/s
V_c	Critical wind velocity	m/s
V_t	t -year return period wind velocity	m/s
v	Total displacement of the line	m
v_i	Second moment related to the variance of the distribution	-
\hat{v}_i	Second moment biased corrected	-
v_n	Modal displacement of the line	m
W	Liquid water content	g/m ³
w	Weight	-
w_c	Mass per unit length of the cable	kg/m
y	First layer thickness	m
y^+	Non-dimensional height	-
z_o	Roughness length	m
z_{ref}	Reference height	m

Greek Symbols

α	Angle of attack	°
α_i	Control parameter of the IDW interpolations	-
α_1	Collision efficiency	-
α_2	Sticking efficiency	-
α_3	Accretion efficiency	-
β	Exponential decay rate	-
βL	Particular symmetric vertical modal component	-
γ	Angle between the impinging trajectory and the normal to the surface at a specified point	°
ε	Constant	10 ⁻⁸

ε_i	Ratio of molecular weights of dry air and water vapor	-
η	Learning rate	-
θ	Threshold parameter of the Generalized Pareto Distribution	cm
λ	Liquid fraction	-
μ	Absolute viscosity of air	kg/m s
ξ_a	Aerodynamic damping ratio	%
ξ_s	Structural damping ratio	%
ρ_a	Air density	kg/m ³
ρ_i	Ice density	kg/m ³
ρ_w	Water density	kg/m ³
σ	Scale parameter of the Generalized Pareto Distribution	cm
σ_i	Local fraction of the incoming particle	-
τ	Shape parameter of the Generalized Pareto Distribution	-
τ_w	Wall shear stress	kg/m s ²
φ	Langmuir parameter	-
φ_n	Mode shape	-
ψ	Updated parameters w and b	-
ω_n	Angular natural frequency	rad/s

Chapter 1

1 Introduction

The formation of different types of ice such as glaze, hard rime, and soft rime, can interfere with the normal operation of specific systems and produce catastrophic consequences in areas as diverse as aeronautic, automotive, and civil engineering. Atmospheric icing, or icing conditions, can be described as supercooled water droplets colliding with a surface creating an ice layer which modifies the original shape of the body under consideration and thus modifying the flow field around it (Janjua et al., 2018).

In the aeronautic industry, icing aircraft research started at the beginning of the last century aiming to understand the ice accretion behavior and its impact in the aircraft performance (Cao et al., 2018). Depending on the thickness of the ice layer, four categories of severity have been proposed: trace, light, moderate, and severe, where the first can be assumed not hazardous, and the last can lead to fatal accidents (William & Wayne, 2000). Several papers among the literature can be found proposing solutions and trying to understand the nature of the ice accretion process. Ice accretion and anti-icing mathematical models have been described by Saeed, (2002), where anti-icing heat requirements have been analyzed. A mixed ice accretion model, considering a combination of rime and glaze have been proposed by Janjua et al., (2018) to understand its effect on aircraft wings. Diebold et al., (2013) described and summarized research carried out throughout the years about ice accretion for two-dimensional airfoils and tried to highlight the importance of the three-dimensional flow field in ice formation.

In the automotive industry, recent efforts in the race to fully autonomous vehicles have encountered obstacles in countries where harsh weather is predominant. Fog, snow, heavy rain, and ice, impede LiDAR systems to work properly and advanced to the next level of autonomy (Filgueira et al., 2017; Rasshofer et al., 2011).

Civil engineering is historically the first area in which ice research has been conducted. The ice accretion mostly affects wired structures like transmission lines or cable-stayed bridges. During

an ice storm, the water droplets frozen on the wires can produce extra vertical load highly increasing the tension transmitted to the towers and overcome the original design loads and thus produce a failure. As a reference, the maximum ice load for transmission lines in history was recorded in Norway and had a magnitude of 305 (kg/m) (Makkonen, 2000). Another important consideration for atmospheric icing on transmission lines are the wind induced vibrations that the wire may experience when the ice deposit is not symmetric. The ice may accrete creating a crescent shape on the windward side of the wire modifying its circular geometric shape and experiencing aerodynamic lift which may lead to aerodynamic instabilities.



Figure 1.1. 305 (kg/m) of rime ice accumulated on an overhead line in Norway the 18th of April of 1961 (Makkonen, 2000).

1.1 Ice accretion on wires

Historically, atmospheric icing has been a big concern for civil engineers due to the uncertainties when calculating design loads for structures. For instance, in Quebec and Ontario, during the

winter of 1998, a severe ice storm without precedents in recent history produced the collapse of 1,300 power-line towers and 35,000 distribution towers leaving millions of people without electricity for weeks and severely affecting their lifestyles (Rossi, 2018). In Sweden in 1999, the power supply was interrupted for several hours in a 130-400 kv system due to ice accumulation on an insulator (Solangi, 2018). In 1990, 20 cm of radial ice accretion were reported in a 400 kv system located in the United Kingdom which produced several incidents and failures during the icing event (Solangi, 2018). In 2010 in Catalonia, where transmission lines are usually not design to withstand severe ice storms due to the low probability of the events, the extra vertical load produced by the ice accretion resulted in costly repairs which took six weeks to complete (Solangi, 2018).

Unlike wind speeds records, ice accretion is rarely available from weather stations or any other source of historical data where the registers might be consulted. This lack of historical records has led to different approaches to estimate the ice hazard on overhead transmission lines. The state-of-the-art of estimating icing on conductors can be classified into five groups: 1) mathematical modeling, 2) empirical observations, 3) experimental observations, 4) probabilistic mapping, and 5) deicing mechanisms (Pohlman & Landers, 1982). Research have mainly focused on the three first categories and several icing models can be found in literature. Methods such as those described in Makkonen, (1984), Makkonen, (1998), Makkonen, (2000), Jones, (1998), Pohlman & Landers, (1982), and Pezard, (1995), to name a few, have become popular and adopted by many structural engineers to estimate the ice thickness during icing conditions. Probabilistic mappings provide too general information and find their weak point when data for a specific site or particular topography is needed, such as high elevated terrain (Pohlman & Landers, 1982). Deicing mechanisms often find their limitations when the icing rate during heavy ice storms exceed their deicing rate capacity, and engineers cannot completely rely on the mechanisms employed (Pohlman & Landers, 1982).

McComber et al., (1983) performed tests in a refrigerated wind tunnel for different wind speed ranges and observed the ice accretion shape formed for the three different types of ice. They then estimated the resultant force from the vertical load, which is function of the ice weight, and the horizontal force, which is function of the wind speed. Krishnasamy & Kulendran, (1998) and

Hoffman, (1984) proposed methods that assume that only a certain percentage of the extreme wind velocity during non-icing conditions will be presented during the ice storm. They proposed a reduction factor for the extreme velocity and combined it with the extreme ice accretion to obtain the combined wind and ice loading. The National Standard of Canada for the design of overhead transmission lines (CSA-C22.3) proposes a similar method, where the resulting loads must be a combination of low probability ice accretion and high probability wind speed or vice-versa. Then, the highest load is selected as the design wind and ice load. The low probability event (of ice or wind speed) is related to its t (years) return period magnitude, while the high probability event is related to the average of the yearly maximum events (when historical data is available). However, the estimation of the design data pairs of wind speed and ice accretion for overhead transmission lines is still a matter of discussion. The presented methods assume the combined values where at least one of the two hazards is represented by its t return level, and the other is strongly related with extreme occurrences. This assumption has been found to be overly conservative in recent studies where the joint hazards have been probabilistically characterized (Rosowsky & Wang, 2014; Sinh et al., 2016, 2019). Sinh et al., (2016) presented a methodology to characterize the joint wind and ice hazard during freezing rain by creating a superstation data base from observed freezing events of 8 weather stations in the Midwestern United States. They used hourly wind speed and precipitation records to simulate glaze ice accretion (type of ice formed during freezing rain) with the model described in Jones, (1998). They then presented a more sophisticated model by modeling 1000 years of temperature, wind speed, precipitation rate and ice accretion (Sinh et al., 2019). Once again, they concluded that the assumption of considering a t return level event for one of the variables may be conservative. Rosowsky & Wang, (2014) characterized the joint wind and snow hazard by modelling 10000 years of snow and wind time histories in Albany, New York. Their analysis concluded that the joint wind-snow hazard is overestimated in structural design codes. Nevertheless, these analyses were not performed for mountainous areas, which is the characteristic topography of the site of interest of the present thesis. For this reason, and because of the uncertainties described before when dealing with joint hazards in structural design codes and standards, the necessity of conducting research to characterize the joint wind and ice hazard in complex terrain is justified.

1.2 Wind induced vibrations

Wind induced vibrations will occur when the ice accreted on the wires forms an asymmetric shape increasing the risk of instabilities due to the presence of aerodynamic lift and thus increasing the tension on the tower supports. The dynamic effects on iced conductors are difficult to characterize and are usually not taken into consideration in codes or standards for the design of overhead transmission lines. Instead, overly conservative data pairs of wind speed and ice accretion are proposed assuming a radial ice deposit aiming to cover the dynamic effects of the wind induced vibrations. These vibrations can be critical for the system when motion is induced by a certain wind speed and angle of attack, creating damages that can vary from conductor strand burn in most of the cases, to cascade failure of the system (Lilien et al., 2005). The dynamic characteristics of the motion can be grouped into three categories: 1) small amplitude and high frequency, 2) small amplitude and moderate frequency, and 3) high-amplitude and low frequency (Borna et al., 2012). The first and second category can be referred as aeolian vibrations and are induced by vortex shedding phenomena. Aeolian vibrations are motions with frequencies in the range of 3 – 100 Hz and amplitudes that reach conductor diameter in the range of its lower frequency (Borna et al., 2012; Guerard et al., 2011). The third category is known as galloping, and is a self-excited vibration produced by an unbalance between the structural and aerodynamic damping (Wang & Lou, 2009). Galloping was first explored by Den Hartog in 1932, when he introduced a single-degree-of-freedom mechanism by observing the change in the aerodynamic lift during or after an icing event (Den Hartog, 1932). When the effect of the negative slope of the lift curve with respect to the angle of attack is greater than the damping effects of the drag, the instability may occur (Den Hartog, 1932). This statement can be mathematically observed in Equation (1.1) and graphically in Figure 1.2.

$$a_g = C_d + \frac{dC_l}{d\alpha} \quad (1.1)$$

where a_g is the Den Hartog's coefficient, C_d is the drag coefficient, C_l is the lift coefficient, and α is the angle of attack of the free stream velocity with respect to the cross section of the cable.

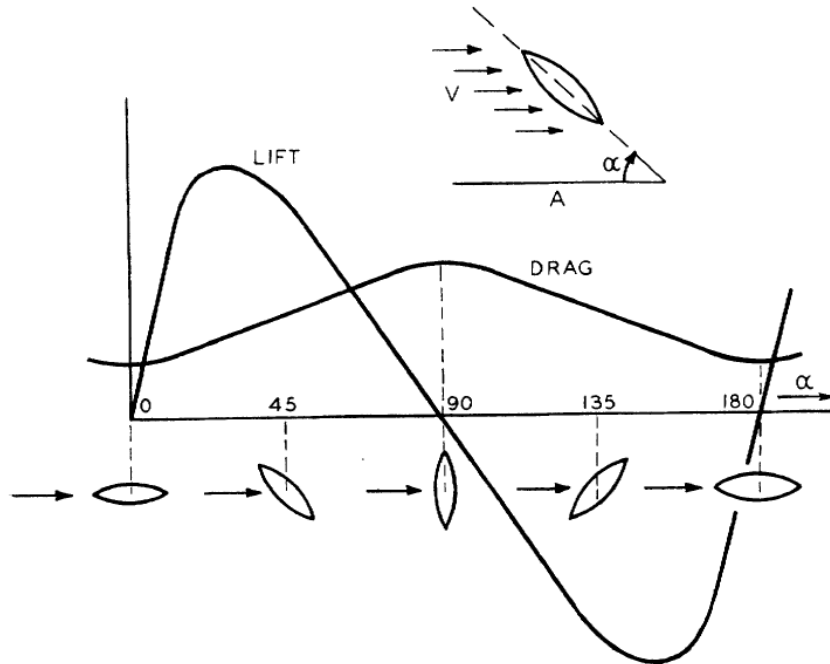


Figure 1.2. C_d and C_l curve with respect to the angle of attack for a non-circular profile (Den Hartog, 1932).

Several models have been proposed since the first approximation to the galloping proposed by Den Hartog. A two-degree-of-freedom system was proposed by Macdonald & Larose, (2008) to identify the range of velocities and angles of attack which causes galloping for an inclined cable of a cable-stayed bridge. Their model allowed them to identify the minimum requirements for the structural damping within the critical Reynolds number range to mitigate galloping. Gjelstrup & Georgakis, (2011) proposed a quasi-steady three-degree-of-freedom system for the determination of aerodynamic instabilities on iced conductors. Their proposed model allowed them to identify instabilities on the onset of galloping and could estimate the special instability cases of the Den Hartog galloping, drag crisis, and dry inclined cable galloping.

It is pertinent to mention that the identification of galloping depends on the behavior of the aerodynamic lift and drag coefficients and thus identifying the shape of the iced conductor is an important step of the process. The ice shape accreted on wires during an icing event depends on

a variety of factors such as wind speed, temperature, droplet size, liquid water content, and area of the cable, among others (Fu et al., 2006; Makkonen, 2000).

1.3 Types of atmospheric icing

Atmospheric icing can be classified into precipitation icing, in-cloud icing and hoarfrost (Pohlman & Landers, 1982). Precipitation icing is normally caused by freezing rain and the impinging water droplets are normally larger compared to in-cloud icing (Pohlman & Landers, 1982). The characteristic type of ice formation due to freezing rain is called glaze ice and its characteristics can be observed in Table 1.1. Note that Table 1.1 intends to give general information of the most common conditions where each type of ice have been observed and is not a strict rule that will always be fulfilled. For example, although glaze ice normally occurs within the range of temperatures between 0°C and -3°C, it is also probable to occur at considerably lower temperatures in the order of -20°C and as high as 5°C (Pohlman & Landers, 1982). For in-cloud icing, the resulting type of ice is normally rime, although glaze ice may also occur with less frequency. Rime ice can be divided into two subcategories named soft rime and hard rime (Pohlman & Landers, 1982). This type of process is characteristic of mountainous areas and are particularly dangerous for transmission line systems due to its frequent occurrence (Rossi, 2018). Hoarfrost is characterized for white ice crystals formation obtained by sublimation of the water vapor in the atmosphere (Rossi, 2018). Since the water vapor in the air is normally low at temperatures bellow the freezing point, hoarfrost rarely produce damages to the system (Pohlman & Landers, 1982).

The maximum rate of icing due to the water droplets colliding with the cable surface is determined by the flux density of these droplets (Makkonen, 2000). When the heat flux from the accretion is too small to cause instantaneous freezing of the droplets at the time of collision, part of the mass flux is lost from the surface by run-off (Makkonen, 2000). In such case, a liquid layer exists on the surface of the ice accretion and the droplets freeze beneath the layer (Makkonen,

2000). Such process is called wet growth, and the resultant ice type is glaze. Figure 1.3a shows the wet growth process schematically.

On the other hand, when there is no liquid layer on the surface, the growth process is dry (Figure 1.3b), and the resultant ice may be hard or soft rime, depending on weather characteristics such as temperature and wind speed, as it can be observed in Table 1.1. Depending on the growth process, one could expect different ice profiles due to the ice accretion. The ice profile, as previously mention, will have great influence in the flow field around the cable and thus in the aerodynamic coefficients for stability analysis. The ice shapes and their characteristics used in the present work for the estimation of instabilities will be further justified and described.

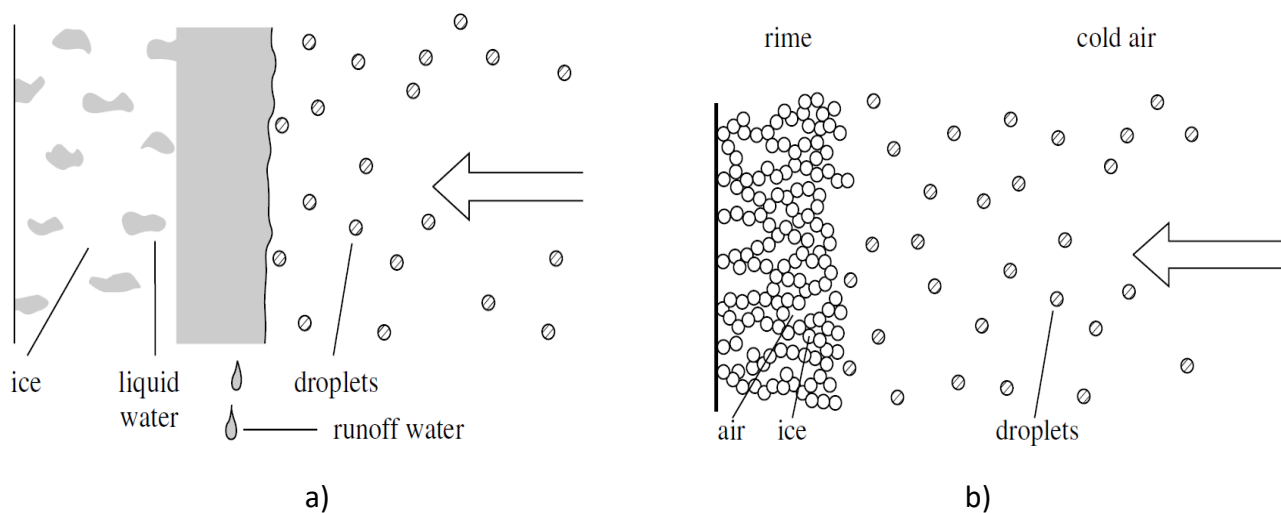


Figure 1.3. a) Wet growth process and b) Dry growth process (Makkonen, 2000).

Table 1.1. Characteristics of the different types of ice accretion on overhead transmission lines (El-Fashny, 2002).

Characteristics	Soft Rime	Hard Rime	Glaze
Density (kg/m^3)	<600	600 - 900	900
Adhesion	Medium	Strong	Very Strong
Appearance	Whitish crusty snow forming needles	Hard ice, white and opaque	Icicles and smooth transparent ice
Temperature ($^{\circ}C$)	-5 to -25	-3 to -8	0 to -3
Wind Speed (m/s)	1 to 5	5 to 10	0 to 20

1.4 Scope

The present work first attempts to characterize the joint hazard where limited data of weather characteristics is available. Historical data from 16 surrounding weather stations are used to estimate hourly wind speed, temperature, and precipitation rate at the site of interest. The techniques to estimate each variable depends on the level of complexity of its prediction. The Inverse Distance Weighting (IDW) interpolation method is used to estimate hourly temperature data, the K Nearest Neighbors Imputation algorithm (KNNI) is performed for the estimation of hourly precipitation rate, and a forward-back propagation Artificial Neural Network (ANN) is trained and tested for hourly wind speed predictions. The described weather characteristics are then used as inputs for the ice accretion modelling.

The ice accretion model used in the present thesis is the one described in Makkonen, (2000), which is detailed in section 2.4. The mentioned model outputs the thickness of the ice deposit, ice density, and ice mass per unit length. The wind speed records are then fitted to a Weibull Distribution and the ice accretion is fitted to a Generalized Pareto Distribution. Five hundred years of simulated records using the inverse of their CDFs are obtained. The Joint Probability Density Function (JPDF), Joint Cumulative Density Function (JCDF), and hazard contours are built from the data pairs resulting from the analyses described to characterize the joint hazard for this specific site of study.

For the dynamic analysis, both rime and glaze ice profiles are assumed based on the outputs from the ice accretion model. Lift and Drag coefficients are obtained from steady state CFD simulations using RANS $k - \omega$ SST turbulence model due to its good performance near the wall. The Den Hartog, (1932) principle is employed for identifying the critical range where instabilities may occur and the linear theory of free vibrations is used to transfer the loads acting on a one-degree-of-freedom system produced on the onset of vertical galloping to the transmission tower. The total load is then calculated considering both the static conditions estimated in the first part of this research and the extra tension produced by the dynamic effects. A comparison with the procedure described in the Canadian Standard (CSA-C22.3) for the design of wind and ice loading on overhead transmission lines is carried out.

1.5 Site of study

The transmission line system for the present study is located over complex terrain on Cascade Creek, in the proximity of Stewart, British Columbia, Canada (Figure 1.4a). It consists of a total of 37 towers, 10 km long and 138 kV. The towers are single circuit single pole Y-frame steel structure, and the conductors are single aluminum clad steel wire with a diameter of 23.55 mm. The present study focuses on the weather characteristics and analysis of the highest elevated tower, which is located at 1485 masl (Figure 1.4b). At that elevation, the system is exposed to harsh weather conditions, characterized by strong wind gusts and large accumulations of atmospheric icing (Rossi et al., 2020).

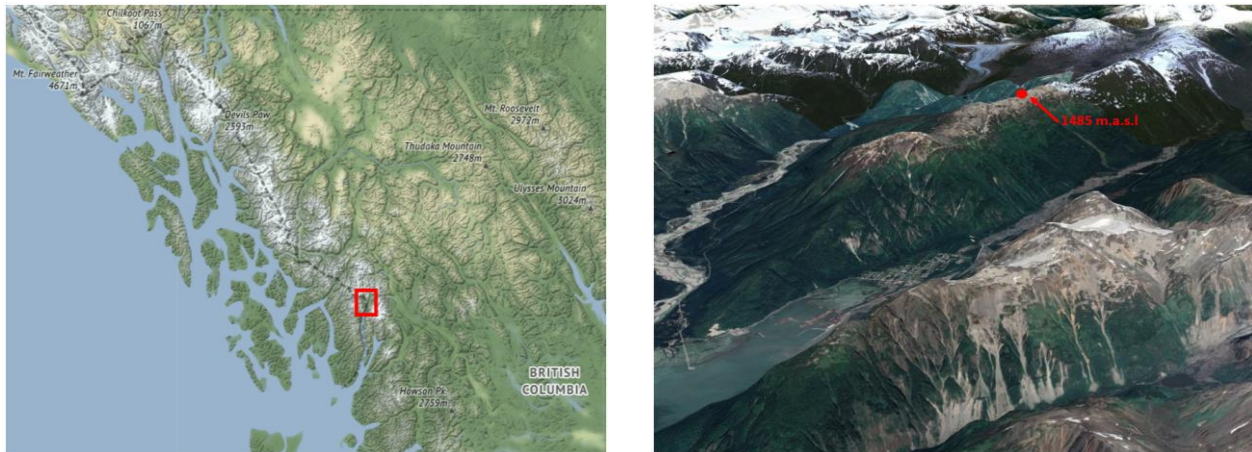


Figure 1.4. a) Location of the transmission line system and b) location of the highest elevated tower (from Google Earth).

1.6 Organization of the thesis

The present work follows the integrated article format as per thesis submission requirement of The University of Western Ontario. The articles to be submitted to the Journal of Wind Engineering and Industrial Aerodynamics are described in Chapter 2 and Chapter 3, respectively.

Chapter 1 provides an introduction of iced conductors and reviews the main studies related to the problem of ice accretion on overhead transmission lines. The literature review of wind induced vibrations is also presented. In addition, the site of study and the scope of this work are introduced to the reader.

Chapter 2 presents the data analysis at the site location considering the 16 surrounding weather stations. The ice accretion model is performed in this chapter. The joint wind and ice hazard is probabilistically characterized considering a radial ice accretion and a comparison with the reliability levels proposed by the Canadian Standard (CSA-C22.3) is made.

Chapter 3 describes the aerodynamic analysis for complex shapes of iced conductors. The stability analysis is performed based on Den Hartog's criterion for vertical galloping, and the tension transmitted to the tower considering both the static effects from Chapter 2 and dynamic effects produced on the onset of galloping is presented. The corroborative results from Chapter 2 and Chapter 3 are compared with the wind and ice design cases from the Canadian Standard (CSA-C22.3).

Chapter 4 provides a summary of the present thesis, the overall conclusions, and recommendations for further research.

1.7 References

Borna, A., Habashi, W. G., & McClure, G. (2012). Numerical Study of Influence of Ice Location on Galloping of an Iced Conductor. *Advances in Civil, Environmental, and Materials Research*

Cao, Y., Tan, W., & Wu, Z. (2018). Aircraft icing: An ongoing threat to aviation safety. *Aerospace Science and Technology*, 75, 353–385. <https://doi.org/10.1016/j.ast.2017.12.028>

Den Hartog, J. P. (1932). Transmission Line Vibration Due to Sleet. *Transactions of the American Institute of Electrical Engineers*, 51(4), 1074–1076. <https://doi.org/10.1109/T-AIEE.1932.5056223>

- Diebold, J. M., Broeren, A. P., & Bragg, M. (2013, June 24). Aerodynamic Classification of Swept-Wing Ice Accretion. *5th AIAA Atmospheric and Space Environments Conference*. 5th AIAA Atmospheric and Space Environments Conference, San Diego, CA. <https://doi.org/10.2514/6.2013-2825>
- Filgueira, A., González, H. J., Lagüela, S., Díaz-Vilariño, L., & Arias, P. (2017). Quantifying the influence of rain in LiDAR performance. *Measurement*, *95*, 143–148. <https://doi.org/10.1016/j.measurement.2016.10.009>
- Fu, P., Farzaneh, M., & Bouchard, G. (2006). Two-dimensional modelling of the ice accretion process on transmission line wires and conductors. *Cold Regions Science and Technology*, *46*(2), 132–146. <https://doi.org/10.1016/j.coldregions.2006.06.004>
- Gjelstrup, H., & Georgakis, C. T. (2011). A quasi-steady 3 degree-of-freedom model for the determination of the onset of bluff body galloping instability. *Journal of Fluids and Structures*, *27*(7), 1021–1034. <https://doi.org/10.1016/j.jfluidstructs.2011.04.006>
- Guerard, S., Godard, B., & Lilien, J.-L. (2011). Aeolian Vibrations on Power-Line Conductors, Evaluation of Actual Self Damping. *IEEE Transactions on Power Delivery*, *26*(4), 2118–2122. <https://doi.org/10.1109/TPWRD.2011.2151211>
- Hoffman, F. A. (1984). *Ice loading of transmission lines*. Sargent and Lundy 8th Biennial Transmission and Substation Conference, Chicago, IL.
- Janjua, Z. A., Turnbull, B., Hibberd, S., & Choi, K.-S. (2018). Mixed ice accretion on aircraft wings. *Physics of Fluids*, *30*(2), 027101. <https://doi.org/10.1063/1.5007301>
- Jones, K. F. (1998). A simple model for freezing rain ice loads. *Atmospheric Research*, *46*(1–2), 87–97. [https://doi.org/10.1016/S0169-8095\(97\)00053-7](https://doi.org/10.1016/S0169-8095(97)00053-7)
- Krishnasamy, S., & Kulendran, S. (1998). Combined wind and ice loads from historical extreme wind and ice data. *Atmospheric Research*, *46*(1–2), 123–129. [https://doi.org/10.1016/S0169-8095\(97\)00055-0](https://doi.org/10.1016/S0169-8095(97)00055-0)

- Lilien, J.-L., Van Dyke, P., Asselin, J.-M., Farzaneh, M., Halsan, K., Havard, D., Hearnshaw, D., Laneville, A., Mito, M., Rawlins, C. B., St-Louis, M., Sunkle, D., & Vinogradov, A. (2005). *State of the art of conductor galloping*. Task Force B2.11.06.
- Macdonald, J. H. G., & Larose, G. L. (2008). Two-degree-of-freedom inclined cable galloping— Part 1: General formulation and solution for perfectly tuned system. *Journal of Wind Engineering and Industrial Aerodynamics*, 96(3), 291–307. <https://doi.org/10.1016/j.jweia.2007.07.002>
- Makkonen, L. (1984). Modeling of ice accretion on wires. *Journal of Applied Meteorology and Climatology*, 23, 929–939.
- Makkonen, L. (1998). Modeling power line icing in freezing precipitation. *Atmospheric Research*, 46(1–2), 131–142. [https://doi.org/10.1016/S0169-8095\(97\)00056-2](https://doi.org/10.1016/S0169-8095(97)00056-2)
- Makkonen, L. (2000). Models for the growth of rime, glaze, icicles and wet snow on structures. *Philosophical Transactions of the Royal Society of London. Series A: Mathematical, Physical and Engineering Sciences*, 358(1776), 2913–2939. <https://doi.org/10.1098/rsta.2000.0690>
- McComber, P., Morin, G., Martin, R., & Vo Van, L. (1983). Estimation of combined ice and wind load on overhead transmission lines. *Cold Regions Science and Technology*, 6(3), 195–206. [https://doi.org/10.1016/0165-232X\(83\)90042-3](https://doi.org/10.1016/0165-232X(83)90042-3)
- National Standard of Canada, (2010). *Design criteria of overhead transmission lines (CAN/CSA-C22.3)*. Ontario, Canada
- Pezard, J. (1995). A method to estimate icing loads on overhead lines. *Atmospheric Research*, 36(3–4), 303–310. [https://doi.org/10.1016/0169-8095\(94\)00047-H](https://doi.org/10.1016/0169-8095(94)00047-H)
- Pohlman, J., & Landers, P. (1982). Present State-of-the-Art of Transmission Line Icing. *IEEE Transactions on Power Apparatus and Systems*, PAS-101(8), 2443–2450. <https://doi.org/10.1109/TPAS.1982.317605>

- Rasshofer, R. H., Spies, M., & Spies, H. (2011). Influences of weather phenomena on automotive laser radar systems. *Advances in Radio Science*, 9, 49–60. <https://doi.org/10.5194/ars-9-49-2011>
- Rosowsky, D. V., & Wang, Y. (2014). Joint Wind-Snow Hazard Characterization for Reduced Reference Periods. *Journal of Performance of Constructed Facilities*, 28(1), 121–127. [https://doi.org/10.1061/\(ASCE\)CF.1943-5509.0000385](https://doi.org/10.1061/(ASCE)CF.1943-5509.0000385)
- Rossi, A. (2018). *Wind tunnel modelling of snow and ice effects on transmission lines*. Technical University of Denmark.
- Saeed, F. (2002). State-of-the-Art Aircraft Icing and Anti-Icing Simulation. *Journal of Archives and Records Association*, 2000(25), 8.
- Sinh, H. N., Lombardo, F. T., & Letchford, C. (2019). Multivariate simulation for assessing the joint wind and ice hazard in the United States. *Journal of Wind Engineering and Industrial Aerodynamics*, 184, 436–444. <https://doi.org/10.1016/j.jweia.2018.12.012>
- Sinh, H. N., Lombardo, F. T., Letchford, C. W., & Rosowsky, D. V. (2016). Characterization of Joint Wind and Ice Hazard in Midwestern United States. *Natural Hazards Review*, 17(3), 04016004. [https://doi.org/10.1061/\(ASCE\)NH.1527-6996.0000221](https://doi.org/10.1061/(ASCE)NH.1527-6996.0000221)
- Solangi, A. R. (2018). *Icing Effects on Power Lines and Anti-icing and De-icing Methods* [Monograph]. The Arctic University of Norway.
- Wang, X., & Lou, W.-J. (2009). *Numerical Approach to galloping of Conductor*. The Seventh Asia-Pacific Conference on Wind Engineering, Taipei, Taiwan.
- William, M. L., & Wayne, R. S. (2000). The state-of-the-art knowledge for icing accidents for general aviation aircraft. *Journal of Air Law and Commerce*, 719, 32.

Chapter 2

2 Joint wind and ice hazard for transmission lines in mountainous terrain

This chapter presents the joint characterization of the wind and ice hazard on overhead transmission lines. The site of study described in section 1.5 will be referred as HE in the present thesis. An analysis of 16 weather stations surrounding HE is carried out. Three different algorithms for the estimation of temperature, wind speed, and precipitation rate at HE are performed using the data from the pre analyzed weather stations. The ice accretion model is performed taking into consideration the output from these algorithms. Fifteen years of historical hourly data pairs of wind speed and ice accretion are obtained after the ice accretion modelling. Five hundred years of data pairs are simulated in addition to the historical data. The wind speed simulated records are generated based on the Weibull Cumulative Distribution Function (CDF) while the Generalized Pareto CDF is used for the ice accretion simulation. The extreme wind speed data is fitted against Gumbel Probability Distribution Function (PDF), while the ice accretion extreme values are fitted with Generalized Pareto distribution. Joint wind and ice PDF (JPDF) and CDF (JCDF) are generated from the historical and simulated records and hazard contours are drawn. The results are then compared with the combined wind and ice values proposed in the CSA-C22.3 standard for different reliability levels.

The ice accretion model considered here is the one described in Makkonen, (2000), for the estimation of rime and glaze. The model takes several atmospheric characteristics as inputs. The supercooled water droplets trajectories must be taken into consideration for the estimation of the collision efficiency on the conductor. In their seminal work Langmuir & Blodgett, (1946) developed mathematical equations of droplet motion in the airflow around circular cylinders. Later, Finstad et al., (1988) related empirically the water droplet trajectories and thus the collision efficiency to the free stream velocity and the water droplet median volume diameter.

The empirical fit described in Finstad et al., (1988) is considered in this thesis. Temperature data is needed for the calculations of the accretion efficiency or freezing fraction. This parameter will dictate the type of ice formation on the wire. Its calculation can be obtained by solving numerically the heat balance of icing surface equation (Makkonen, 1984, 2000). Precipitation data is needed for the estimation of the liquid water content (W), which is another parameter for the ice accretion rate. Here, the empirical relationship between precipitation and water content presented by Best, (1950) was taken into consideration.

2.1 Weather stations

The first step of this project consisted of the pre analysis of the weather stations with enough historical data (i.e. less than 30% of missing data (MD)) for the estimation of three variables: 1) wind speed (u [m/s]), 2) temperature (T [°C]), and 3) hourly water precipitation rate (p [mm]). The data were taken from the Ministry of Transportation and Infrastructure (MTI) data base of British Columbia (<https://prdoas3.pub-apps.th.gov.bc.ca/saw-paws/weatherstation>). The data base contains 2-minute average velocities measured at the top of the hour. Although they may not be stationary, the velocities were assumed as hourly measured for the ice accretion model (Subsection 2.4) and converted to 3-second gust wind velocities for the joint hazard analysis (Subsection 2.6). All the weather stations available from the MTI data base were localized and are shown in Figure 2.1. A first radius (R_1) of 50 km around HE was drawn and a first attempt to estimate weather characteristics with the stations located within R_1 was conducted. However, some stations did not fulfill the condition of MD < 30%, or one of the variables were not found (i.e. the station measurements included wind speed and temperature but not precipitation data). A second radius (R_2) of 120 km was drawn and stations within the R_2 were included. Measurements were found to fulfill the MD < 30% condition in almost all the stations from 2005 to 2020. Before 2005, stations with MD > 50% were frequently found because the measurements were not registered hourly, or due to different techniques of data collecting at that time. For these reasons, the analysis was limited to the time series between 2005 and 2020. The stations were then cleaned of physically impossible values such as $T = -1000$ °C, $u = 1000$ m/s, or $p =$

1000 mm/h, for example, and these values were assumed as MD. In all cases, these kinds of values represented a very low percentage of the total data and did not modify the MD < 30% condition. Figure 2.2 shows all the stations that were selected in the pre analysis phase for the estimation of the weather characteristics at HE. Table 2.1 summarizes relevant information about the selected weather stations. From the table, some observations can be made. Temperature data is available at all the weather stations and with very low percentage of MD. Wind speed hourly records could be found in thirteen of the sixteen analyzed weather stations with higher MD compared with the temperature. Nevertheless, the average MD is 4.10% which is still very acceptable. Precipitation data was only found in seven out of the sixteen weather stations analyzed. It was observed that the lack of precipitation data correlates with the stations above 540 m of altitude. This tends to be a general problem for the northern part of Canada and specially in high elevated terrain where the water precipitation amounts are very difficult to measure (Mekis & Hogg, 1999; Smithson et al., 2002).

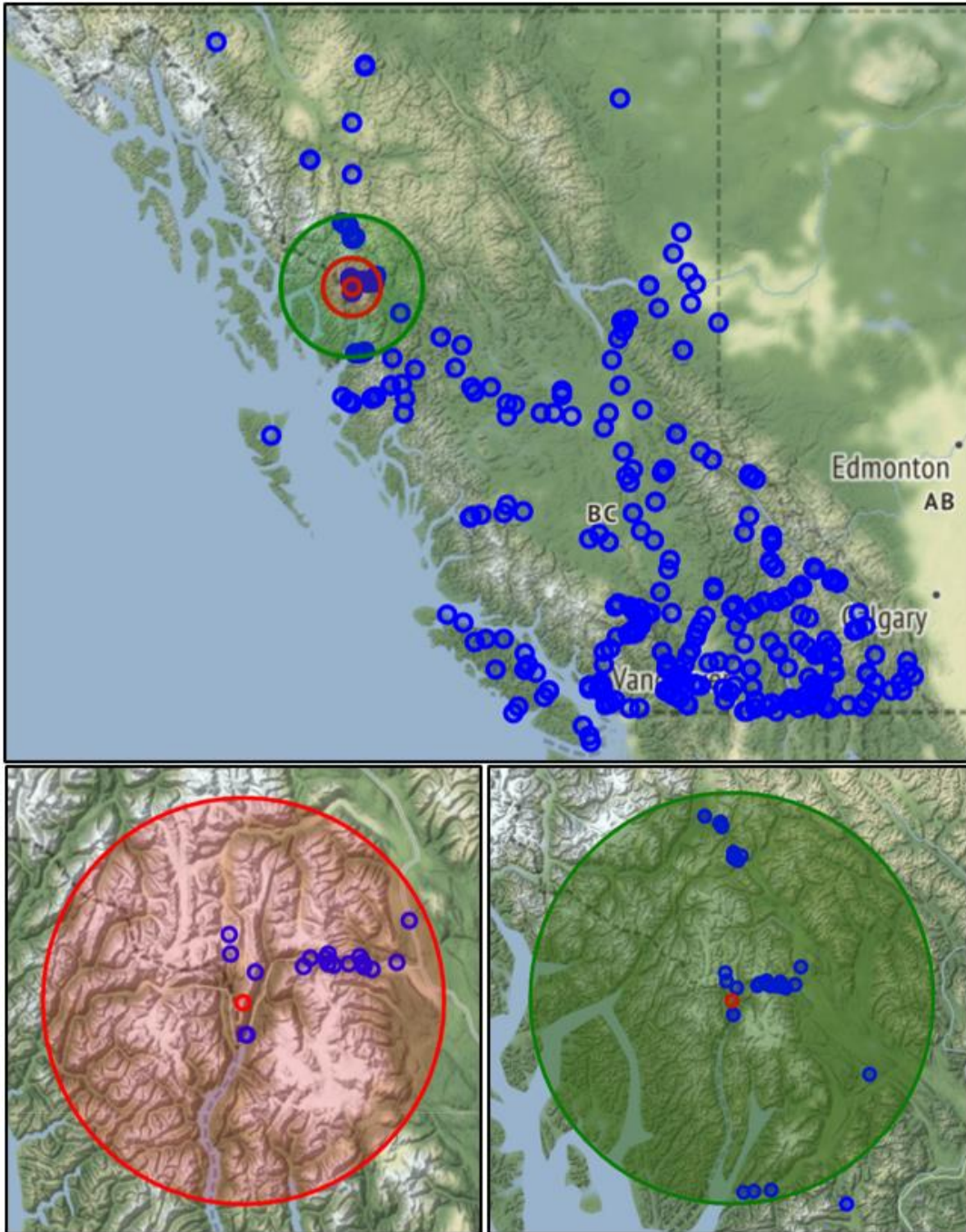


Figure 2.1. Top) All the weather stations in the MTI database (blue dots) and HE (small red circle). Bottom left corner) 50 km radius around HE, and Bottom right corner) 120 km radius around HE.

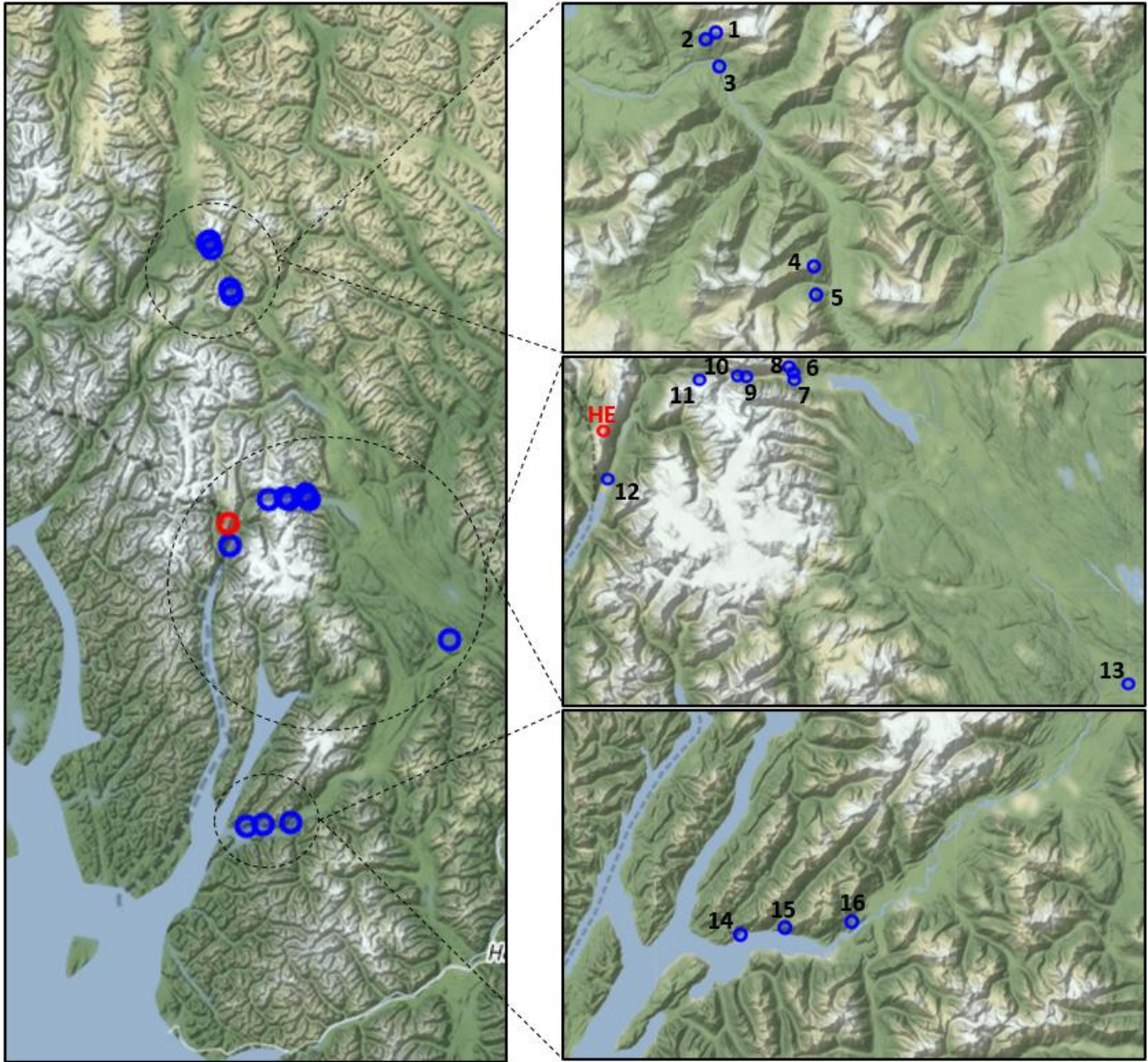


Figure 2.2. 16 selected weather stations after the pre analysis phase (MD < 30%).

Table 2.1. Weather Stations selected from the pre analysis phase.

Code	Label	Name	LAT	LONG	E (m)	Years	<i>p</i> (mm) (% MD)	<i>u</i> (m/s) (% MD)	<i>T</i> (°C) (% MD)
53127	1	Gamma High	56.95083	-130.095	1540	09 - 20	(--)	(2.99)	(3.02)
53123	2	Gamma	56.94667	-130.10694	1175	05 - 20	(--)	(10.77)	(7.43)
53126	3	Carl's Corner	56.92867	-130.0905	504	07 - 20	(3.95)	(--)	(3.46)
53128	4	Revision	56.79544	-129.97519	1500	09 - 20	(--)	(2.73)	(3.67)
53122	5	Snowbank Mid	56.77667	-129.97253	1065	05 - 20	(--)	(5.00)	(1.07)
51123	6	Windy Point Lower	56.11017	-129.51522	1035	05 - 17	(--)	(2.64)	(3.40)
51126	7	Endgoal	56.09987	-129.51218	370	05 - 20	(6.03)	(3.38)	(1.92)
51124	8	Windy Point Upper	56.12	-129.52642	1490	05 - 20	(--)	(2.37)	(1.91)
51128	9	Kettle Hole	56.10347	-129.63297	440	05 - 20	(3.61)	(--)	(2.18)
51127	10	Summit Sluff Wind	56.10631	-129.65389	540	05 - 20	(--)	(1.91)	(1.81)
51125	11	Disraeli	56.09972	-129.75167	2000	05 - 20	(--)	(8.16)	(2.73)
51129	12	Stewart	55.94808	-129.98264	15	05 - 20	(8.81)	(6.21)	(6.47)
51191	13	Cranberry Junction	55.63222	-128.67278	356	05 - 20	(1.48)	(0.51)	(0.19)
52522	14	Iknouk Road	55.00186	-129.88126	30	10 - 20	(2.63)	(--)	(0.33)
52521	15	Iknouk	55.01033	-129.77636	862	05 - 20	(--)	(6.64)	(6.62)
52591	16	Grizzly Hill	55.01849	-129.61817	120	15 - 20	(0.21)	(0.02)	(0.27)
HE	HE	Site of study	56.02095	-129.99366	1485	-	-	-	-

2.2 Goodness of fit

In a previous study, weather analysis at the same site of interest as in the present study was performed (Agustsson & Nygaard, 2016). The authors estimated 20 years (1995 – 2015) of hourly weather characteristics by performing a Weather Research and Forecast (WRF) model for the location of the 37 towers that form the transmission line system, including HE. The present work,

as mentioned in the past section, attempts to obtain the weather characteristics at HE by using historical the data from the 16 surrounding weather stations as main source. For validation purposes, the accuracy of the predicted values from the analyses described in the next subsection is measured by their goodness of fit with the results from the WRF model. In this thesis, the Mean Absolute Error (MAE), the Mean Square Error (MSE), the Root Mean Square Error (RMSE), and the correlation coefficient (r) are used as quantitative measures of comparison (El-Fashny, 2002).

$$MAE = \frac{1}{n} \sum_{i=1}^n |x_i - y_i| \quad (2.1)$$

$$MSE = \frac{1}{n} \sum_{i=1}^n (x_i - y_i)^2 \quad (2.2)$$

$$RMSE = \sqrt{\frac{1}{n} \sum_{i=1}^n (x_i - y_i)^2} \quad (2.3)$$

$$r = \frac{\sum_{i=1}^n (x_i - \bar{x})(y_i - \bar{y})}{[\sum_{i=1}^n (x_i - \bar{x})^2 \sum_{i=1}^n (y_i - \bar{y})^2]^{\frac{1}{2}}} \quad (2.4)$$

where x_i is the WRF observation, y_i is the predicted value, and n is the number of total observations.

2.3 Data analysis

Three different techniques were employed for the estimation of the weather characteristics at HE. In this study, the Inverse Distance Weighted (IDW) interpolation method was performed for hourly temperature estimation, the K Nearest Neighbors Imputation (KNNI) method was used for

precipitation, and a forward-back propagation Artificial Neural Network (ANN) was used for wind speed predictions. The reasons of the different techniques employed are explained in the following subsections.

2.3.1 Inverse Distance Weighted interpolations

Inverse Distance Weighted (IDW) is a spatial interpolation model based on the assumption that the closer a station is, the more influence it will have on the estimated values at the site location (Apaydin et al., 2004). IDW have been widely used because its relative simplicity and good results comparing with more sophisticated models. Apaydin et al., (2004) compared six spatial interpolation methods for the estimation of six weather parameters and concluded that IDW performed well against Local and Global polynomial interpolation, Completely regularized spline, and the well-known Kriging model in three of its variants: Ordinary, Simple, and Universal. Similar analyses were carried out by Chen & Liu, (2012) for the estimation of rainfall distribution in the middle of Taiwan. Their results in terms of r , MAE, MSE, and RMSE showed that the key for satisfactory results resides in the correct estimation of the ratio of influence (R_i) and the order of the control parameter (α_i) in the IDW model. In this work, for the reasons previously discussed and due to its relatively low computational cost, IDW was performed for the estimation of hourly T . The following equations represent the IDW interpolation:

$$y_p = \sum_{i=1}^N w_i x_i \quad (2.5)$$

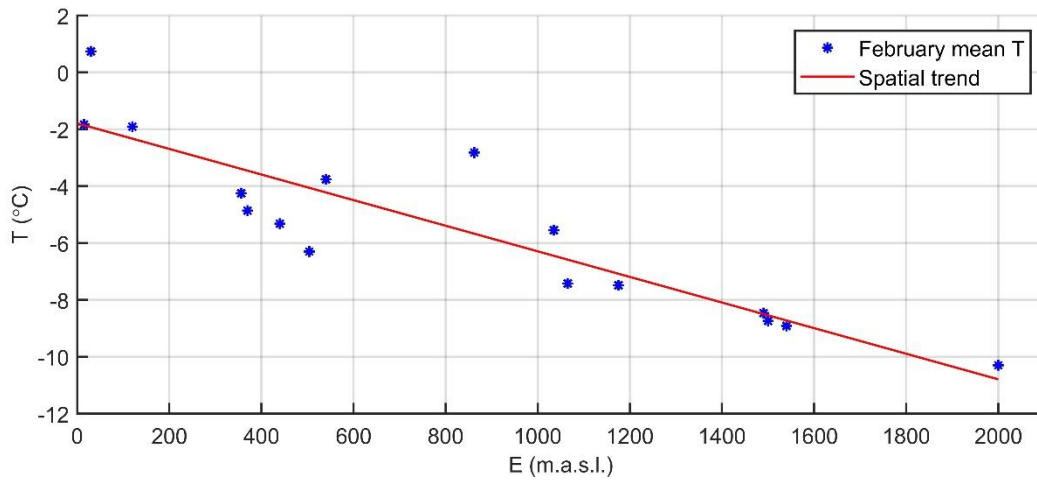
$$w_i = \frac{d_i^{-\alpha_i}}{\sum_{i=1}^N d_i^{-\alpha_i}} \quad (2.6)$$

where $y_p (T_p)$ is the unknown weather variable at HE, $x_i (T_i)$ represents the known weather variables of the nearby weather stations, w_i is the weighting of each nearby station, d_i (m) is the

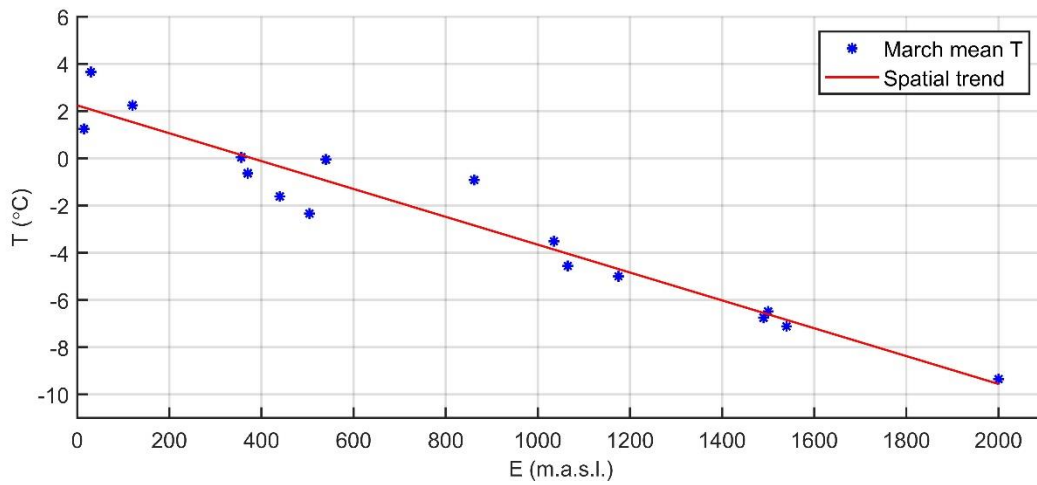
Euclidean distance from each weather station to HE, N is the number of weather stations considered, and α_i is the control parameter. The estimation of the control parameter has been discussed in previous studies with similar aims than the present study. While it is true that there is not a general parameter that works for all cases, there have been some approximations depending on the variable in study. Fan et al., (2015) used an $\alpha_i = 2$ for wind speed forecasting in Europe showing satisfactory results when comparing IDW with Kriging and Auto Regressive models. On the other hand, Gemmer et al., (2004) have set the control parameter to six for the estimation of monthly precipitation trends in China. Chen & Liu, (2012) decided to vary α_i within a range from 0 – 5 with a delta of 0.1. They also performed IDW for a range of R_i between 10 and 70 km. While a combination of specific α_i and R_i values gave them good results, they concluded that it is not possible to assume a value that can performed equally good for all the studies conducted. For this reason, the procedure described in Chen & Liu, (2012) were taken into consideration in the present thesis. The value of α_i was varied within a range from 0 to 5 with a delta of 0.5.

Because IDW is an interpolation method that do not take into account the elevation of the measured point, a spatial de-trending must be done before performing Equation (2.5) and Equation (2.6) for the variable in study (Fan et al., 2015). Temperature de-trend can be applied by calculating the laps rate (L) and using the elevation as the predictor. The lapse rate L is defined as the decrease in temperature with respect to altitude over a vertical profile of the atmosphere (He & Wang, 2020). This trend can be calculated with linear regression and its goodness of fit can be estimated with r^2 . Because different laps rates can be expected depending on the season of the year, it is good practice to do a monthly segmentation of the data (Kurtzman & Kadmon, 1999). The monthly mean of each year considered in this study was estimated and used to fit the linear regression models. At the end of the temperature de-trending analysis, 12 different L values correspondent to the 12 months of the year were obtained and used to convert the values of temperature to $E = 0$ m. At the end of the interpolations, the trend was added again to its correspondent elevation (HE). Figure 2.3a and b shows the fitted linear regression models correspondent to the month of February and March, respectively, for the sixteen weather stations within R_2 , while Figure 2.4 shows the correspondent Lapse rate for each month. The rest

of the linear regression models for the construction of the Lapse rate plot can be consulted in Appendix A.



a)



b)

Figure 2.3. Spatial trend and weather stations (blue dots) for the month of a) February ($L = 0.45$ °C/100 m), $r^2 = 0.80$, and b) March ($L = 0.59$ °C/100 m), $r^2 = 0.93$.

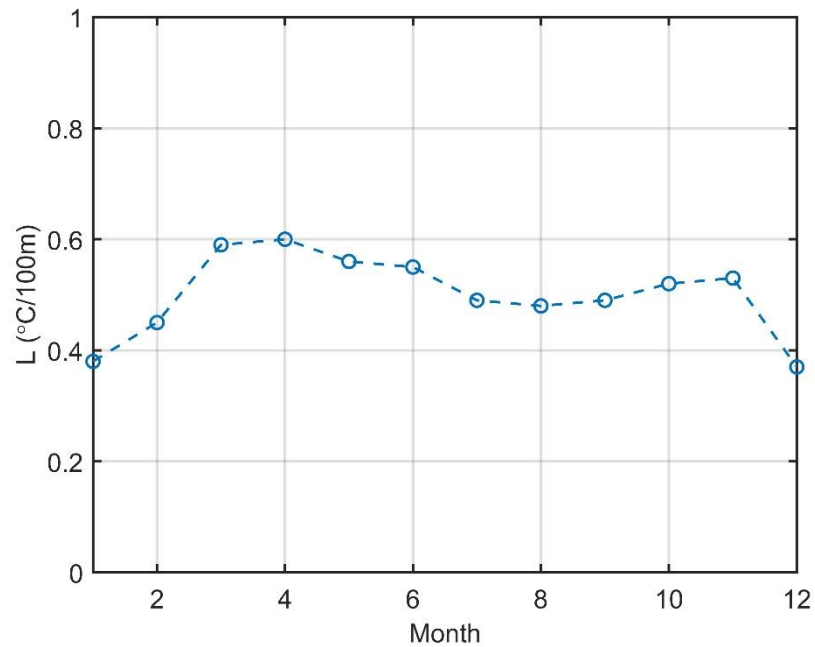


Figure 2.4. Lapse rate (L) per 100 m of elevation for each month.

2.3.2 K Nearest Neighbors Imputation

As previously discussed, p was the most difficult variable to find in the analyzed weather stations. The highest elevated station that contains p records is station 3 at $H = 504$ m. Above that altitude, the estimation of water precipitation is quite challenging due to the presence of drizzle, ice pellets, hail, and snow, among other types of precipitation. The lack of information at higher elevations made not possible to obtain a spatial trend that corresponds to HE. Furthermore, in the case of p , data from the WRF model at HE is not available, and no comparison could be made in this case. For this reason, HE and its closest station (station 12) were assumed part of the same basin, and the analysis focused on filling MD of station 12 by performing the KNNI method. KNNI is a simple imputation methodology that have been observed to perform well when $MD < 10\%$ (Aieb et al., 2019). It takes into consideration the records in the most correlated nearby stations, such that:

$$p_p = \frac{\sum_{i=1}^K p_i}{K} \quad (2.7)$$

where p_p (mm) is the missing precipitation record at station 12, p_i (mm) is the observed record at the nearby weather stations, and K is the number of neighbor stations. From Figure 2.5 is possible to observe that stations 9 and 7 are the most correlated with station 12. This was expected due to the relatively small Euclidean distance between the stations. Equation (2.7) was performed taking those stations into consideration. If one of the stations had a missing record at the same hour than station 12, then just the value of the station with records was imputed. If the two neighbor stations had missing records, that hour was leaved as MD. At the end, 24 hours were missing for station 12, corresponding to MD = 0.02%, and with 3 continuous hours as the maximum gap. Those missing values were then filled with linear interpolation to complete the station such that MD = 0%.

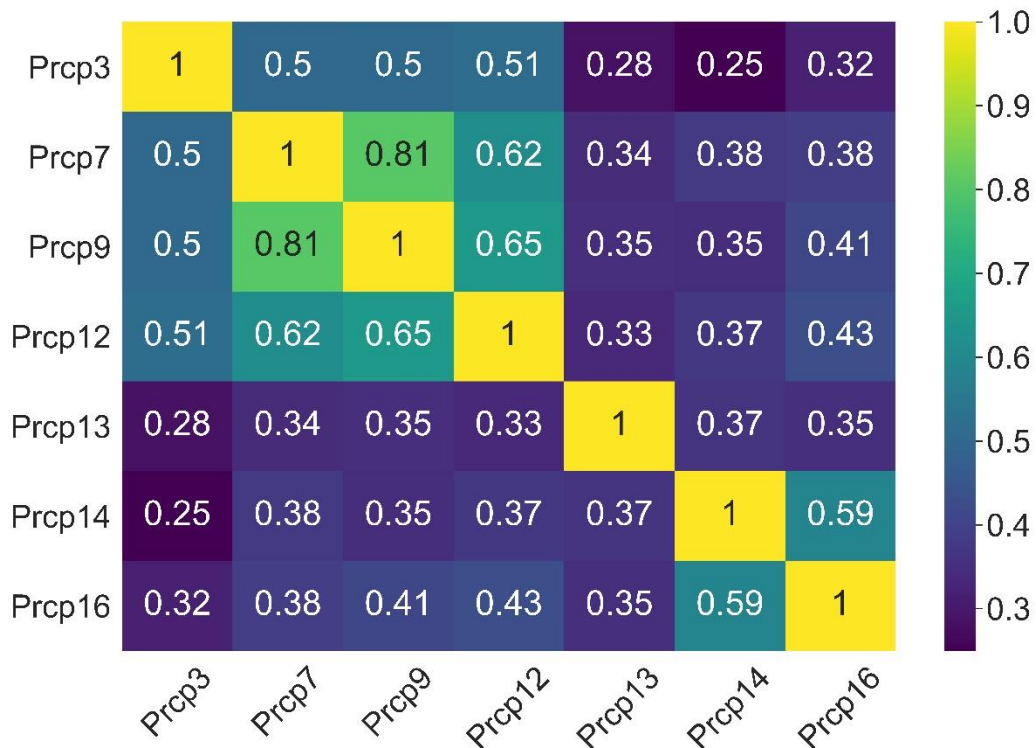


Figure 2.5. Precipitation data and its correlation with the nearby weather stations, $Prcp n$, where n is the number of the weather stations indicated in Table 2.1.

2.3.3 Artificial Neural Network

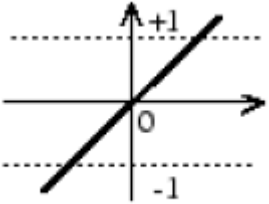
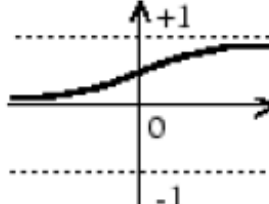
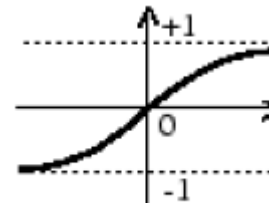
Artificial Neural Networks (ANN) are powerful machine learning algorithms inspired from the functioning of the human brain (Philippopoulos & Deligiorgi, 2012). This approach has been successfully applied in the field of wind engineering for wind speed and wind-power predictions (Afshar, 2016; Filik & Filik, 2017; Lawan et al., 2020; Philippopoulos & Deligiorgi, 2012). The advantage of applying this method for wind speed forecasting relies in its ability to identify nonlinear patterns between the surrounding weather stations (inputs) and the site of interest (targets) and thus outperform traditional interpolation methods in complex terrain (Philippopoulos & Deligiorgi, 2012). An ANN is composed of mainly three parts: the input layer, the hidden layers, and the output layer. Each layer contains a number of neurons, or nodes, which receives the inputs variables and by applying mathematical transformations they pass information to the next layer (Afshar, 2016).

Equation (2.8) is the general formula which will output the predictions of an ANN (Philippopoulos & Deligiorgi, 2012).

$$y = f \left(\sum_{i=1}^n x_i w_i + b_i \right) \quad (2.8)$$

where x_i are the input variables, w_i are the weights, b_i are offset parameters, n is the number of neurons in the last hidden layer, and f is the activation function which will transform the values at each node. The selection of the activation function depends on the kind of predictions one would like to measure. Table 2.2, for example, shows a list of the most popular activation functions (Afshar, 2016).

Table 2.2. Most popular activation functions (Afshar, 2016).

Activation Function	Equation	Graphical Representation
Linear	$f(x) = x$	
Logistic sigmoid	$f(x) = \frac{1}{1 + e^{-x}}$	
Hyperbolic tangent	$f(x) = \frac{1 - e^{-x}}{1 + e^{2x}}$	

In this thesis, to capture the nonlinear relationship between the inputs and the targets, a hyperbolic tangent (tanh) activation function is considered for the input and hidden layers, while a linear activation function is selected for the output layer.

The following subsections briefly describe the characteristics of the ANN used in the present study:

2.3.3.1 The dataset

To train the ANN, the data must be divided into the training and test set (Afshar, 2016). The dataset considered to train the network consists of the weather characteristics from the weather

stations from 2005 – 2015 as the predictors, and the WRF model records from 2005 – 2015 as the targets. The dataset was divided into 70% for the training set and the remaining 30% of the data was divided into 50% for the validation set and 50% for the test set to avoid overfitting. Cross validation was applied between the predictions and the validation set during the training stage.

2.3.3.2 Loss function

As previously mentioned, the input variables are modified by the activation function at the input layer and the updated values are passed to the hidden layers and eventually to the output layer. This first step of the process is called forward propagation. The predicted values are then compared with the targets and the error between them is computed. This error is measured by the loss function, which can be any metric of goodness of fit introduced in Section 2.2 (Philippopoulos & Deligiorgi, 2012). In the present thesis, the MAE is selected as the loss function, as recommended by Willmott & Matsuura, (2005) for the evaluation of the network performance. At the backpropagation stage, the error computed is propagated backward from the input layer through the hidden layers and finally to the input layer (Basheer & Hajmeer, 2000). Backpropagation networks are widely used due to its ability to identify the contribution of each weight to the total error and calculate the proper changes to reduce the loss function at the next epoch. An epoch in machine learning is defined as the process of completing the forward and back propagation one time. For a better understanding on the full mathematical procedure to compute backpropagation, please refer to Krose & Van Der Smagt, (1996).

2.3.3.3 Optimization algorithm

During the backpropagation stage, the network attempts to update the parameters w and b to minimize the loss function (Afshar, 2016). For this to be possible, the gradient descent algorithm is applied. This algorithm calculates the gradient of the loss function with respect to the parameters w and b by applying the following equations (Pereira & Borysov, 2019):

$$w_{i+1} = w_i - \eta \frac{\partial Loss}{\partial w_i} \quad (2.9)$$

$$b_{i+1} = b_i - \eta \frac{\partial Loss}{\partial b_i} \quad (2.10)$$

where η is the learning rate. A schematic representation of the gradient descent of the loss function is shown in Figure 2.6 (Pereira & Borysov, 2019). The choose of η should be carefully analyzed, science a big η may compute faster solutions but may never find the optimal minimum point of the loss function curve, while a small η will eventually find the optimal point but may compute the solution in a considerably greater amount of time. One problem of the plain gradient descent from Equations (2.9) and (2.10) is that the probability of getting stuck in a local minimum point of the loss function is high and thus the optimal solution will not be found, as illustrated in Figure 2.6. Stochastic gradient descent is a simple solution for this problem, where the gradients errors are calculated considering mini-batches or subsets of the complete dataset introducing noise to the estimated gradients allowing the parameters w and b to escape from local minimums of the loss function (Pereira & Borysov, 2019). Several optimization algorithms can be found in the literature implementing stochastic gradient descent to update the parameters. The most used and popular optimization algorithms due to its good computational efficiency are the momentum, RMSprop, and the recently introduced Adam optimizer, which is a combination of the momentum and RMSprop gradient descent. Adam stands for adaptive moment estimation and is an adaptive learning rate method which considers individual values of η for the network parameters (Bushaev, 2018). If the gradient of the loss function is assumed to be a random variable, then its first and second moment related to the expected value and the variance of the distribution, respectively, can be computed as follows (Kingma & Ba, 2017):

$$m_{i+1} = \beta_1 m_i + (1 - \beta_1)g_t \quad (2.11)$$

$$v_{i+1} = \beta_2 m_i + (1 - \beta_2)g_t^2 \quad (2.12)$$

where m_{i+1} and v_{i+1} are the first and second moment at the $i^{th} + 1$ timestep, respectively, β_1 and β_2 are exponential decay rates for the moments set to 0.9 and 0.999, respectively, and g_t is the loss function gradient at the current minibatch or data subset. As the moments are initialized as zero vectors, they need to be bias-corrected by applying the following equations:

$$\hat{m}_{i+1} = \frac{m_t}{1 - \beta_1^i} \quad (2.13)$$

$$\hat{v}_{i+1} = \frac{v_t}{1 - \beta_2^i} \quad (2.14)$$

Finally, the updated parameters from the Adam optimizer can be computed as follows:

$$\psi_{i+1} = \psi_i - \frac{\eta \hat{m}_{i+1}}{\sqrt{\hat{v}_{t+1} + \varepsilon}} \quad (2.15)$$

where ψ_{i+1} represents the updated parameters w or b at the $i^{th} + 1$ timestep, and ε is a parameter set to 10^{-8} to avoid dividing by zero in the above equation.

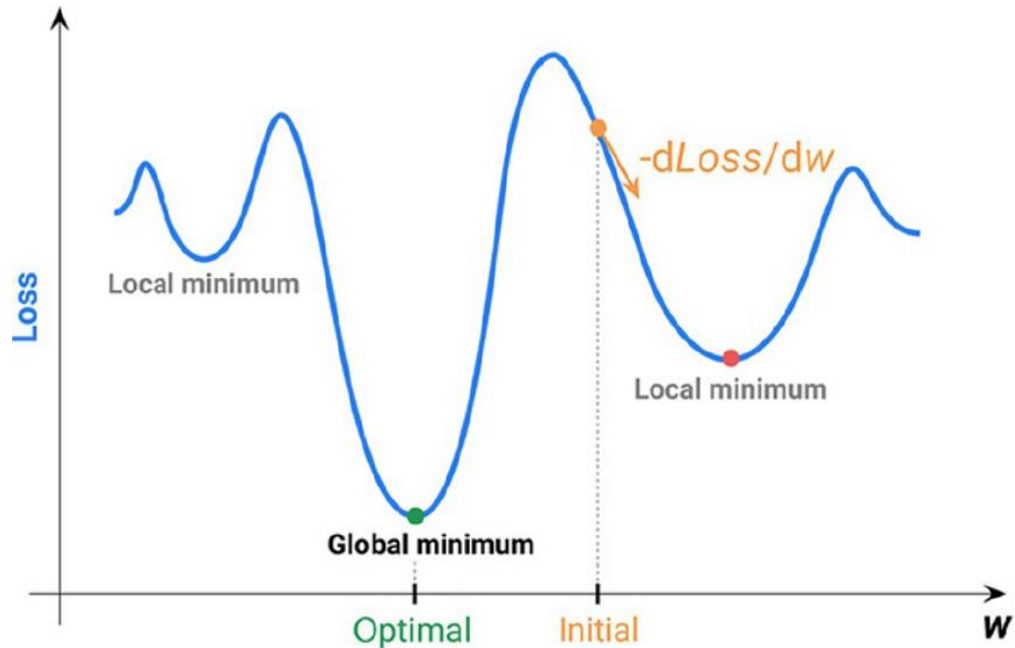


Figure 2.6. Loss function gradient descent (Pereira & Borysov, 2019).

2.3.3.4 Regularization

Regularization prevents the ANN to capture the noise and “memorize” the validation data to avoid the risk of overfitting. A characteristic of overfitting is typically observed when an outstanding performance is obtained in the validation set but a seriously poor performance is obtained in the test set. In this work, the dropout technique is used in each hidden layer. With this technique, a specified number of hidden neurons are randomly omitted from the ANN and a hidden node cannot rely on the omitted hidden units being present (Hinton et al., 2012). In this way, practically a different ANN is trained at each epoch and the loss function is reduced due to the average predictions produced by each trained ANN (Hinton et al., 2012). A dropout rate of 20% is applied in this work, meaning that 1 out of 5 hidden neurons of each hidden layer will be randomly excluded from the network.

2.3.3.5 Architecture of the ANN

The wind speed, wind direction, atmospheric pressure, and temperature were considered the predictors. In this case, just the 7 weather stations with complete records were considered (2005

– 2020) so that the stations are contributing with 28 predictors. In addition, the hour of the day and month of the year were included in the input parameters to capture wind speed diurnal and seasonal trends. Thus, the network is fed with a total of 30 predictors at the input layer. Normalizing the data is not strictly necessary for ANNs, but it is recommendable for a faster learning process (Afshar, 2016; Philippopoulos & Deligiorgi, 2012). The data were normalized using the min-max scaler technique in the range between 0 and 1, except for the temperature, which was normalized between -1 and 1 by applying the following equation (Afshar, 2016):

$$\hat{x} = low + \frac{(high - low)(x - \min X)}{\max X - \min X} \quad (2.16)$$

where \hat{x} is the transformed value, x is the original observation from the X sample, and *low* and *high* refers to the minimum and maximum value of the min-max scaler normalization.

Finding the optimal architecture of the network is an empirical process, however, the number of neurons in the hidden layers is typically recommended to be between the numbers of neurons in the output and input layers (Afshar, 2016). For this reason, 3 hidden layers of 20 neurons were selected for this network. The output layer consists of just one neuron, which will predict the hourly wind speed records at HE. The network was developed in the open source TensorFlow 2.0 and Keras 2.3.0 libraries by using a Sequential model. A schematic representation of the network used in this thesis is shown in Figure 2.7, while Table 2.3 shows a summary of its characteristics described along subsection 2.3.3.

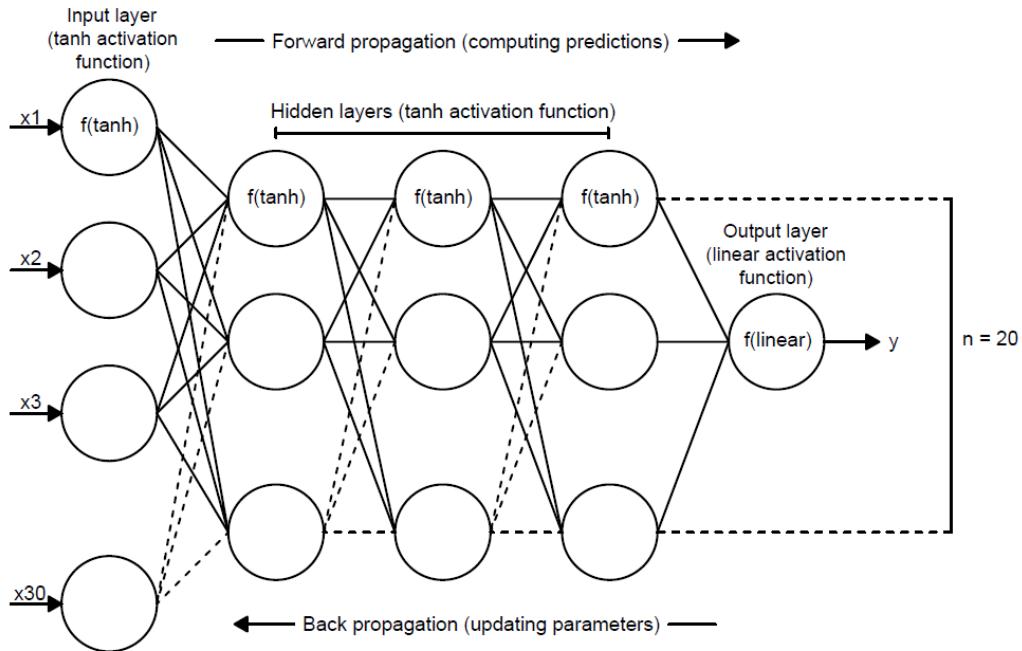


Figure 2.7. Architecture of the network.

Table 2.3. Characteristics of the network.

Training set	70%
Validation set	15%
Test set	15%
Loss function	MAE
Optimization algorithm	Adam
Regularization	Dropout (20%)
Normalization	Min-max scaler
Number of neurons in the input layer	30
Number of hidden layers	3
Number of neurons in the hidden layers	20
Number of neurons in the output layer	1
Activation function in the input layer	tanh
Activation function in the hidden layers	tanh
Activation function in the output layer	linear

The wind speed values from the weather stations were elevated to 20 m. above ground (location of the cable) before the training process by applying the power law (Simiu & Scanlan, 1996).

$$\frac{u}{u_{ref}} = \left(\frac{z}{z_{ref}} \right)^{I_u} \quad (2.17)$$

$$I_u = \frac{1}{\ln\left(\frac{z}{z_o}\right)} \quad (2.18)$$

where u (m/s) is wind speed, z (m) is the height at which the measurements were made (10m above ground), u_{ref} (m/s) is the reference velocity, I_u is the turbulence intensity, and z_o (m) is the characteristic roughness length at each weather station location. The number of epochs were set to 500, and the remaining 5 years (2015 – 2020) of records from the weather stations were used to forecast the wind speeds at HE.

2.4 Ice accretion model

The weather data acquired from the analysis described in section 3 were then used as inputs to simulate ice accretion rate on a single conductor. Here, the model described in (Makkonen, 2000) was used due to its relative simplicity and formerly acknowledge accuracy in the predictions. According to the model, the rate of icing is obtained as follows:

$$\frac{dM}{dt} = \alpha_1 \alpha_2 \alpha_3 W u A \quad (2.19)$$

where $W = 0.067p_i^{0.846}$ (g/m³) is the liquid water content (Jones, 1998) A is the cross section of the cable, and α_1 , α_2 , and α_3 are variables ranging from 0 to 1, known as the collision, sticking, and accretion efficiency, respectively. Equation (2.19) needs to be solved according to the kind of ice formation on the conductor. Details of the development of the empirical solutions and

numerical simulations can be found in Fu, (2004), Ličar, (2016), Makkonen, (1984), or Makkonen (2000), among others, and thus are not developed here. However, the estimations of the variables of Equation (2.19) are described along this section.

The collision efficiency α_1 is defined as the ratio of the particles (droplets) that hit the object to the total of particles (Makkonen, 2000). To know the collision efficiency, the trajectories of the water droplets and the velocity vectors at the time of collision with the cable must be solved. However, if a radial ice accretion shape is assumed, then, for practical proposes, the overall collision efficiency α_1 can be solved numerically following the empirical procedure described in Finstad et al., (1988). The assumption of a radial ice accretion shape is due to the finite torsional stiffness of the cable (Roberge, 2005). When the ice eccentricity is large enough, the wire will eventually rotate around its axis and the accretion will become a cylindrical sleeve (Roberge, 2005). At the early stage of the growth process, before the cable rotation and thus before the radial ice accretion shape is formed, the rime and glaze may form different ice profiles due to its different physical growth conditions on the windward side of the wire. Modelling those shapes are crucial when the effects of the vertical galloping are required. The study of complex ice shapes requires detailed aerodynamic analyses, which are not included in this thesis. The procedure to estimate α_1 is described in the following equations:

$$\alpha_1 = A - 0.028 - C(B - 0.0454) \quad (2.20)$$

$$A = 1.066K_n^{-0.00616} e^{-1.103K_n^{-0.688}}$$

$$B = 3.641K_n^{-0.498} e^{-1.497K_n^{-0.694}} \quad (2.21)$$

$$C = 0.00637(\varphi - 100)^{0.381}$$

$$K_n = \frac{\rho_w d^2 u}{9\mu D} \quad (2.22)$$

$$\varphi = \frac{R_{ed}^2}{K_n} \quad (2.23)$$

$$Re = \frac{\rho_a du}{\mu} \quad (2.24)$$

where K_n and φ are the inertia and Langmuir parameter, respectively, ρ_w (kg/m^3) is the water density, d is the droplet median volume diameter, μ ($\text{kg/m} \cdot \text{s}$) is the absolute viscosity of air, D (m) is the cable diameter, and R_{ed} is the droplet Reynolds number. In this paper, the droplet median volume diameter was taken as $d = 25$ (μm) as it has been observed as a good representation of the droplet distribution spectrum during freezing conditions (Thompson et al., 2017). The sticking efficiency α_2 is reduced from 1 when the water droplets bounce after the impact with the surface. In the case of rime and glaze ice it is possible to assume no bounce of the water droplets and thus taking $\alpha_2 = 1$ at every time step (Makkonen, 2000). The accretion efficiency α_3 depends on the type of ice formation. For rime ice, the supercooled water droplets froze instantaneously after the impact and $\alpha_3 = 1$ can be assumed. In the case of glaze ice (wet growth), the water droplets are observed to run off the cable surface and α_3 can be solved from the heat balance on the icing surface shown in the following equation (Makkonen, 2000):

$$\alpha_3 = \frac{1}{F(1-\lambda)Lf} \left[(h + 6a_i)(t_s - T) + \frac{h\varepsilon_i L_e}{C_p P_i} (e_s - e_a) - \frac{hr_i u^2}{2C_p} + FC_w(t_s - T) \right] \quad (2.25)$$

where $F = \alpha_1 \alpha_2 w u$, λ is the liquid fraction taken as 0.3, Lf is the latent heat of fusion at 0 °C, h is the heat transfer coefficient, a_i is the radiation linearization constant (8.1×10^7 (K^3)), t_s is the cable surface temperature, ε_i is the ratio of molecular weights of dry air and water vapor (0.622), L_e is the latent heat of evaporation at 0 °C, C_p is the specific heat of air, P_i is the air

pressure, e_s is the saturation water vapor pressure at 0 °C (6.17 (mbar)), e_a is the saturation water vapor pressure at T_i , r_i is the recovery factor for viscous heating (0.79 in the case of a cylinder), and C_w is the specific heat of water. Equation (2.25) can be solved numerically, first assuming wet growth so that $t_s = 0$ °C, if the outcome from the equation is not $0 < \alpha_3 < 1$, then the wet growth assumption is proven to be wrong, and t_s can be solved numerically for dry growth ($\alpha_3 = 1$) (Ličar, 2016; Makkonen, 2000).

The ice density depending on the type of ice can also be obtained numerically at each time step. The resultant ice density is an important factor due to its influence in the accretion diameter. For its calculation in g/cm^3 , the following procedure was performed (Macklin, 1962):

$$\begin{aligned} \rho_i &= 0.11R^{0.76} && \text{for } R \leq 10 && (2.26) \\ \rho_i &= R(R + 5.61)^{-1} && \text{for } 10 < R \leq 60 \\ \rho_i &= 0.92 && \text{for } R > 60 \\ R &= -\frac{u_0 d}{2t_s} \end{aligned}$$

where R is the Macklin's density parameter, and u_0 is the impact droplet velocity.

For the ice mass reduction, two physical processes were taken into consideration: evaporation and sublimation rate. Evaporation will take place when $T > 0$ °C and ice will start melting relatively fast (Harstveit & Vindteknikk, 2009). However, for winters where T can stay below 0 °C for long time, sublimation rate needs to be included in the deicing rate modelling. Sublimation is defined as the change of phase directly from solid to vapor and the deicing rate occurs slowly if comparing with ice melting (Agustsson & Nygaard, 2016; Druetz et al., 1995). Although evaporation and sublimation rate can be estimated by evaluating the energy balance model, here, for simplicity, a typical melting rate of 0.3 $\text{kg/m} \cdot \text{h}$, and sublimation rate of 0.02 $\text{kg/m} \cdot \text{h}$ when $T > 0$ °C, and at dry hours (i.e. $p_i = 0$), respectively, were included in the model (Druetz et al., 1995). After the simulation, 15 years of hourly data pairs of wind speed and ice accretion diameter were obtained.

All the storms within that period were identified and used to obtain their probability distribution in terms of duration (hours) and intensity (radial thickness). A storm here is considered an icing event in which the accreted mass exceeded 0.1 kg/m for at least three consecutive hours. The maximum hourly wind speed recorded during the icing event (wind on ice velocity) was identified and selected as the data pair for the maximum radial ice accretion (R_{eq}). Hence, the maximum hourly velocity and maximum radial ice accretion during an icing event were assumed concurrent and used to characterize the joint wind and ice hazard.

2.5 Probability distributions

The results from the analyses described in the previous subsections were fitted to different probability distributions according to their characteristics. The wind speed values from the WRF model and the ANN were fitted to a Weibull distribution and their scale and shape parameters were compared to check if there was good agreement. Similarly, their extreme values were fitted with the well-known Gumbel distribution and the t -year return period velocities were estimated. The Weibull probability distribution function is shown in Equation (2.27), followed by the Gumbel extreme value distribution in Equation (2.28) (Gumbel, 1954; Weibull, 1939).

$$f(x) = \frac{k}{a} \left(\frac{x}{a}\right)^{k-1} e^{(-x/a)^k} \quad (2.27)$$

$$V_t = U + \frac{1}{b} (-\ln(-\ln(1 - P))) \quad (2.28)$$

where k and a are the shape and scale parameters of the Weibull distribution, respectively, in this case, x represents the wind speeds u from the ANN and WRF model, V_t (m/s) is the t -year

return period velocity, U is the mode of the extreme value distribution, $\frac{1}{b}$ is the dissipation, and P is the probability of the event occurring once every t years ($P = \frac{1}{t}$).

The ice radial thickness R_{eq} was fitted to a Generalized Pareto distribution, since it has been observed to be a good fit for ice accretion extreme values distribution (El-Fashny, 2002). 500 years of icing events were simulated by generating random, or pseudo values of wind speed or ice accretion from the inverse of their fitted cumulative density functions. The Weibull cumulative density function (CDF) shown in Equation (2.29) was used to generate the hourly wind speed pseudo records while the Generalized Pareto (GP) CDF shown in Equation (2.30) was used for the ice accretion radial shape (Sinh et al., 2016).

$$P(V \leq V_0) = 1 - e^{-\left(\frac{V_0}{a}\right)^k} \quad (2.29)$$

$$P(X \leq x|\theta) = 1 - \left[1 + \frac{\tau(x - \theta)}{\sigma}\right]^{-\frac{1}{\tau}} \quad (2.30)$$

where V is the wind speed in this case, V_0 is a specific wind speed, x is the radial ice accretion, θ is the threshold parameter, and τ and σ are the shape and scale parameters of the GP distribution, respectively.

2.6 Results and discussion

The results from the data analysis of the weather characteristics are shown in Figure 2.8. The maximum correlation coefficient obtained between the WRF and IDW models was $r = 0.92$ with a control parameter $\alpha_i = 1.5$. This good agreement reinforced the hypothesis of the linear relationship between low and high elevated terrain hourly temperature records for the analyzed weather stations with relatively the same longitude and latitude coordinates. For the wind speed

analysis, the ANN achieved a correlation coefficient of $r = 0.81$. The ANN was able to identify the nonlinear relationship between the surrounding weather stations and HE in general but failed to identify the outliers above the 99 percentile, as it can be observed in Figure 2.8. The reason for its difficult modelling is the complex terrain where HE is located, the randomness and nature of wind speed decorrelates rapidly in space and makes its prediction quite challenging. The Weibull parameters of the distributions and the goodness of fit are shown in Table 2.4.

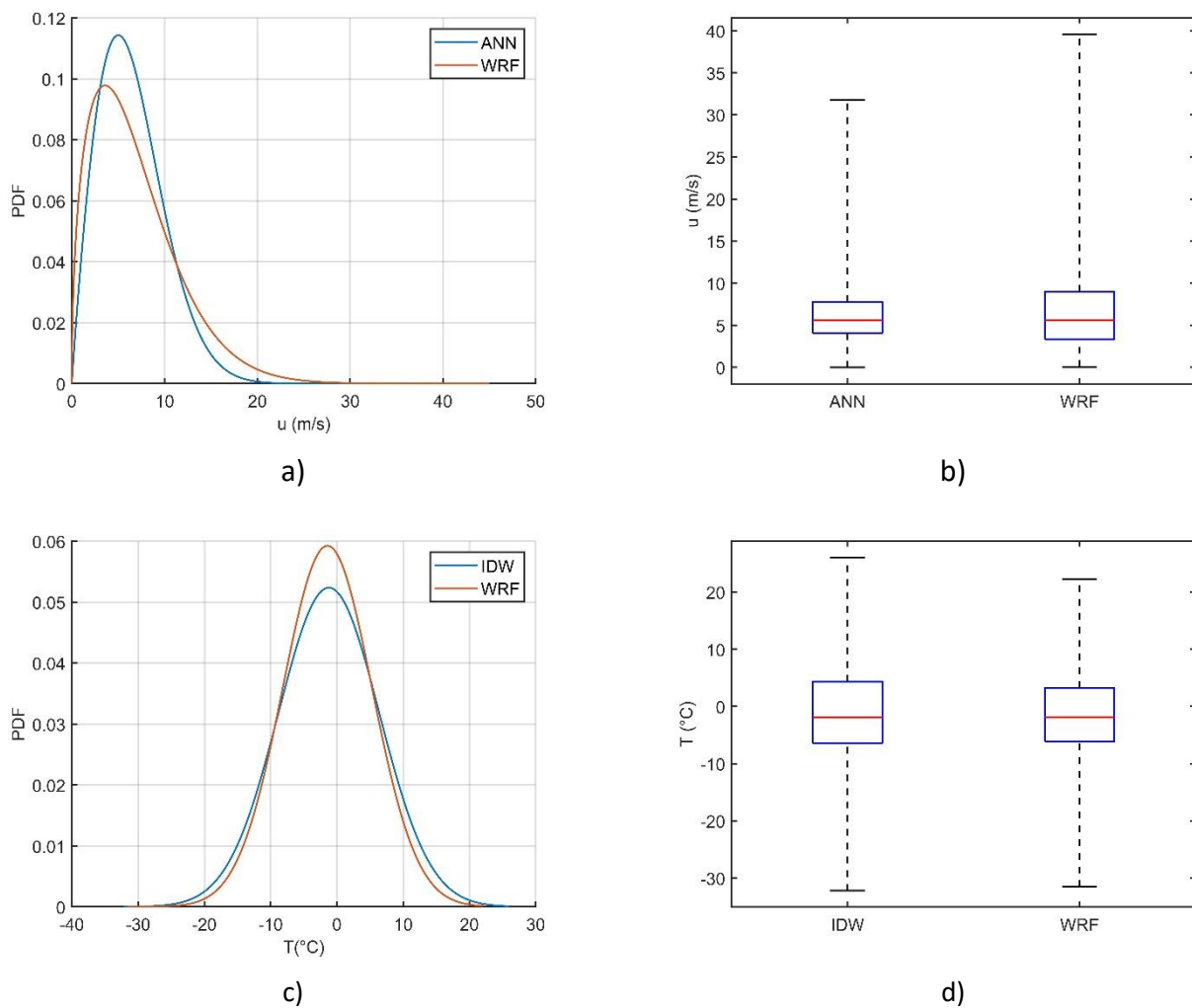


Figure 2.8. a) Fitted Weibull distribution for wind speed historical records, b) Box plots for wind speed historical records, c) Fitted Normal distributions for temperature historical records, and d) Box plots for temperature historical records.

Table 2.4. Goodness of fit and probability distribution parameters.

Variable	α_i	r	MAE	MSE	RMSE	Weibull Parameters (k, a)
T (°C)	1.5	0.92	2.01	7.45	2.73	--
u (m/s)	--	0.81	2.46	10.95	3.31	ANN: (1.92, 7.32) WRF: (1.48, 7.60)

From the ice accretion model, several observations can be made. All the storms within the 15 years of historical records were identified and their intensity in terms of R_{eq} and duration were registered. A total of 385 icing events were identified for a storm recurrence rate of $385/15$ years = 25.67 events per year. Table 2.5 contains information of the 5 most severe storms modelled. The evolution of the 5 storms reported in Table 2.5 can be consulted in Appendix A. The wind speeds during icing conditions from Table 2.5 were compared with the design velocities reported in Jubayer & Hangan, (2018). In their analysis, the authors obtained design wind and gust speeds for snow covered surfaces (characteristic of the wintertime) and for three different wind directions at 10 m above ground for the same HE as in the present thesis by performing numerical and experimental simulations. The most conservative design wind and gust speeds from their analysis were taken as reference and were elevated at 20m above ground by applying Equation (2.17) and Equation (2.18). Here, the design wind speed was considered as the average of the maximum velocities reported in Table 2.5, and the design gust wind speed was obtained by applying a factor of 1.36 based on the Durst Curve (ASCE 7). The mentioned comparison is shown in Table 2.6. Note that this comparison does not intend to provide the wind data pair for the joint analysis, instead, the comparison is made for consistency purposes of the wind speeds magnitude presented at HE.

It is pertinent to remember that this analysis assumes a radial ice accretion on the conductor based on the overall collision efficiency, as previously discussed. For aerodynamic analysis where galloping may occur, modelling the shape of the ice accretion is needed instead of assuming a radial shape. This can be done by modelling the local collision efficiency on the conductor, using the information from Table 2.5 as inputs. Such models can be found in Fu et al., (2006), and

McComber & Touzot, (1981), for example, or by using commercial ice accretion software like LEWICE or Ansys FENSAP-Ice. Other authors have assumed a simplified ice accretion shape to perform aerodynamic analysis, since an axial growth on the windward side of the conductor during icing events has been observed to be in good agreement with field observations where rime ice or wet snow may accrete (Poots & Skelton, 1995; Rossi et al., 2020). The results for the ice density indicate that most of the ice formation may be soft rime for this specific case of study, and is consistent with the analysis presented in Rossi et al., (2020). at HE based on the analysis from the WRF model. A mean ice density of $\bar{\rho}_i \approx 300 \text{ kg/m}^3$ was obtained for all the icing events identified in the analysis. This density can be used for the estimation of the wind and ice load when considering rime ice formation. Figure 2.9 shows the histogram of occurrence of ice formation from the ice accretion model. The few events where the ice density was $\rho_i > 900 \text{ kg/m}^3$ (glaze ice) corresponds to all the cases when the Macklin's density parameter was $R > 60$, as stated in Equation (2.26). The ice accretion extreme values analysis is shown in Figure 2.10. A good fit to the Generalized Pareto distribution for R_{eq} in terms of the PDF, CDF, Quantile-Quantile (Q-Q) plot and return levels can be observed. This observation is consistent with previous studies where the GP distributions are recommended to fit ice accretion extreme values (El-Fashny, 2002). The GP parameters and the measure of its goodness of fit from the Q-Q plot are reported in Table 2.7. The Peak Over Threshold (POT) method was used for the selection of θ . This was done by trial and error, with the hypothesis that the extreme values of R_{eq} follow a GP distribution. The quintile 0.7 were used as a first guess and the goodness of fit both qualitatively (Figure 2.10) and quantitatively (Table 2.7) where measured until the best fit was found. The 90 percentile showed the best results and was selected as the threshold θ in the analysis, with 38 out of 385 storms categorized as extreme events ($R_{eq} > \theta$) for an extreme recurrence rate of $38/15 = 2.53/\text{year}$.

Table 2.5. Information of the most severe storms. u_{max}) Maximum velocity presented during the evolution of the storm, \bar{u}) Mean velocity presented, \bar{T}) Mean temperature presented, \bar{p}) Mean precipitation presented.

Storm No.	Duration (hours)	R_{eq} (cm)	u_{max} (m/s)	\bar{u} (m/s)	\bar{T} (°C)	\bar{p} (mm)
1	146	12.48	30.73	14.92	-20.19	0.69
2	463	8.93	31.66	12.27	-13.28	0.47
3	111	7.81	15.09	9.20	-14.91	1.58
4	184	7.5	31.71	19.51	-16.87	0.25
5	95	6.89	31.01	21.74	-23.78	0.34

Table 2.6. Wind and Gust velocities from physical and ANN analyses.

Analysis	u (m/s)	$Gust$ (m/s)
(Jubayer & Hangan, 2018)	27.87	40.33
ANN	28.04	38.13

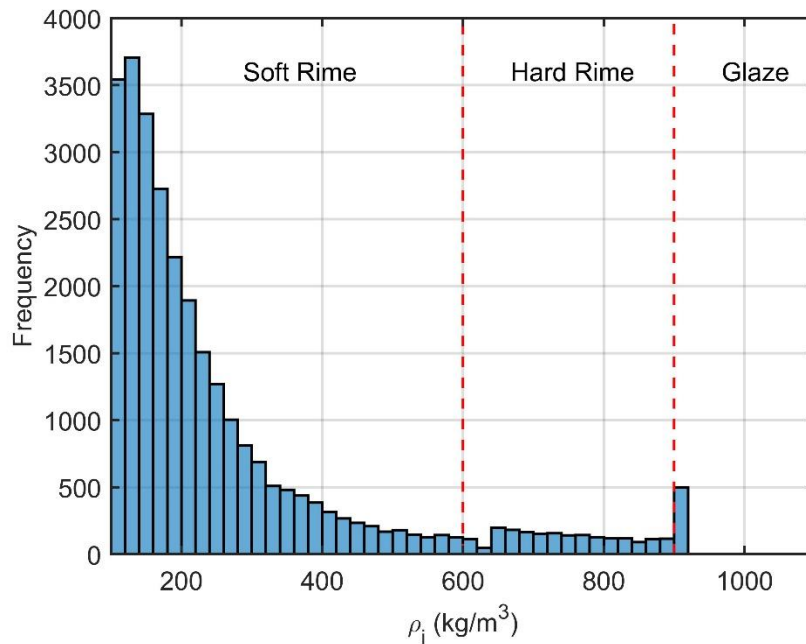


Figure 2.9. Ice density (ρ_i) and types of ice histogram based on the classifications reported in

Table 1.1.

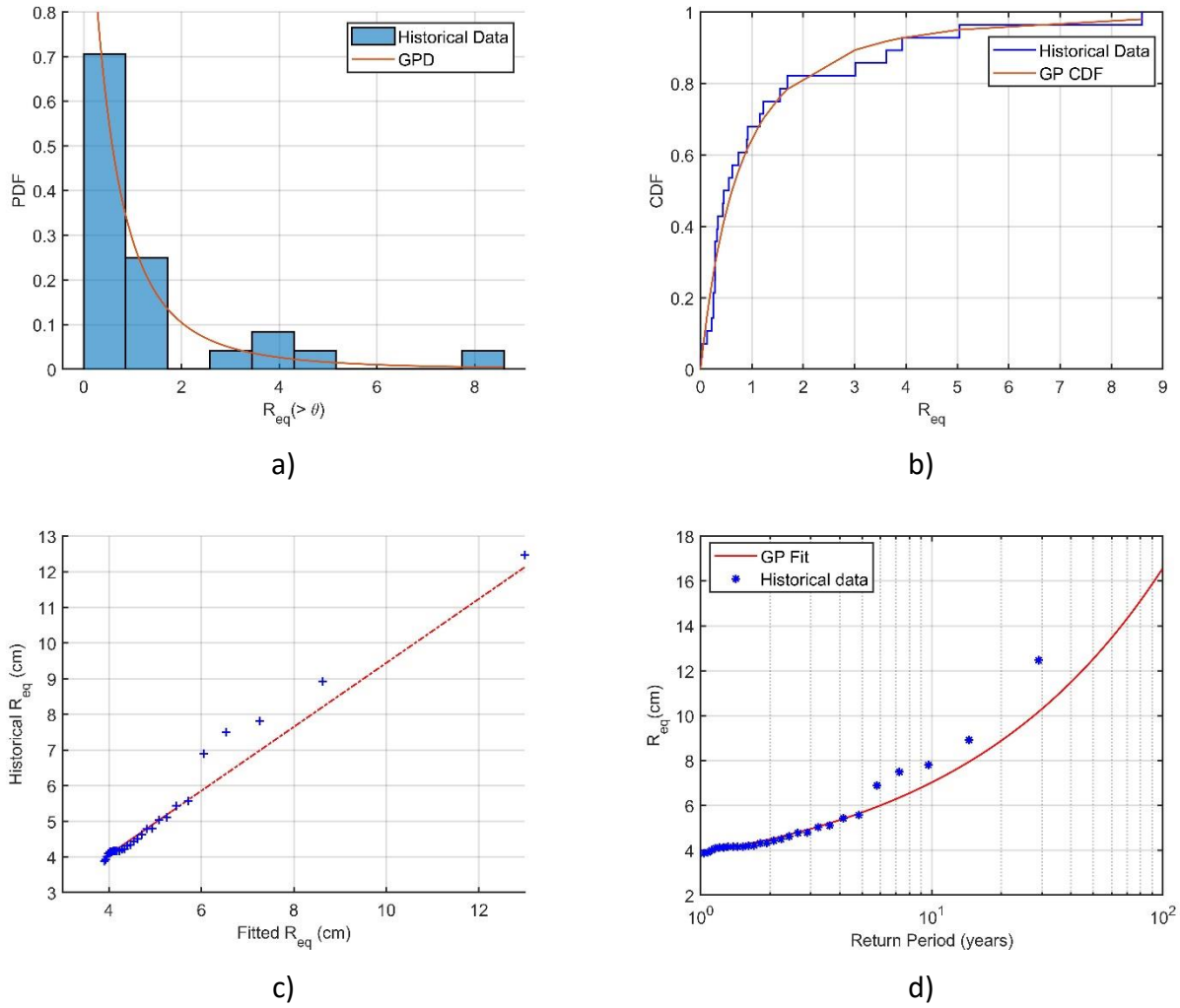


Figure 2.10. a) Generalized Pareto PDF, b) Generalized Pareto CDF, c) Q-Q plot, and d) Theoretical return levels vs fitted Generalized Pareto return levels.

Table 2.7. Distribution parameters and goodness of fit measured in terms of r) Correlation coefficient, MAE) Mean Absolute Error, MSE) Mean Square Error, RMSE) Root Mean Square Error.

Distribution	Parameters	r	MAE	MSE	RMSE
GP	$\tau = 0.48$ $\sigma = 0.74$ $\theta = 3.88$	0.98	0.12	0.05	0.23

The 50-year return levels for wind speed (V_{50}) and ice radial thickness ($R_{eq_{50}}$) are reported in Table 2.8. Overall, there is good agreement between the results from the WRF model and the analysis from the present work. The differences between the two models are of the order of 12% for V_{50} and 4% for $R_{eq_{50}}$. The ANN predictions are lower compared to the WRF modelled values due to the underestimation of the peak values previously discussed.

Table 2.8. 50-year return levels for wind speed and ice accretion.

Model	V_{50} (m/s)	Req_{50} (cm)
ANN, Ice accretion model	36.71	12.52
WRF, Ice accretion model	42	12

Finally, similarly to Rosowsky & Wang, (2014) and Sinh et al., (2016), the records were combined in order to characterize the wind and ice hazard. A joint scatter plot was built from the historical and simulated records (Figure 2.12). The wind speed values were converted to 3 second gust wind speed by a factor of 1.36, for structural design purpose. The joint frequency histogram is shown in Figure 2.11a. The joint complementary cumulative density function (JCCDF) or probability of exceedance curve was obtained from the product of their marginals' CDFs (Figure 2.11b). The hazard contours were drawn by projecting the JCCDF curve in the x-y plane for a given probability of exceedance and were taken as a reference for selecting the data pairs according to their hazard level (Figure 2.13). Each hazard contour in the figure corresponds to a different hazard level. Hazard levels are represented by the probability of exceeding a certain value in t years. Since the hazard contours are characterizing a joint hazard in this study, they indicate the probability of exceeding both values (R_{eq} and u) at the same time in t years. The CSA-C22.3 considers 3 reliability levels for the design, being related to 50, 150, and 500 years return period, respectively. Two combinations are proposed in the standard:

- C1: The low probability R_{eq} related to its reliability level return period (50, 150 or 500 years), and high probability u , related to the average of yearly maximum events.

- C2: The low probability u related to its reliability level return period (50, 150 or 500 years), and high probability R_{eq} , related to the average of yearly maximum events.

Thus, the contours presented correspond to the hazard levels of 2, 0.67, and 0.2% probability of exceedance, for 50, 150, and 500 mean year recurrence interval, respectively. From the hazard contours, it is possible to select the data pair which represents the worst case scenario when calculating the loads, and take those values into consideration for the design (Sinh et al., 2016). The combination C1 and C2 for the three reliability levels is also shown in Figure 2.13. It can be observed that the combinations are above all contours, even higher than the 0.2%, 500 hazard level. This is due to the assumption of combining two values which are strongly related to their extreme events, for which the probability of occurrence at the same time is extremely low. Table 2.9 contains information of the three reliability levels and both C1, and C2 combinations.

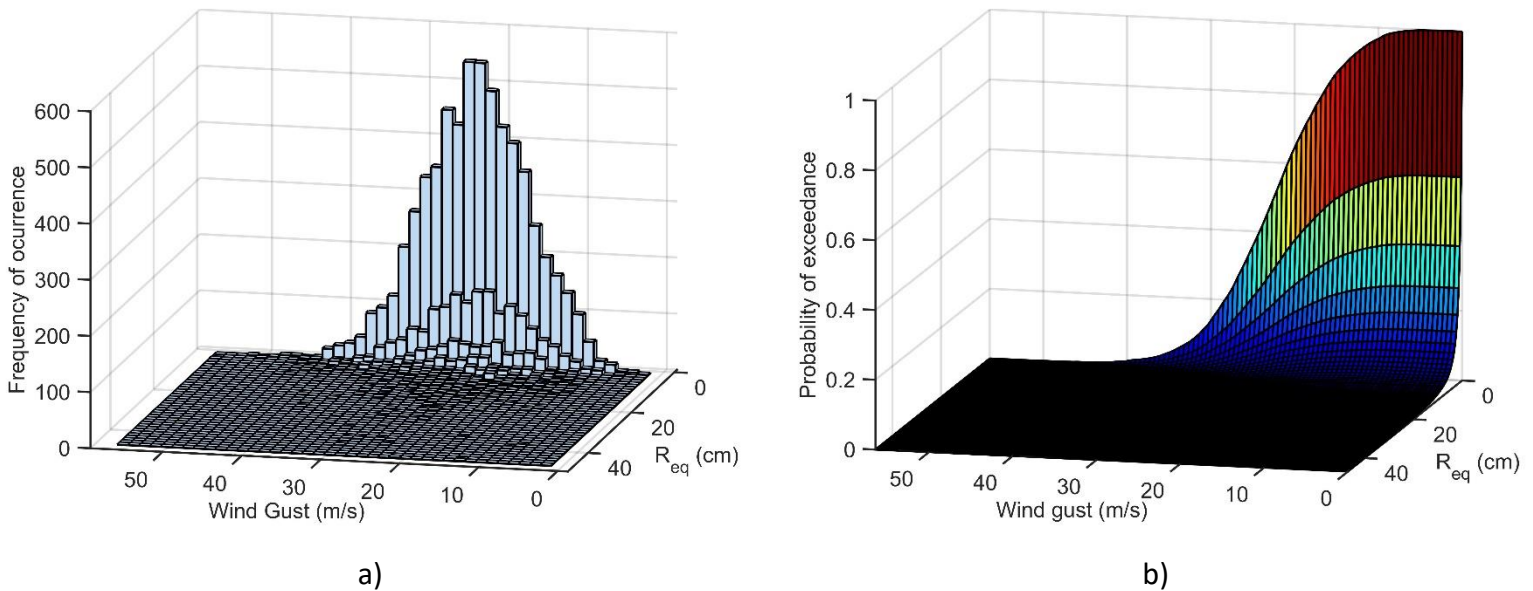


Figure 2.11. a) Joint Frequency histogram and b) Joint Probability of Exceedance curve.

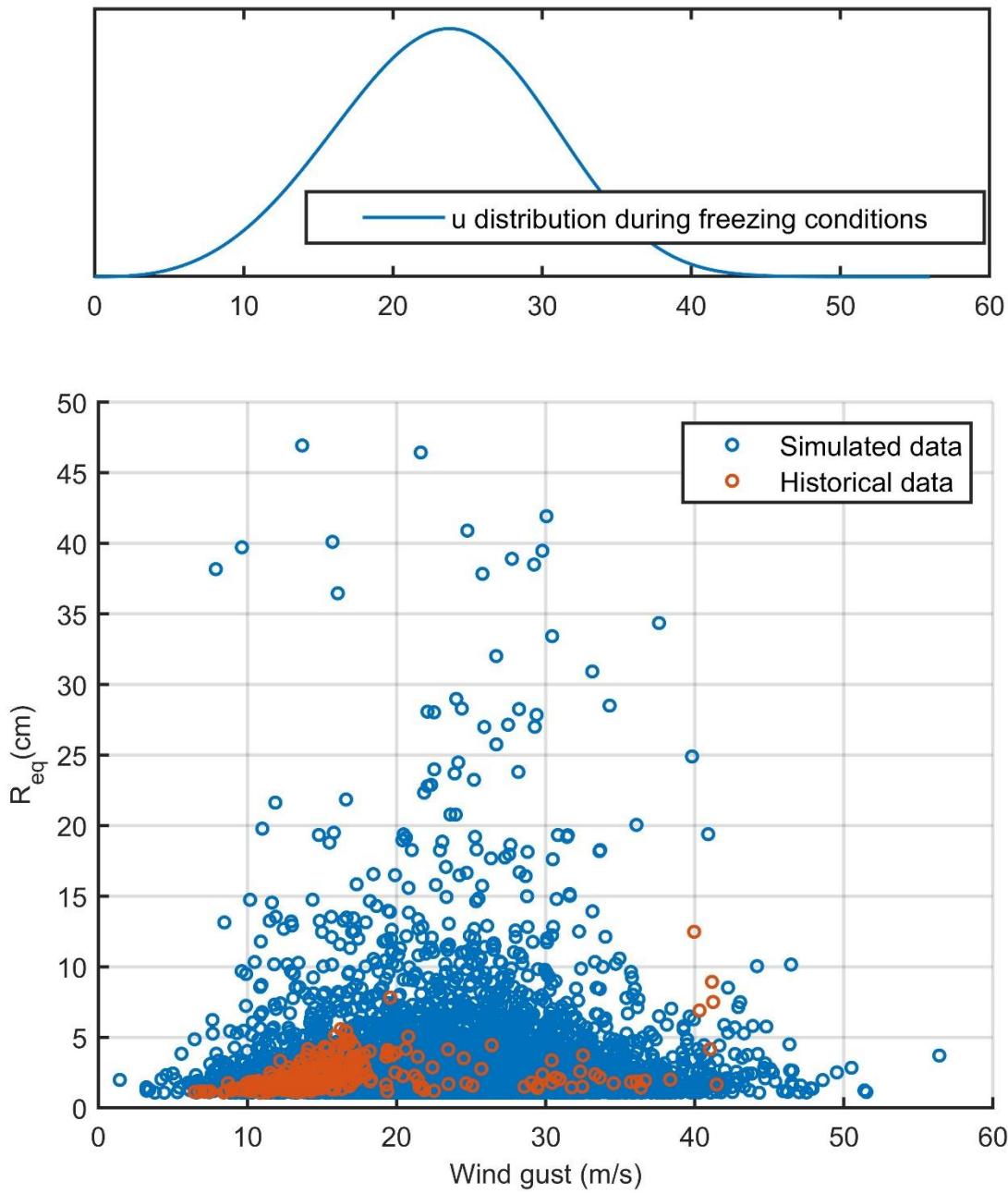


Figure 2.12. Joint scatter plot for the historical and simulated data pairs.

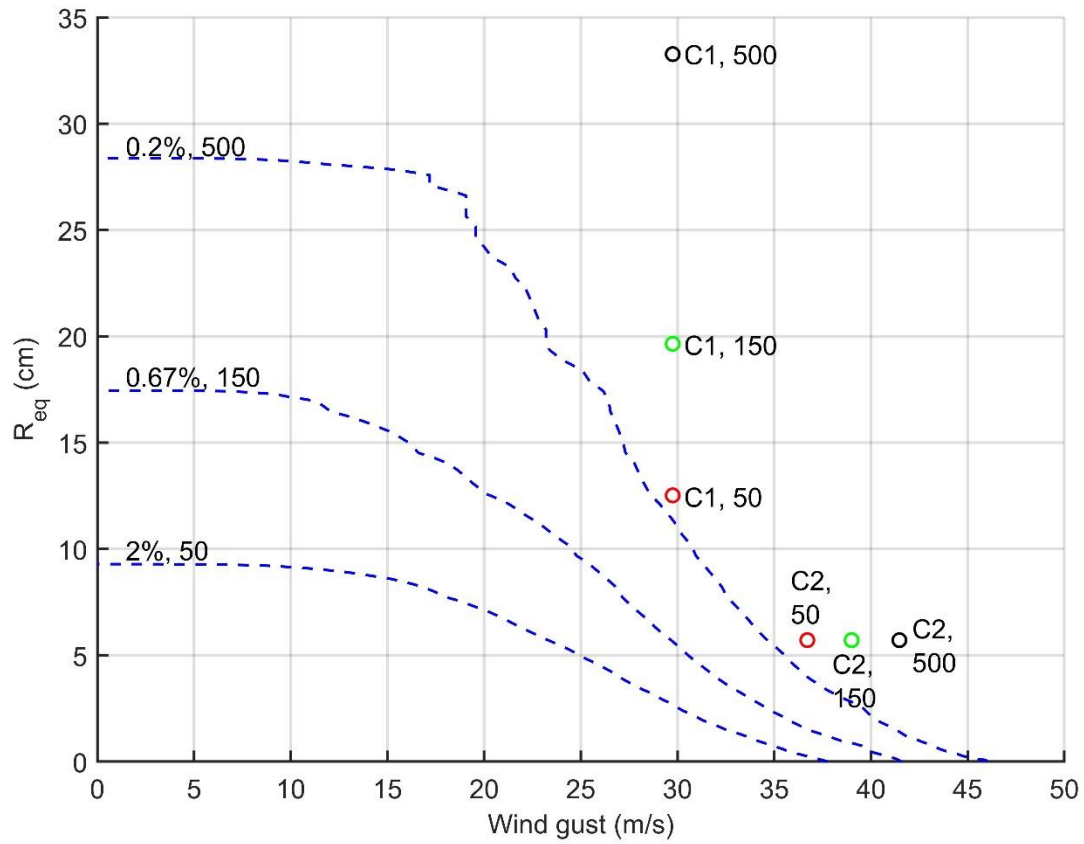


Figure 2.13. Hazard contours characterizing the joint wind and ice hazard.

Table 2.9. Reliability levels and C1 and C2 combined values from the CSA-C22.3.

Combination	R_{eq} (cm)	u (m/s)	t (years)
C1	12.52	29.75	50
C2	5.71	36.71	
C1	19.65	29.75	150
C2	5.71	39	
C1	33.27	29.75	500
C2	5.71	41.47	

2.7 Conclusions

Historical data from 16 weather stations for a mountainous terrain in British Columbia, Canada, were analyzed. Temperature data from IDW interpolations were in good agreement with WRF simulations. Wind speed hourly records based on the ANN analysis were found to have a good correlation with the WRF model, however, the ANN underpredicted the peak values above the 99 percentile. Nevertheless, Neural Networks are powerful tools which are gaining usage in the wind engineering field due to its good cost-performance ratio, providing wind speed in considerably less time than more complex methods. The ice accretion modelling resulted in 385 ice storms within a period of 15 years or an average of 25.67 storms per year, and an extreme storm recurrence rate of $38/15 = 2.53/\text{year}$. Their characteristic in terms of duration and intensity were estimated and used to select the wind speed and ice accretion data pairs and determine hazard levels from the GP distributions, respectively. The ice density to take into consideration in the design of the line corresponded to soft time with a value of $\rho_i \approx 300 \text{ (kg/m}^3\text{)}$. This ice density value in combination with the selected data pairs from the reliability levels hazard contours that that lead to the worst-case scenario can be taken into consideration for the system design. In this analysis, the combined values proposed in the CSA-C22.3 were found to be conservative. The data pairs for the 50-year return period reliability level were found to be far from the 2%, 50 hazard level and closer to the 0.2%, 500 hazard contour. The rest of the combinations were found to be far from all the contours.

However, further aerodynamic analysis at the early stage of the ice accretion process before the eventual rotation of the wire is needed for complex ice shapes for both rime and glaze ice before concluding that the standard provides overly conservative data pairs. Those complex shapes accreted on the windward side of the conductor are prone to galloping and may increase the wind and ice loading on the system exceeding the loads estimated from the contours. The present chapter provided the probabilistic characterization of the wind and ice hazard and the weather characteristics at the site.

2.8 References

- ASCE. (2010). "Minimum design loads for buildings and other structures." ASCE 7-10, Reston, VA.
- Afshar, B. B. (2016). *Wind Power Forecasting Using Artificial Neural Networks with Numerical Prediction – A Case Study for Mountainous Canada*. The University of British Columbia.
- Agustsson, H., & Nygaard, B. E. (2016). *Long Lake transmission line, British Columbia, Canada: Calculation of climatic loads* (KVT/HA/2016/R025; p. 20). Kjeller Vindteknikk.
- Aieb, A., Madani, K., Scarpa, M., Bonaccorso, B., & Lefsih, K. (2019). A new approach for processing climate missing databases applied to daily rainfall data in Soummam watershed, Algeria. *Heliyon*, 5(2), e01247. <https://doi.org/10.1016/j.heliyon.2019.e01247>
- Apaydin, H., Sonmez, F. K., & Yildirim, Y. E. (2004). Spatial interpolation techniques for climate data in the GAP region in Turkey. *Climate Research*, 28, 31–40. <https://doi.org/10.3354/cr028031>
- Basheer, I. A., & Hajmeer, M. (2000). Artificial neural networks: Fundamentals, computing, design, and application. *Journal of Microbiological Methods*, 43(1), 3–31. [https://doi.org/10.1016/S0167-7012\(00\)00201-3](https://doi.org/10.1016/S0167-7012(00)00201-3)
- Best, A. C. (1950). The size distribution of raindrops. *Quarterly Journal of the Royal Meteorological Society*, 76(327), 16–36. <https://doi.org/10.1002/qj.49707632704>
- Bushaev, V. (2018, October). *Adam latest trends in deep learning optimization*. Medium. <https://towardsdatascience.com/adam-latest-trends-in-deep-learning-optimization-6be9a291375c>

- Chen, F.-W., & Liu, C.-W. (2012). Estimation of the spatial rainfall distribution using inverse distance weighting (IDW) in the middle of Taiwan. *Paddy and Water Environment*, 10(3), 209–222. <https://doi.org/10.1007/s10333-012-0319-1>
- Druez, J., Louchez, S., & McComber, P. (1995). Ice shedding from cables. *Cold Regions Science and Technology*, 23(4), 377–388. [https://doi.org/10.1016/0165-232X\(94\)00024-R](https://doi.org/10.1016/0165-232X(94)00024-R)
- El-Fashny, K. (2002). *Modeling ice loads using passive ice meter observations in Quebec*. McGill University.
- Fan, F., Bell, K., Hill, D., & Infield, D. (2015). Wind forecasting using kriging and vector autoregressive models for dynamic line rating studies. *2015 IEEE Eindhoven PowerTech*, 1–6. <https://doi.org/10.1109/PTC.2015.7232348>
- Filik, Ü. B., & Filik, T. (2017). Wind Speed Prediction Using Artificial Neural Networks Based on Multiple Local Measurements in Eskisehir. *Energy Procedia*, 107, 264–269. <https://doi.org/10.1016/j.egypro.2016.12.147>
- Finstad, K. J., Lozowski, E. P., & Gates, E. M. (1988). A computational investigation of water droplets trajectories. *Journal of Atmospheric and Oceanic Technology*, 5, 160–170.
- Fu, P. (2004). *Modelling and simulation of the ice accretion process on fixed or rotating cylindrical objects by the boundary element method* [Université du Québec à Chicoutimi]. <https://doi.org/10.1522/18326611>
- Fu, P., Farzaneh, M., & Bouchard, G. (2006). Two-dimensional modelling of the ice accretion process on transmission line wires and conductors. *Cold Regions Science and Technology*, 46(2), 132–146. <https://doi.org/10.1016/j.coldregions.2006.06.004>
- Gemmer, M., Becker, S., & Jiang, T. (2004). Observed monthly precipitation trends in China 1951–2002. *Theoretical and Applied Climatology*, 77(1–2), 39–45. <https://doi.org/10.1007/s00704-003-0018-3>

- Gumbel, E. . J. (1954). Statistical Theory of Extreme Values and Some Practical Applications; a Series of Lectures. *Journal of the Royal Aeronautical Society*, 58(527), 792–793.
- Harstveit, D. K., & Vindteknikk, K. (2009). Using Metar—Data to Calculate In-Cloud Icing on a Mountain Site near by the Airport. *IWAIS XIII*, 122, 9.
- He, Y., & Wang, K. (2020). Contrast patterns and trends of lapse rates calculated from near-surface air and land surface temperatures in China from 1961 to 2014. *Science Bulletin*, 65(14), 1217–1224. <https://doi.org/10.1016/j.scib.2020.04.001>
- Hinton, G. E., Srivastava, N., Krizhevsky, A., Sutskever, I., & Salakhutdinov, R. R. (2012). *Improving neural networks by preventing co-adaptation of feature detectors* [Academic]. <http://arxiv.org/abs/1207.0580>
- Jubayer, C. M., & Hangan, H. (2018). A hybrid approach for evaluating wind flow over a complex terrain. *Journal of Wind Engineering and Industrial Aerodynamics*, 175, 65–76. <https://doi.org/10.1016/j.jweia.2018.01.037>
- Kingma, D. P., & Ba, J. (2017, January 29). *Adam: A Method for Stochastic Optimization*. International Conference on Learning Representations, San Diego, CA. <http://arxiv.org/abs/1412.6980>
- Krose, B., & Van Der Smagt, P. (1996). *An introduction to Neural Networks* (Eighth edition). The University of Amsterdam.
- Kurtzman, D., & Kadmon, R. (1999). Mapping of temperature variables in Israel: A comparison of different interpolation methods. *Climate Research*, 13, 33–43. <https://doi.org/10.3354/cr013033>
- Langmuir, I., & Blodgett, Katherine. (1946). *A mathematical investigation of water droplet trajectories*. Army Air Forces Headquarters, Air Technical Service Command. <https://catalog.hathitrust.org/Record/101738423>

- Lawan, S. M., Abidin, W. A. W. Z., & Masri, T. (2020). Implementation of a topographic artificial neural network wind speed prediction model for assessing onshore wind power potential in Sibuluan, Sarawak. *The Egyptian Journal of Remote Sensing and Space Science*, 23(1), 21–34. <https://doi.org/10.1016/j.ejrs.2019.08.003>
- Ličar, M. (2016). *Numerical Modelling of Icing on Power Lines* [Seminar].
- Macklin, W. C. (1962). The density and structure of ice formed by accretion. *Quarterly Journal of the Royal Meteorological Society*, 88, 30–50.
- Makkonen, L. (1984). Modeling of ice accretion on wires. *Journal of Applied Meteorology and Climatology*, 23, 929–939.
- Makkonen, L. (2000). Models for the growth of rime, glaze, icicles and wet snow on structures. *Philosophical Transactions of the Royal Society of London. Series A: Mathematical, Physical and Engineering Sciences*, 358(1776), 2913–2939. <https://doi.org/10.1098/rsta.2000.0690>
- McComber, P., & Touzot, G. (1981). Calculation of the Impingement of Cloud Droplets in a Cylinder by the Finite-Element Model. *American Meteorological Society*, 38, 1027–1036.
- Mekis, E., & Hogg, W. D. (1999). Rehabilitation and analysis of Canadian daily precipitation time series. *Atmosphere-Ocean*, 37(1), 53–85. <https://doi.org/10.1080/07055900.1999.9649621>
- National Standard of Canada, (2010). *Design criteria of overhead transmission lines* (CAN/CSA-C22.3). Ontario, Canada
- Pereira, F. C., & Borysov, S. S. (2019). Machine Learning Fundamentals. In *Mobility Patterns, Big Data and Transport Analytics* (pp. 9–29). Elsevier. <https://doi.org/10.1016/B978-0-12-812970-8.00002-6>

- Philippopoulos, K., & Deligiorgi, D. (2012). Application of artificial neural networks for the spatial estimation of wind speed in a coastal region with complex topography. *Renewable Energy*, 38(1), 75–82. <https://doi.org/10.1016/j.renene.2011.07.007>
- Poots, G., & Skelton, P. L. I. (1995). Simulation of wet-snow accretion by axial growth on a transmission line conductor. *Applied Mathematical Modelling*, 19(9), 514–518. [https://doi.org/10.1016/0307-904X\(95\)00012-9](https://doi.org/10.1016/0307-904X(95)00012-9)
- Roberge, M. (2005). *The Physics of Wet Snow Accreted on an Overhead Wire*. McGill University.
- Rosowsky, D. V., & Wang, Y. (2014). Joint Wind-Snow Hazard Characterization for Reduced Reference Periods. *Journal of Performance of Constructed Facilities*, 28(1), 121–127. [https://doi.org/10.1061/\(ASCE\)CF.1943-5509.0000385](https://doi.org/10.1061/(ASCE)CF.1943-5509.0000385)
- Rossi, A., Jubayer, C., Koss, H., Arriaga, D., & Hangan, H. (2020). Combined effects of wind and atmospheric icing on overhead transmission lines. *Journal of Wind Engineering and Industrial Aerodynamics*, 204, 104271. <https://doi.org/10.1016/j.jweia.2020.104271>
- Simiu, E., & Scanlan, R. H. (1996). *Winds Effects on Structures: Fundamentals and Applications to Design*. Wiley.
- Sinh, H. N., Lombardo, F. T., Letchford, C. W., & Rosowsky, D. V. (2016). Characterization of Joint Wind and Ice Hazard in Midwestern United States. *Natural Hazards Review*, 17(3), 04016004. [https://doi.org/10.1061/\(ASCE\)NH.1527-6996.0000221](https://doi.org/10.1061/(ASCE)NH.1527-6996.0000221)
- Smithson, P., Addison, K., & Atkinson, K. (2002). *Fundamentals of the Physical Environment*. Psychology Press.
- Thompson, G., Politovich, M. K., & Rasmussen, R. M. (2017). A Numerical Weather Model's Ability to Predict Characteristics of Aircraft Icing Environments. *Weather and Forecasting*, 32(1), 207–221. <https://doi.org/10.1175/WAF-D-16-0125.1>

Weibull, W. (1939). A Statistical Theory of the Strength of Materials. *Ing. Vetenskapa Acad. Handlingar*, 151, 1–45.

Willmott, C. J., & Matsuura, K. (2005). Advantages of the mean absolute error (MAE) over the root mean square error (RMSE) in assessing average model performance. *Climate Research*, 30, 79–82. <https://doi.org/10.3354/cr030079>

Chapter 3

3 Vertical galloping on complex shapes of iced conductors

In this chapter, for aerodynamic analyses, the asymmetric ice profile at the early stage of the accretion during an icing event need to be taken into consideration instead of the radial ice accretion considered in the Chapter 2. In the case of rime ice, a crescent shape by axial growth following a cosine law in the windward side of the conductor have been proposed and observed to be a good representation of real rime ice accretion shape (Poots & Skelton, 1995). The reason behind this process is due to the instantaneous freezing of the supercooled water droplet after the collision with the cable. Due to its well representation of the real rime ice deposit, several authors have considered this shape to perform aerodynamic analysis on iced conductors. Liu et al., (2015) performed wind tunnel tests and computational fluid dynamics (CFD) simulations for a single conductor and studied the effect of the wake on a bundle conductor. Rossi et al., (2020) obtained aerodynamic coefficients from a force balance wind tunnel experiments considering a range of eccentricities of the crescent shape ice deposit and obtained the tension transmitted to the tower on the onset of galloping. Borna et al., (2012) identified instabilities on the same ice shape by performing a two-dimensional two-way fluid structure interaction (FSI) model aiming to capture the maximum displacements produced by the vertical galloping and the horizontal displacements within a range of wind velocities.

Glaze ice, on the other hand, is more difficult to characterize due to its wet growth process. For this case, assuming the crescent shape by axial growth may not be accurate because the droplets do not freeze instantaneously after collision. Instead, the freezing rate is controlled by the latent heat release and a fraction of the impinging water droplet runs off the cable due to gravity (Makkonen, 2000). For this reason, the mass may concentrate beneath the surface creating more complex shapes. The airflow past the cylindrical shape of the cable must be modelled keeping track of the water droplets trajectories, evaluating the local collision efficiency, and solving the heat balance equation to eventually estimate the new ice shape at each time step of the process

(Fu et al., 2006). Modelling complex ice shapes is a complex iterative process whose details can be found in Fu, (2004), Fu et al., (2006), or McComber & Touzot, (1981), for example. In addition, this procedure can be performed by using icing software such as the Nasa LEWICE, the CANICE model, or the Ansys FENSAP-ICE, to name a few (Fu et al., 2006).

In this chapter, both rime and glaze ice shapes are considered for stability analysis. The rime ice analysis performed by Rossi et al., (2020) is taken as a reference for comparison purposes with two more complex ice shapes. The complex glaze ice shapes are taken from previous analysis published by Fu et al., (2006). The shapes are selected based on the similarity between the characteristics (wind speed and temperature) considered in Fu et al., (2006) for the estimation of the ice shape and the characteristics observed in Chapter 2. The Den Hartog, (1932) principle is applied for the identification of critical ranges where instabilities may occur and the linear theory of free vibrations of a suspended cable is used to transfer the loads acting on a one-degree-of-freedom system produced on the onset of vertical galloping to the transmission tower.

3.1 Ice profiles

The ice profiles for rime and glaze were selected based on previous observations and considering the physical process where they may form:

3.1.1 Rime ice profile

Poots & Skelton, (1995) have demonstrated that assuming a unity accretion efficiency, the ice deposit on the windward side of the conductor follows a cosine law shown in Figure 3.1. This shape has been well accepted for a dry growth process due to its good agreement with field observations (Poots & Skelton, 1995). The ice profile is assumed to be uniformly distributed along the entire length of the cable and no rotation conditions for the one-degree-of-freedom system

analysis. The ice eccentricity considered here for the rime ice profile is set to $t/d=1$ (see Figure 3.1).

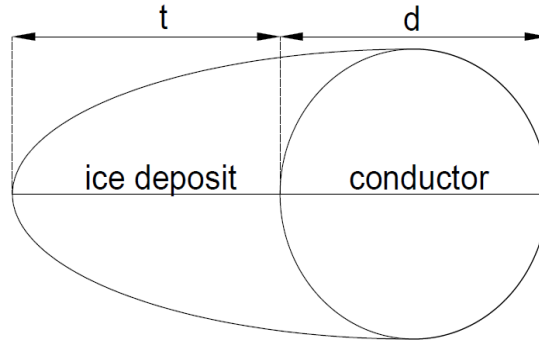


Figure 3.1. Rime ice profile (Poots & Skelton, 1995).

The profile form Figure 3.1 follows Equation (3.1) proposed by Poots & Skelton, (1995).

$$\sigma_i = \sigma_0 \cos \gamma(r_B) \quad (3.1)$$

where σ_i denotes the local fraction of the incoming particle, $\sigma_0 < 1$ is a constant, and $\gamma(r_B)$ is the angle between the impinging trajectory and the normal to the surface at the point r_B .

3.1.2 Glaze ice profile

From the most severe storms in terms of icing intensity R_{eq} (radial ice deposit) and its weather characteristics shown in Table 2.5, it is possible to observe that the average of the mean velocities \bar{u} presented during the length of the icing events is 15.46 m/s. Glaze ice shapes produced by water droplets flowing with the streamlines considering a similar free stream velocity were found in the literature and used for this analysis. The selected profiles are those modelled for wet and

semi wet growth conditions presented in Fu et al., (2006) (Figure 3.2). Both profiles correspond to icing simulations considering a wind speed $u = 10 \text{ m/s}$, and temperature (T) conditions of $-10 \text{ }^\circ\text{C}$ and $-5 \text{ }^\circ\text{C}$ for Figure 3.2a (S1) and Figure 3.2b (S2), respectively. The eccentricity for the S1 profile is $t/d = 0.72$, while for the S2 profile is $t/d = 0.36$. Since the S1 profile is characteristic of semi wet growth conditions, it can be considered a combination of rime and glaze ice formation (Fu et al., 2006).

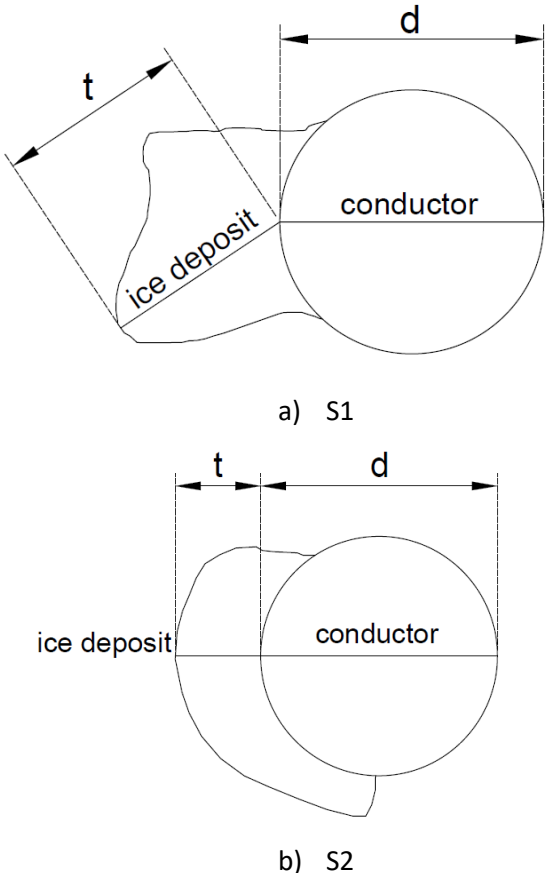


Figure 3.2. a) S1 profile for $u = 10 \text{ m/s}$, and $T = -10 \text{ }^\circ\text{C}$ in semi wet growth conditions, and b) S2 profile for $u = 10 \text{ m/s}$, and $T = -5 \text{ }^\circ\text{C}$ in wet growth conditions (Fu et al., 2006).

3.2 CFD Setup

The ice profiles described in the past subsections were analyzed by performing Computational Fluid Dynamics (CFD) simulations to obtain the aerodynamic lift (Cl) and drag (Cd) coefficients. The simulations were performed in the Fluent module of Ansys 18.1, and the recommendations from Rossi, (2018) were followed for the analysis setup. Steady state simulations were performed using the RANS $k - \omega$ SST turbulence model due to its good prediction of Cd and Cl at the proximity of the wall which in this case is the ice profile. The boundary conditions were located far from the profile to let the flow develop along the domain as shown in Figure 3.4a. A circular shape around the profile was set to act as a body of influence to refine the mesh in the zone of interest and a mesh growth rate of 1.05 was applied. In this way, the mesh density decreases as the elements get farther from the profile to considerably reduce the computational cost, which was an important goal of the analysis. Additionally, to keep the computational cost as low as possible, a sensitivity analysis was carried out by varying the value of the first layer thickness. Theoretically, to achieve reliable Cd and Cl from RANS models, the value of y^+ should be within the viscous sublayer range of the boundary layer profile (Figure 3.3). Nevertheless, to achieve a value of y^+ in the viscous sublayer, y^+ should be < 1 , which is very difficult to accomplish due to the small value of the first layer thickness needed which tends to increase the number of mesh elements. For this reason, a preliminary study was performed setting the values of y^+ to 1, 5 and 10 by performing the following calculations (Sijal, 2019):

$$C_f = 0.058/R_e^{0.2} \quad (3.2)$$

$$R_e = \frac{\rho_a u d_c}{\mu} \quad (3.3)$$

$$\tau_w = 0.5 C_f \rho_a u^2 \quad (3.4)$$

$$u_\tau = \sqrt{\frac{\tau_w}{\rho_a}} \quad (3.5)$$

$$y^+ = \frac{u_\tau y \rho_a}{\mu} \quad (3.6)$$

where C_f is the skin friction coefficient, R_e is the Reynolds number, d_c is the characteristic length of the iced conductor, μ is the air viscosity, τ_w is the wall shear stress, u_τ is the friction velocity, y^+ is the non-dimensional height, and y is the first layer thickness. Table 3.1 shows the results from the sensitivity analysis considering the rime ice profile and tested for three different wind velocities. From the table, it can be observed that the number of mesh elements drastically increases when decreasing the value of y^+ , while the differences in Cd and Cl are in average 5% comparing the results for $y^+ = 10$ and $y^+ = 1$. Hence, it was accepted that for the purpose of this study using a value of $y^+ = 10$ ensures the best cost-effective ratio. This analysis was taken into consideration for the three ice profiles and y^+ was set to 10 for each case. The final mesh and the detail of first layer thickness for the rime profile are shown in Figure 3.4b. The mesh quality was also evaluated by monitoring two quality metrics such as the element quality and cells skewness. From Figure 3.5a and b, it can be observed that the described procedure resulted in high quality elements and low cell skewness for the rime ice profile. The mesh and quality metrics for S1 and S2 profiles can be consulted in Appendix B.

For the validation analysis, the results from the present study and those from wind tunnel tests reported in Rossi, (2018) for the same rime ice profile and wind velocity were compared and are detailed in subsection 3.4 of this chapter. The overall differences between the CFD simulations and the wind tunnel tests from Rossi et al., (2020) were of the order of 5% for Cd and 8% for Cl .

The ice profiles were rotated considering three different sections. Section one was considered from the angle of attack $\alpha = 0^\circ$ to 30° with $\Delta\alpha = 5^\circ$, section two from $\alpha = 30^\circ$ to 150° with $\Delta\alpha =$

10°, and section three from $\alpha = 150^\circ$ to 180° with $\Delta\alpha = 5^\circ$. The direction from where α was measured is illustrated in Figure 3.6. A total of 25 data points for the construction of C_l and C_d curves with respect to α were obtain for each profile after the CFD simulations. The outcome of the analysis is shown in subsection 3.4.

Table 3.1. Sensitivity analysis for the rime ice profile.

y^+	$u \left(\frac{m}{s}\right)$	C_d	C_l	Elements
10	7.92	0.4206	1.426097	60,000
	12.87	0.5099	1.617076	
	18.81	0.5013	1.582942	
5	7.92	0.4249	1.456055	100,000
	12.87	0.498339	1.588819	
	18.81	0.463913	1.536678	
1	7.92	0.402645	1.49563	260,000
	12.87	0.4882	1.5492	
	18.81	0.4622	1.5334	

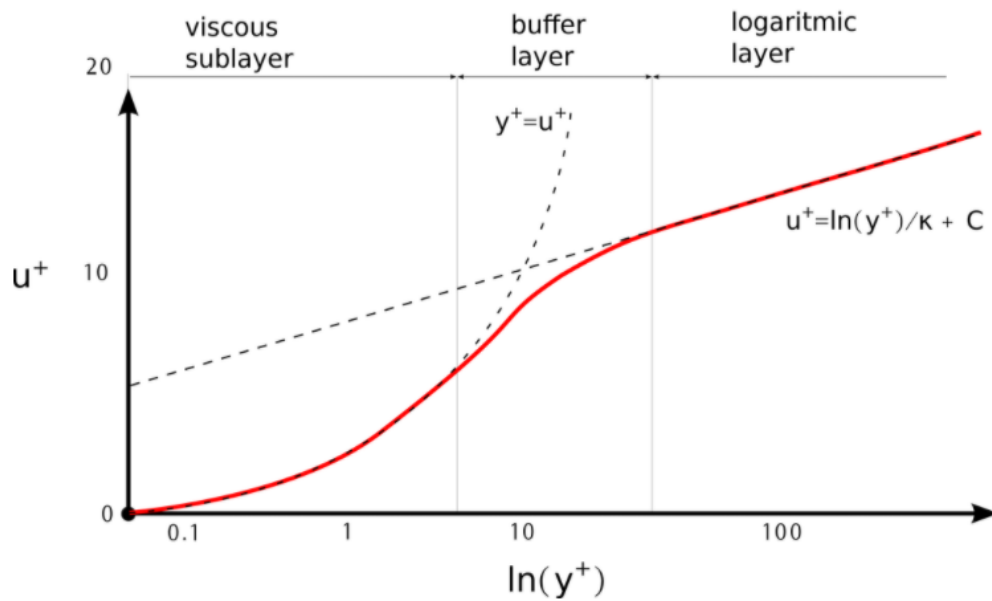
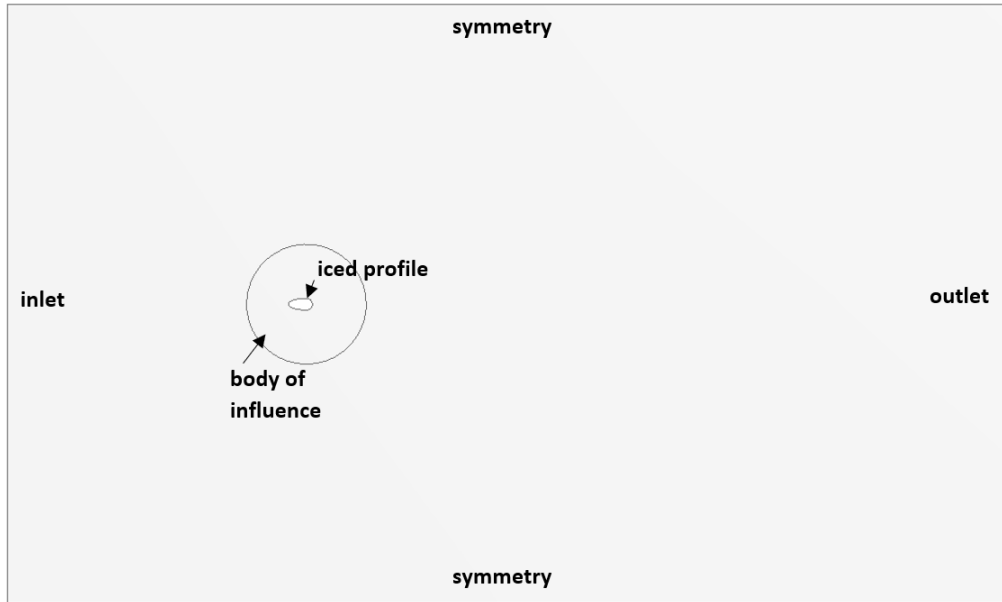
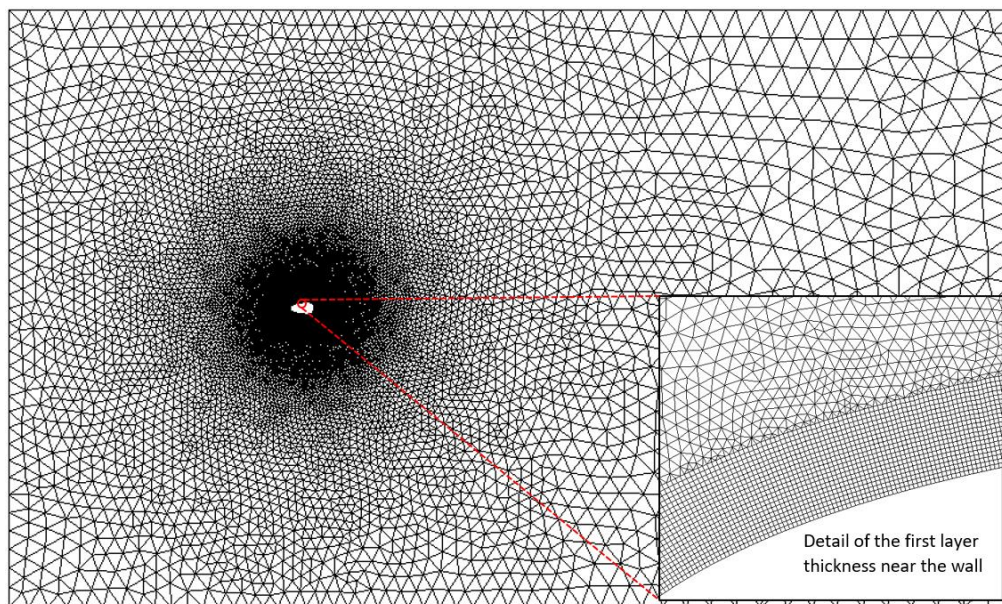


Figure 3.3. Boundary Layer near the wall (Sijal, 2019).

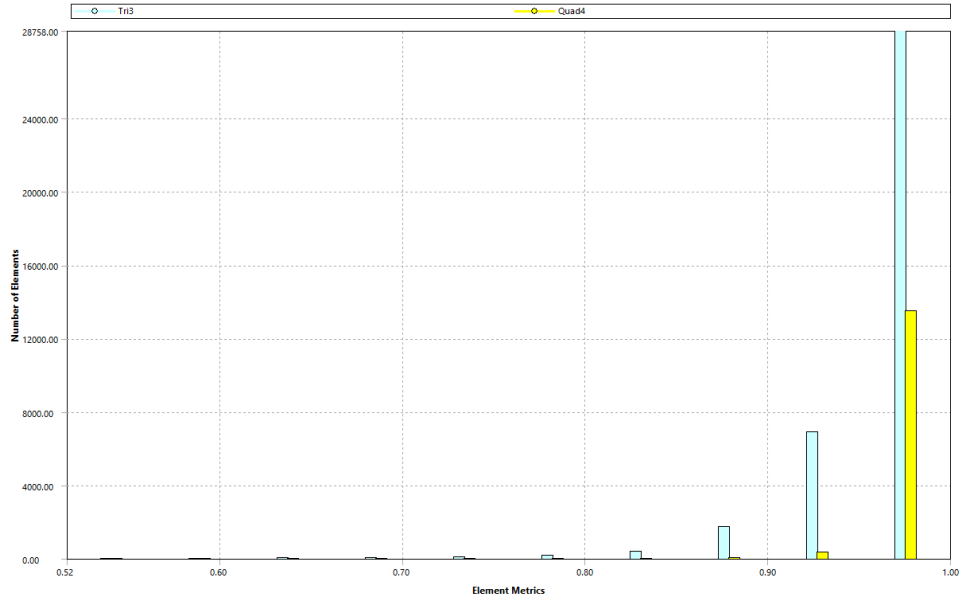


a)

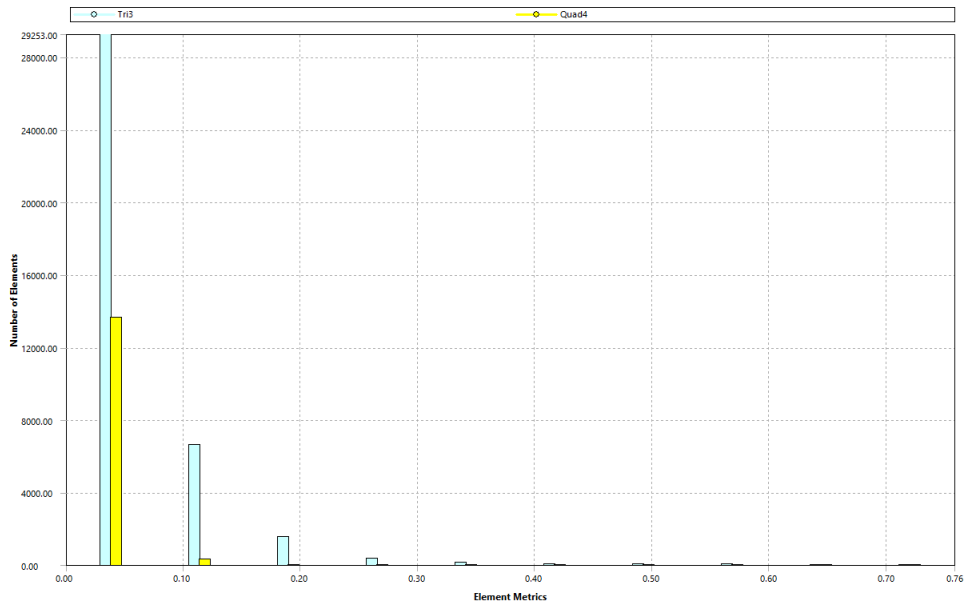


b)

Figure 3.4. a) Boundary conditions and b) final mesh considered for the rime ice profile with a total of $\approx 60,000$ elements, $y^+ = 10$, average element quality = 0.97, and average skewness = 0.03.



a)



b)

Figure 3.5. Mesh metrics for the rime ice profile: a) Element Quality, and b) Cells Skewness.

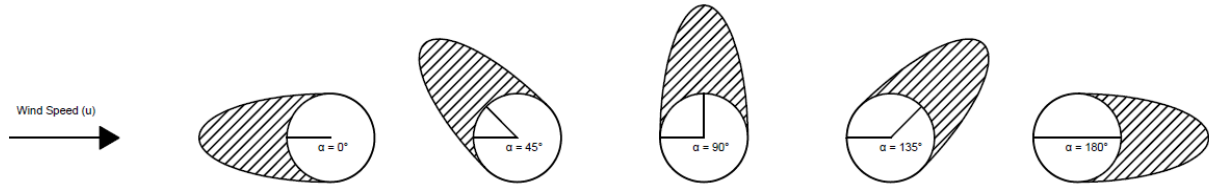


Figure 3.6. Rotation of the ice profiles.

3.3 Structural Analysis

This section is divided into 4 parts. First, the calculations of the static loads produced by both the ice mass accreted on the cable and the wind speed are described. The eigen value analysis for the estimation of the natural frequencies of the system is carried out in the second part. Third, the necessary conditions for galloping to occur are presented. Finally, the procedure for estimating the extra tension transmitted to the tower on the onset of galloping is developed.

3.3.1 Static loads

The horizontal component of the tension transmitted to the tower due to the vertical load can be calculated as follows (Irvine & Caughey, 1974):

$$H = \frac{m_{tot} g L_i^2}{8 s} \quad (3.7)$$

where m_{tot} represents the mass per unit length considering the ice deposit and the cable itself, $g = 9.81 \text{ (m/s}^2\text{)}$, $L_i = 172.4 \text{ (m)}$ is the length of the span, and $s = 3.39 \text{ (m)}$ is the sag at the mid span. For the calculation of m_{tot} , a mass per unit length of $w_c = 1.3 \text{ (kg/m)}$ was assumed for the cable. For rime ice, the density distribution from Figure 2.9 showed that $\rho_i = 400 \text{ (kg/m}^3\text{)}$ may

be a reasonable value to take into consideration for the design. For S1 and S2 profiles, a value of $\rho_i = 900 \text{ (kg/m}^3\text{)}$ was taken into consideration, which is characteristic of glaze ice.

For the horizontal wind load, the correspondent tension can be obtained by applying the CSA-C22.3 standard.

$$Ac = q_0 C_d G_c G_L d_c L_i \quad (3.8)$$

where $q_0 = \frac{1}{2} \rho_a u^2$, $\rho_a = 1.225 \text{ (kg/m}^3\text{)}$ is the air density, $C_d = 1.2$ is the drag coefficient, $G_c = 2.1$ is the combined wind factor which depends on the height and terrain categories of the line location, and $G_L = 1$ is the span factor. The combined data pairs of ice accretion and wind speed were taken from Section 2. The correspondent ice accretion shape for a 10 m/s wind gust was selected from each hazard contour presented in Figure 3.7 and both values were considered in the calculations of Equation (3.7) and Equation (3.8). Note that the ice accretion (R_{eq}) from Figure 3.7 considers a radial ice thickness along the length of the cable instead of a crescent ice deposit in the windward side. The fact of considering a radial shape for the static analysis and then adding its contribution to the dynamic effects may lead to conservative load estimations. However, for design purposes, this action was considered adequate in covering the possible uncertainties when dealing with the joint wind and ice hazard.

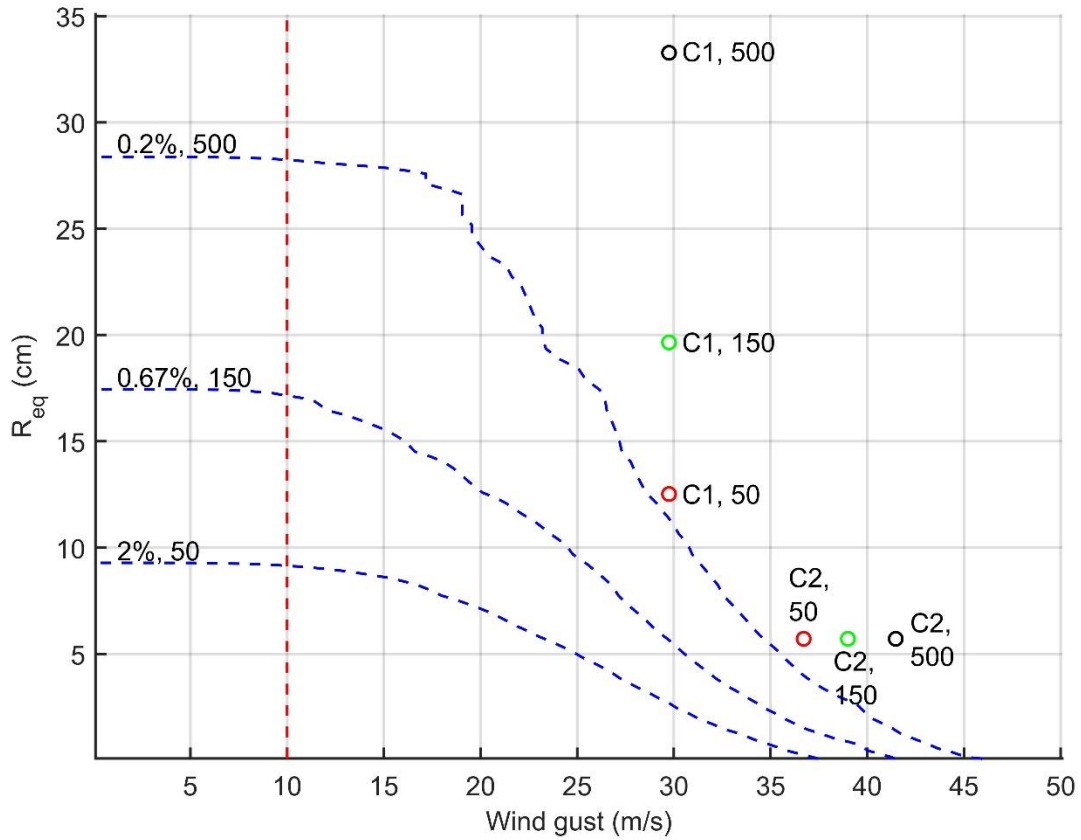


Figure 3.7. Selected ice accretion data pair for a 10 m/s wind gust velocity.

3.3.2 Natural Frequencies of the system

The linear theory of free vibrations of a suspended cable proposed by Irvine & Caughey, (1974) is capable to describe the dynamic behaviour of transmission line systems which present a ratio sag to span of 1:8 or less. The mode shapes of the system and its natural frequencies can be obtained by applying the following equations (Irvine & Caughey, 1974):

$$\varphi(x) = 1 - \tan\left(\frac{1}{2} \beta L\right) \sin(\beta x) - \cos(\beta x) \quad (3.9)$$

$$\beta = \left(\frac{m_s \omega_n^2}{H} \right)^{\frac{1}{2}} \quad (3.10)$$

where ω_n is the n^{th} angular natural frequency (rad/s), m_s is the structural mass, H is the horizontal tension component considering just the mass of the cable in Equation (3.7), and βL specifies the particular symmetric vertical modal component which can be graphically estimated (Figure 3.8) by finding the non-zero roots of Equation (3.11).

$$\tan\left(\frac{1}{2}\beta L\right) = \left(\frac{1}{2}\beta L\right) - \left(\frac{4}{\lambda^2}\right)\left(\frac{1}{2}\beta L\right)^3 \quad (3.11)$$

$$\lambda^2 = \left(\frac{8s}{L}\right)^2 \frac{L_i}{(HL_e/E_c A_c)} \quad (3.12)$$

where λ is a parameter involving cable geometry and elasticity, $L_e = L_i \left(1 + 8[s/L_i]^2\right)$, E_c is the modulus of elasticity of the cable, and A_c is the area of the cable. Note that this analysis is limited to the symmetric vertical modal components of the system since the antisymmetric vertical modal components are not contributing to the tension transmitted to the tower due to the motion of the cable (Irvine & Caughey, 1974). In addition, according to Lilien et al., (2005), the oscillations produced by the vertical galloping have frequencies lower than 1 Hz and thus the analysis is limited to the first two symmetric vertical modal components of the line. From Figure 3.8, the value of $\frac{1}{2}\beta L$ for the first two symmetric modes are found when the red curve representing the right side of Equation (3.11) intersects the blue curves representing the left side of the equation. The intersections are represented by the black broken lines in the figure. Finding $\frac{1}{2}\beta L$ from Figure 3.8 and solving for Equation (3.10), the two symmetric natural frequencies for the one-degree-of-freedom system shown in Table 3.2 were obtained. Note that even though the two natural frequencies are close from each other, here, the effect of close modes was neglected and each mode was treated independently.

Table 3.2. Natural frequencies of the conductor.

φ_n	$\frac{1}{2}\beta L$	ω_n (rad/s)	f_n (Hz)
1 st	3.76	4.53	0.72
2 nd	5.10	6.13	0.98

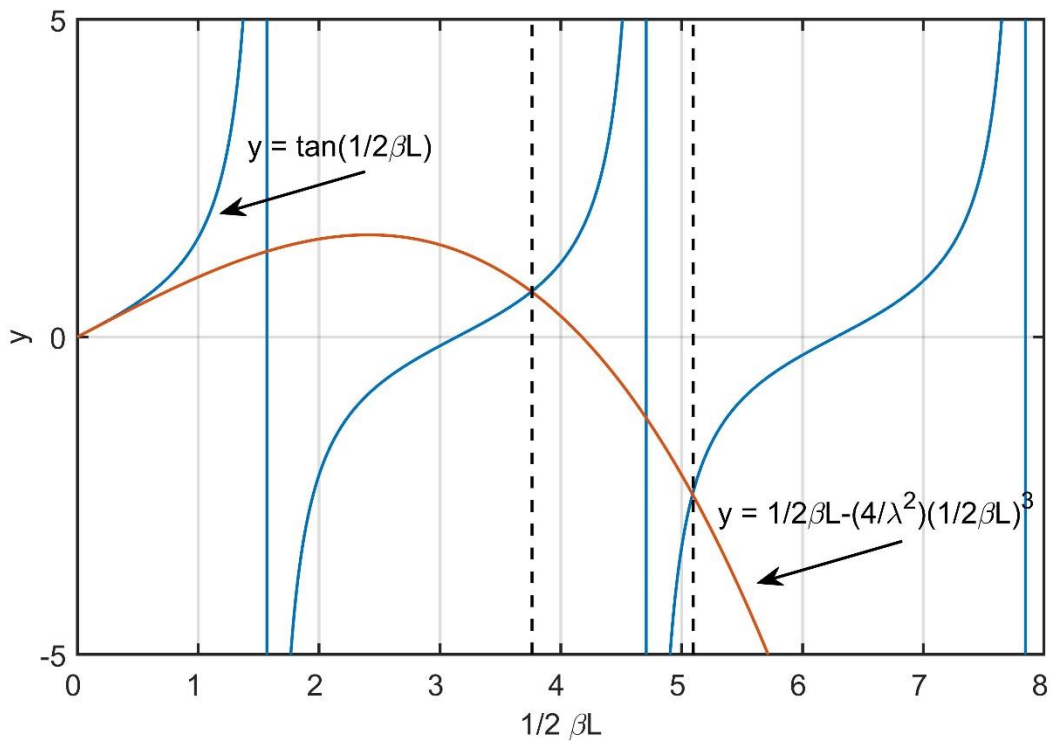


Figure 3.8. Graphic representation of the non-zero roots of Equation (3.11).

3.3.3 Galloping Conditions

There are three necessary conditions that must be fulfilled for the galloping to occur. First, the Den Hartog's coefficient from Equation (1.1) must be negative (Den Hartog, 1932). The interpretation behind this statement is that the effect of the negative slope of the lift curve with respect to the angle of attack must be greater than the damping effects of the drag to present

aerodynamic instabilities (Den Hartog, 1932). When a_g stays negative for a large range of $\Delta\alpha$, the contribution to the maximum modal amplitude will increase, as will be discussed in the following subsection. The second condition depends on the wind speed and the structural properties of the transmission line system. When the free stream velocity surpasses the critical wind speed, the risk of experience vertical galloping will be presented (Scruton & Flint, 1964).

$$V_c = \frac{2 S_c f_n d_c}{a_g} \quad (3.13)$$

where V_c is the critical wind speed, $S_c = \frac{4\pi \xi_s m_s}{\rho_0 d_c^2}$ is the Scruton number, f_n is the natural frequency (Hz) of the structure, $\xi_s = 0.005$ is a typical structural damping ratio for transmission lines taken from literature and considered for the two mode shapes (Borna, 2014; Rossi, 2018), and m_s is the structural mass per unit length. The third and final condition refers to the unbalance between the aerodynamic and structural damping.

$$\xi_s + \xi_a < 0 \quad (3.14)$$

where

$$\xi_a = \frac{\rho_0 d_c u}{4m_s \omega_n} a_g \quad (3.15)$$

is the aerodynamic damping ratio. At this point, the structure is not capable of mitigating the aerodynamic damping force, and it stays in a self-excited oscillatory motion characterized by high amplitudes and low frequencies. If the three conditions are fulfilled, galloping is assumed to fully develop.

3.3.4 Extra tension on the onset of galloping

The final purpose of the structural design is to obtain the design loads considering all the possible events acting on the system. In the case of the vertical galloping, its contribution to the total tension can be obtained by applying the following procedure (Rossi, 2018):

$$m_n = \int_0^{L_i} m_s \varphi_n^2(x) \quad (3.16)$$

$$MPF_n = \frac{\int_0^{L_i} m_s \varphi_n(x) dx}{m_n} \quad (3.17)$$

$$v_n(x) = A_n \varphi_n(x) MPF_n \quad (3.18)$$

$$A_n = \frac{\Delta \alpha u}{\omega_n} \quad (3.19)$$

$$v(x) = \sqrt{\sum_{n=1}^N v_n^2(x)} \quad (3.20)$$

$$h = \frac{E_c A_c 8s}{L_e L_i^2} \int_0^{L_i} v(x) dx \quad (3.21)$$

where m_n is the modal mass, MPF_n is the modal participation factor, $v_n(x)$ are the displacements for the n^{th} mode, A_n is the maximum modal amplitude, $\Delta \alpha$ is the range where $a_g < 0$, $v(x)$ is the total displacement of the cable (considering both symmetric modes), and h is the extra tension produced on the onset of the instability.

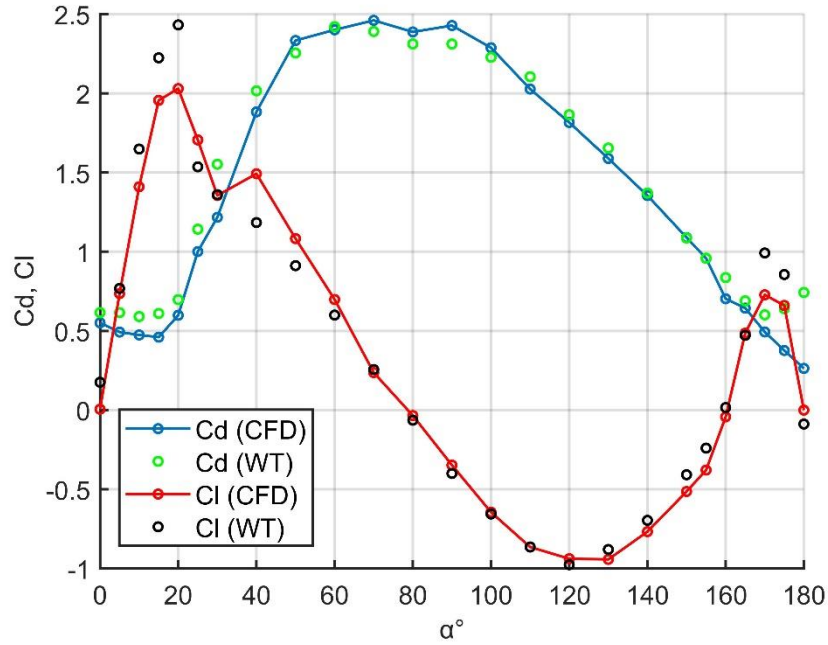
3.4 Results and discussion

The results from the CFD analysis are shown in Figure 3.9 for the three ice profiles considered. Figure 3.9a shows a comparison with the aerodynamic coefficients reported in Rossi et al., (2020) (WT) for the rime profile and overall a good fit can be observed. The aerodynamic coefficients from the CFD analysis underestimated the C_l peak values at $\alpha = 20^\circ$ and 170° obtained from the wind tunnel tests. These specific zones of the C_l curve are critical since instabilities may occur within the $\Delta\alpha$ range where the slope changes drastically from positive to negative. For this reason, the peak values from the wind tunnel tests reported in Rossi et al., (2020) were taken into consideration for the a_g calculations shown in Equation (1.1). The C_d curve from Figure 3.9a also shows a general good fit between both analyses. As expected, the maximum C_d was obtained between $\alpha = 70^\circ - 90^\circ$ due to the vertical position of the profile at this wind angle of attack. Figure 3.9b and c show the coefficients for the S1 and S2 profiles, respectively. In this case, the interpretation of the trends for the C_d and C_l curves are not as intuitive as for the rime profile due to their irregular shapes. The C_d curves seems to have a flatter shape, specially for the S2 profile. The S1 profile has the change in the C_l slope at $\alpha = 70^\circ$, while two drastic changes can be observed for the S2 profile at $\alpha = 70^\circ$ and 140° .

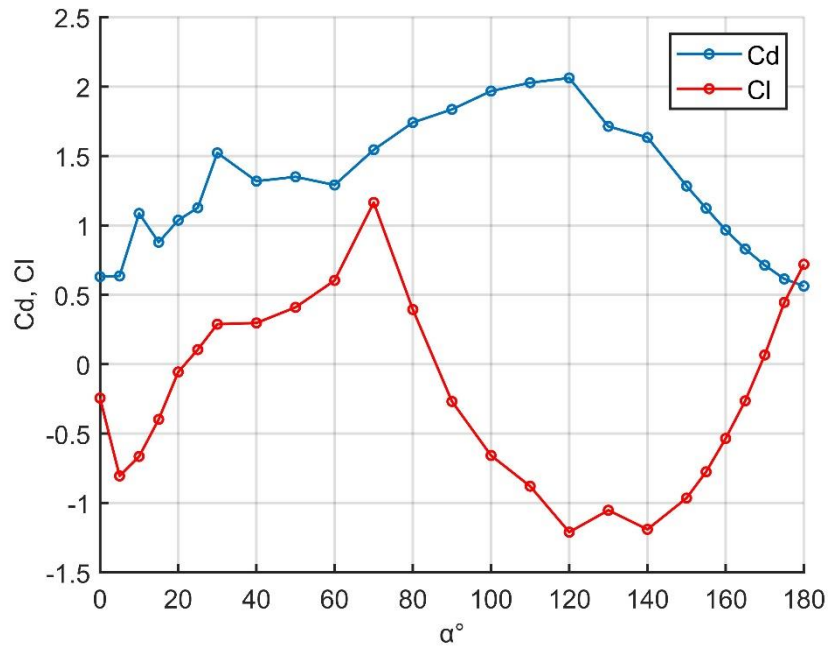
The Den Hartog's coefficient is shown in Figure 3.10 for the three tested profiles. From the figure, it can be observed that the effect of the negative slope resulted in a greater negative peak for the rime ice profile than for S1 and S2. The three profiles were found to have two different ranges where instabilities may occur. For rime ice the potential risk of instabilities is in the range of $\alpha = 21.2^\circ$ and 30.2° , and the second range between $\alpha = 174.6^\circ$ and 180° . For the S1 profile the instabilities may occur between $\alpha = 0^\circ$ and 7.5° and between 76.4° and 102.8° . Finally, for the S2 profile, the vulnerable ranges were found to be between 43.3° and 52.8° , and 148.5° and 180° , respectively.

All the identified ranges which fulfilled the first galloping condition, also fulfilled the second and third condition from Equation (3.13) and Equation (3.14). The critical velocities V_c at which galloping will cut off were found to be lower compared with the velocity of 10 m/s considered

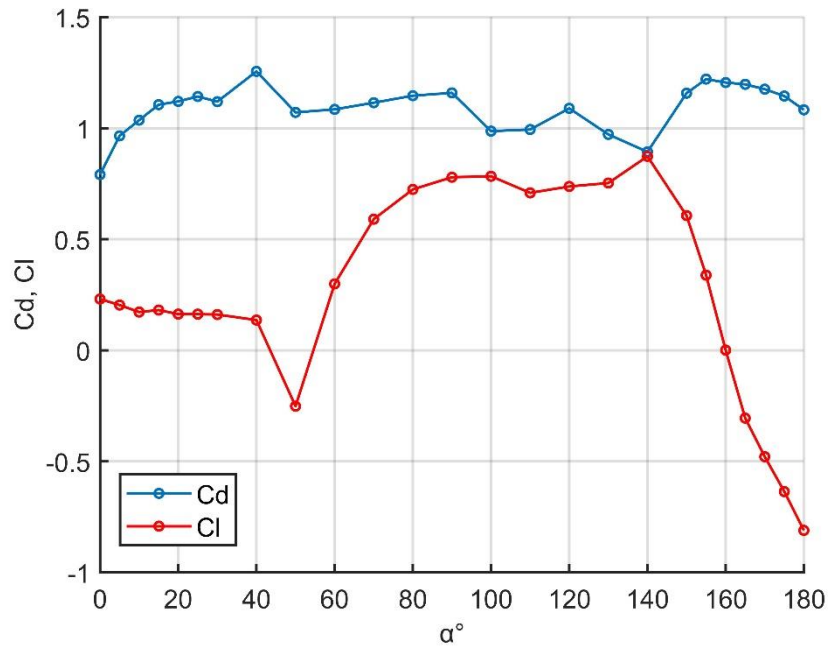
for this analysis. Table 3.3 shows V_c and ξa for the three profiles and both mode shapes. From the table, it can be concluded that galloping will occur at all the ranges previously discussed.



a) Rime profile



b) S1 profile



c) S2 profile

Figure 3.9. Aerodynamic lift and drag coefficients for the different profiles tested.

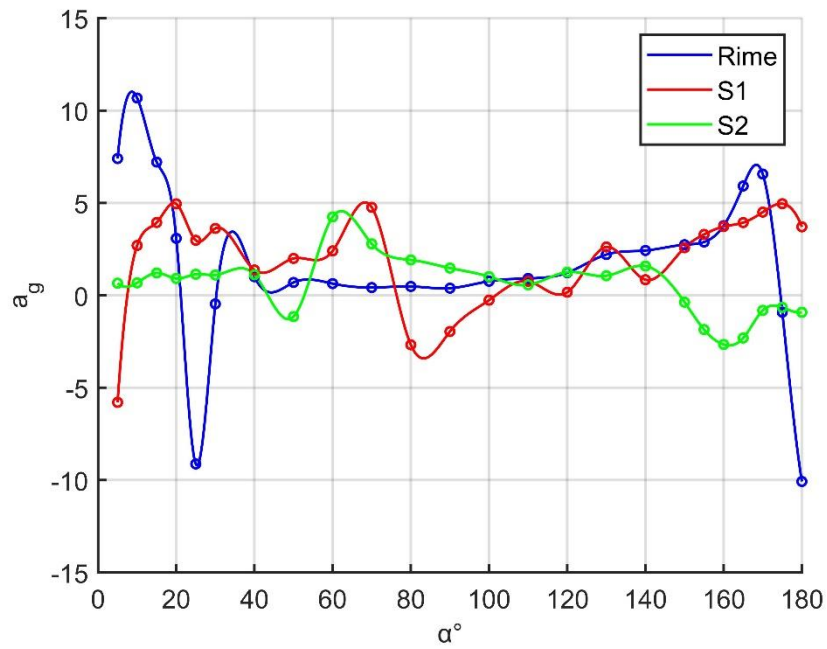


Figure 3.10. Den Hartog's coefficient vs angle of attack for the three different ice profiles.

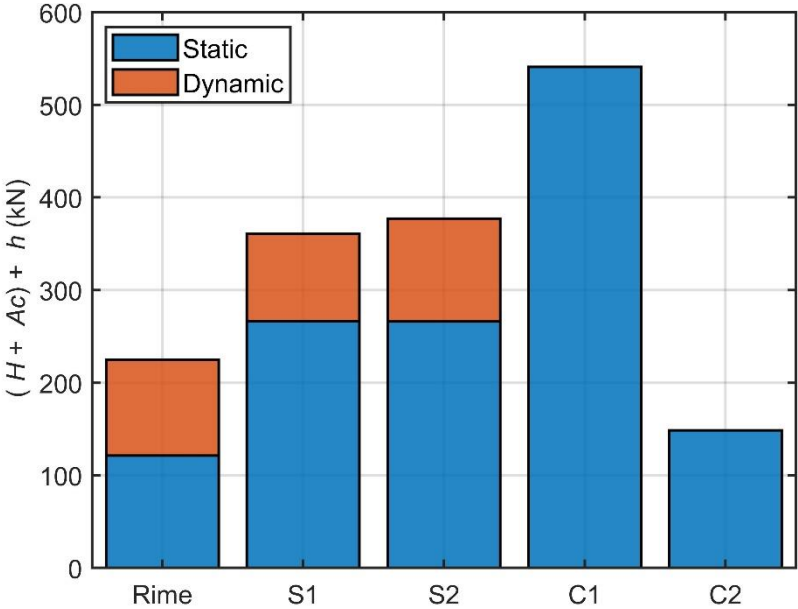
Table 3.3. Galloping conditions analysis.

Profile	$\Delta\alpha$	a_g	Vc (m/s)		ξa	
			φ_1	φ_2	φ_1	φ_2
Rime	21.2° – 30.2°	-9.17	0.89	1.20	-0.112	-0.082
	174.6° – 180°	-10.04	0.81	1.10	-0.122	-0.090
S1	0° – 7.5°	-5.79	1.41	1.91	-0.070	-0.052
	76.4° – 102.8°	-3.41	2.39	3.24	-0.041	-0.030
S2	43.3° – 52.8°	-1.26	6.46	8.75	-0.015	-0.011
	148.5° – 180°	-2.66	3.07	4.16	-0.032	-0.024

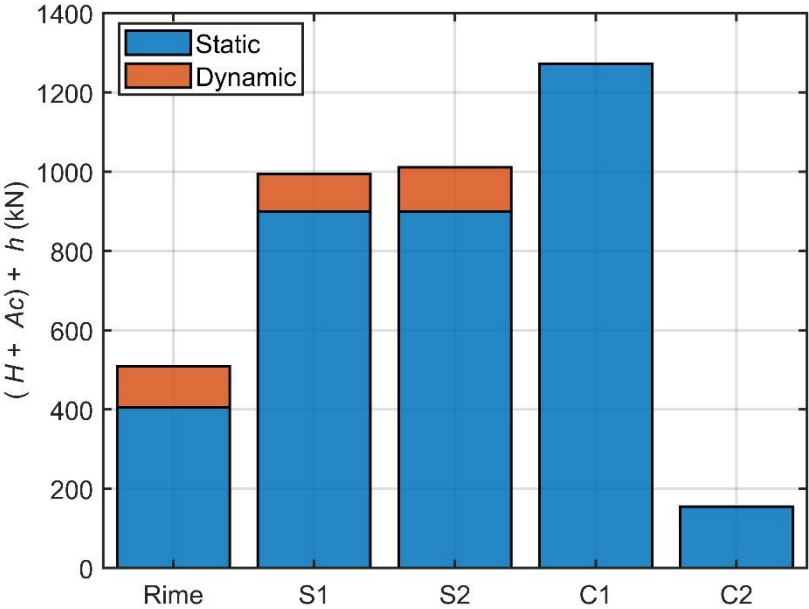
The tension transmitted to the towers for the three profiles produced by the static ($A_c + H$) (considering the radial ice accretion) and dynamic (h) loads are shown in Figure 3.11 and Table 3.4. The loads H calculated from the CSA-C22.3 standard procedure are shown in Table 3.5. For the ice load, a $\rho_i = 900 \text{ kg/m}^3$ is considered for both C1 and C2 combinations, as stated in the standard.

From Figure 3.11, it can be observed that the contribution of the static load to the total load is greater for all the profiles tested, specially for the 150 (Figure 3.11b) and 500 years (Figure 3.11c). reliability levels. This is due to the increase in the data pairs magnitude considered for the static loads when increasing the reliability level, while for the dynamic effects the ice profile remains the same and thus the dynamic load is not increasing as function of the reliability level. Both S1 and S2 profiles registered considerably higher magnitudes than for the rime profile due to the ice density characteristic of glaze ice. The C1 combination was found to cover the static loads and dynamic effects for all the reliability levels. In average, considering all the reliability levels, the C2 combination tends to overestimate the rime ice, and glaze profiles S1 and S2 by a factor of 2.61, 1.39, and 1.35, respectively. The contrary was found for C2, which seriously underestimated the loading for all cases. For this reason, it can be concluded that for this specific case, the ice load is

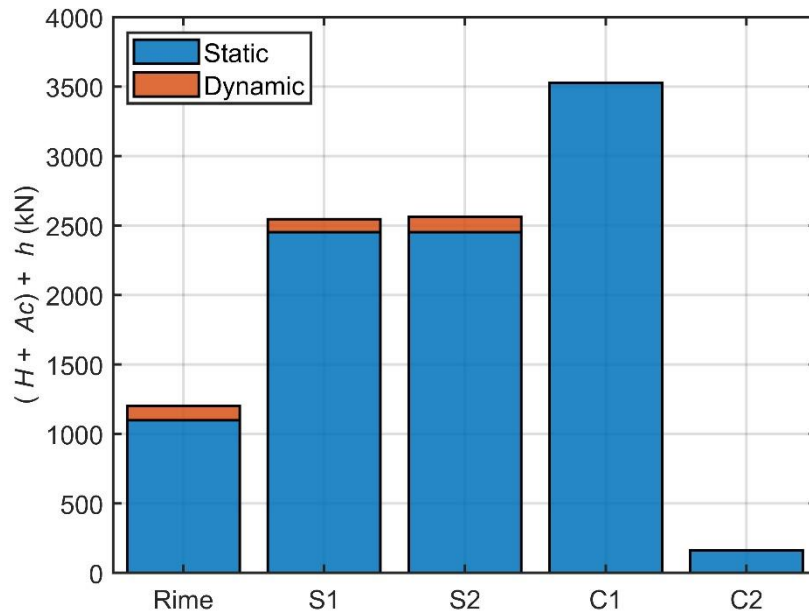
dominant, and C1, which is related to the low probability R_{eq} is a better option to cover the static and dynamic effects produced at the onset of galloping.



a) 50 MRI



b) 150 MRI



c) 500 MRI

Figure 3.11. Static and dynamic loads for the three profiles tested and three reliability levels.

Table 3.4. Static and dynamic loads for the three profiles tested and three reliability levels.

	Reliability level			
	50	150	500	
Profile	$H + A_c$ (kN)	$H + A_c$ (kN)	$H + A_c$ (kN)	h (kN)
Rime	121.40	405.25	1098.48	103.42
S1	266.21	899.64	2451.97	94.25
S2	266.21	899.64	2451.97	111.04

Table 3.5. Static loads calculated from the standard (CSA-C22.3) procedure.

	Reliability level		
	50	150	500
Combination	$H + A_c$ (kN)	$H + A_c$ (kN)	$H + A_c$ (kN)
C1	541.00	1271.83	3527.00
C2	148.49	154.84	162.13

3.5 Conclusions

Stability analysis for three different ice profiles have been carried out. The three profiles were found to be susceptible to vertical galloping within two different ranges of angle of attack. Rime ice presented potential risk of instabilities in the range of $\alpha = 21.2^\circ$ and 30.2° , and the second range between $\alpha = 174.6^\circ$ and 180° . For the S1 profile these ranges resulted within $\alpha = 0^\circ$ and 7.5° and between 76.4° and 102.8° . The S2 profile presented risk of instabilities between 43.3° and 52.8° , and 148.5° and 180° . The analysis revealed that the complex ice profile S2 transmitted greater tension to the towers, followed by the Rime profile and S1 profile, in that order. However, in all the cases, the extra tension produced on the onset of galloping was found to be small compare with the static load calculated from the hazard contours, except for the rime ice profile for the first level of reliability, for which dynamic effects represented 46% of the total tension. The combination C1 from the CSA-C22.3 standard have been found to always cover the static and dynamic wind effects on the iced conductors. In average, the C1 combination was 2.61, 1.39, and 1.35 times greater than the wind and ice loading for the Rime, S1, and S2 profiles, respectively. The C2 combination was found to be inaccurate for this specific site of study since it drastically underestimated the tension for all the profiles and all the reliability levels.

3.6 References

- Borna, A. (2014). *Prediction of Galloping of Transmission Line Conductors by a Computational Aeroelastic Approach* [Monograph]. McGill University.
- Borna, A., Habashi, W. G., & McClure, G. (2012). *Numerical Study of Influence of Ice Location on Galloping of an Iced Conductor*. 123–132.
- Den Hartog, J. P. (1932). Transmission Line Vibration Due to Sleet. *Transactions of the American Institute of Electrical Engineers*, 51(4), 1074–1076. <https://doi.org/10.1109/T-AIEE.1932.5056223>
- El-Fashny, K. (2002). *Modeling ice loads using passive ice meter observations in Quebec*. McGill University.
- Farzaneh, M. (Ed.). (2008). *Atmospheric icing of power networks*. Springer.
- Fu, P. (2004). *Modelling and simulation of the ice accretion process on fixed or rotating cylindrical objects by the boundary element method* [Université du Québec à Chicoutimi]. <https://doi.org/10.1522/18326611>
- Fu, P., Farzaneh, M., & Bouchard, G. (2006). Two-dimensional modelling of the ice accretion process on transmission line wires and conductors. *Cold Regions Science and Technology*, 46(2), 132–146. <https://doi.org/10.1016/j.coldregions.2006.06.004>
- Gjelstrup, H., & Georgakis, C. T. (2011). A quasi-steady 3 degree-of-freedom model for the determination of the onset of bluff body galloping instability. *Journal of Fluids and Structures*, 27(7), 1021–1034. <https://doi.org/10.1016/j.jfluidstructs.2011.04.006>
- Guerard, S., Godard, B., & Lilien, J.-L. (2011). Aeolian Vibrations on Power-Line Conductors, Evaluation of Actual Self Damping. *IEEE Transactions on Power Delivery*, 26(4), 2118–2122. <https://doi.org/10.1109/TPWRD.2011.2151211>

- Irvine, H. M., & Caughey, T. K. (1974). The linear theory of free vibrations of a suspended cable. *Proc. R. Soc. Lond. A.*, *341*, 299–315.
- Lilien, J.-L., Van Dyke, P., Asselin, J.-M., Farzaneh, M., Halsan, K., Havard, D., Hearnshaw, D., Laneville, A., Mito, M., Rawlins, C. B., St-Louis, M., Sunkle, D., & Vinogradov, A. (2005). *State of the art of conductor galloping*. Task Force B2.11.06.
- Liu, Y., Tang, A. P., Liu, K. T., & Tu, J. W. (2015). Numerical simulation on the aerodynamic force of the iced conductor for different angles of attack. *Engineering Review*, *35*(2), 157–169.
- Macdonald, J. H. G., & Larose, G. L. (2008). Two-degree-of-freedom inclined cable galloping—Part 1: General formulation and solution for perfectly tuned system. *Journal of Wind Engineering and Industrial Aerodynamics*, *96*(3), 291–307. <https://doi.org/10.1016/j.jweia.2007.07.002>
- Makkonen, L. (2000). Models for the growth of rime, glaze, icicles and wet snow on structures. *Philosophical Transactions of the Royal Society of London. Series A: Mathematical, Physical and Engineering Sciences*, *358*(1776), 2913–2939. <https://doi.org/10.1098/rsta.2000.0690>
- McComber, P., & Touzot, G. (1981). Calculation of the Impingement of Cloud Droplets in a Cylinder by the Finite-Element Method. *American Meteorological Society*, *38*, 1027–1036.
- National Standard of Canada, (2010). *Design criteria of overhead transmission lines* (CAN/CSA-C22.3). Ontario, Canada
- Pohlman, J., & Landers, P. (1982). Present State-of-the-Art of Transmission Line Icing. *IEEE Transactions on Power Apparatus and Systems*, *PAS-101*(8), 2443–2450. <https://doi.org/10.1109/TPAS.1982.317605>
- Poots, G., & Skelton, P. L. I. (1995). Simulation of wet-snow accretion by axial growth on a transmission line conductor. *Applied Mathematical Modelling*, *19*(9), 514–518. [https://doi.org/10.1016/0307-904X\(95\)00012-9](https://doi.org/10.1016/0307-904X(95)00012-9)

- Rossi, A. (2018). *Wind tunnel modelling of snow and ice effects on transmission lines*. Technical University of Denmark.
- Rossi, A., Jubayer, C., Koss, H., Arriaga, D., & Hangan, H. (2020). Combined effects of wind and atmospheric icing on overhead transmission lines. *Journal of Wind Engineering and Industrial Aerodynamics*, 204, 104271. <https://doi.org/10.1016/j.jweia.2020.104271>
- Scruton, C., & Flint, A. R. (1964). Wind-excited oscillations of structures. *Proceedings of the Institution of Civil Engineers*, 27(4), 673–702. <https://doi.org/10.1680/iicep.1964.10179>
- Sijal, A. (2019). *Understanding Y+ for CFD Simulations*. <https://www.linkedin.com/pulse/understanding-y-cfd-simulation-sijal-ahmed>
- Wang, X., & Lou, W.-J. (2009). *Numerical Approach to galloping of Conductor*. The Seventh Asia-Pacific Conference on Wind Engineering. Taipei, Taiwan

Chapter 4

4 Conclusions and future work

This thesis presented ice accretion analysis for mountainous terrain divided into two parts. First, the wind and ice acting jointly on the transmission line system have been probabilistically characterized. The approach uses probability distributions to build joint hazard contours to select data pairs of wind speed and ice accretion occurring simultaneously during an icing event. Second, the dynamic effects of the wind speed on the iced conductors is performed. The ice profiles are selected based on similarity between the present work and previous studies regarding the weather characteristics at the site of study. Comparisons between the outcome of this analysis and the wind and ice loads proposed by the Canadian standard CSA-C22.3 are presented.

4.1 Summary

Chapter 2 presents the weather characteristics at the site of study. 16 weather stations are used for the estimation of hourly temperature, precipitation, and wind speed. IDW interpolations are performed taking into consideration the 16 surrounding weather stations. The KNNI algorithm is used for precipitation rate estimation. Station 12 and the site of interest are assumed part of the same basin and station 12 is completed using the most correlated neighbor stations (stations 7 and 9). An ANN is used for wind speed prediction. The 7 weather stations with complete records (2005 - 2015) and the WRF model velocities from Agustsson & Nygaard, (2016) are used to train-test the model. A total of 30 predictors including the wind speed, wind direction, atmospheric pressure, and temperature from the seven complete weather stations, in addition to the hour of the day and month of the year are used to feed the network. The ice accretion model from Makkonen, (2000) is performed for a radial ice accretion estimation. The ice load is selected based on the maximum ice accretion registered for each icing event, and the wind on ice load is

selected by choosing the maximum velocity presented during the evolution of each storm. The ice accretion and wind speed are fitted to their correspondent probability distributions and 500 years of icing events are simulated based on these distributions. The wind and ice joint histogram is built with the data pairs considering both, historical and simulated events, and the joint probability of exceedance (JCDF) curve is built with the product of the marginal cumulative density functions of ice accretion and wind speed. Joint hazard contours are drawn by projecting the JCCDF curve in the x-y plane for a given probability of exceedance, which indicate the data pairs occurring simultaneously for a given reliability level.

Chapter 3 presents the ice profiles considered for the dynamic analysis. For the rime ice profile, the well accepted crescent shape by axial growth described in Poots & Skelton, (1995) is considered. The glaze ice profiles are selected based on similarity between the weather characteristics at the site of study from Chapter 2, and the characteristics used in Fu et al., (2006) for a two-dimensional modelling of ice accretion. CFD simulations are carried out to obtain aerodynamic lift and drag coefficients for a given angle of attack, and 25 data points are obtained to build the lift and drag curve for each profile. The Den Hartog's criterion is applied for the identification of potential aerodynamic instabilities, and the critical velocity and aerodynamic damping ratio are calculated to assume galloping to fully develop if the three galloping conditions are fulfilled.

4.2 Conclusions

The overall conclusions from Chapter 2 are the following:

- Temperature data from the IDW interpolations were in good agreement with the WRF model, achieving a correlation coefficient of 0.92. The low control parameter $\alpha_i = 1.5$ revealed the stronger influence of the stations closer to the site of interest. IDW is an adequate method to estimate temperature records at mountainous terrain using the linear relationship with respect to height and using the Lapse rate to detrend the records.

- The wind speeds predicted by the ANN were found to underestimate the peak values above the 99 percentile from the WRF model wind speeds. This is reflected in the estimation of the 50-year return period velocity, where a difference of 12% between them were found. However, an overall good fit below the 99 percentile were obtained and a correlation coefficient of 0.81 was achieved.
- The wind speed values from the network were also found in good agreement with a mixed numerical and experimental simulation of the same site topography by Jubayer & Hangan, (2018), where differences between the design wind velocity and wind gust for the same site of study were found to be 4% and 6%, respectively.
- The results from the ice accretion model resulted in a total of 385 icing events within the 15-year period, for an average of 25.67 storms per year. A total of 38 storms were categorized as extreme events, for an extreme recurrence rate of 2.53 per year.
- The data pairs considered in the standard CSA-C22.3 for the design of wind and ice loading for overhead transmission lines were found to be conservative. The reliability level for a 50-year return period was found to be a combination of data pairs belonging to the 0.2%, 500-year hazard contour. The rest of the combinations were found to be far more conservative compared to all the predicted hazard contours.

The overall conclusions from Chapter 3 are the following:

- The CFD simulations for the rime ice profile underpredicted the peak values of the Cl curve from the wind tunnel experiments reported in Rossi et al., (2020). Differences of 17% for the angle of attack $\alpha = 20^\circ$, and 24% for the second local peak at $\alpha = 170^\circ$ were found.

- There were two ranges of angle of attack with potential risk of instabilities for all the profiles tested. The Den Hartog's coefficient were found negative at $\alpha = 21.2^\circ - 30.2^\circ$, and between $\alpha = 174.6^\circ - 180^\circ$, with a negative peak value of $a_g = -9.71$ and $a_g = -10.14$, respectively, for the rime ice profile.
- For the S1 profile, the ranges of potential instabilities resulted within $\alpha = 0^\circ$ and 7.5° and between 76.4° and 102.8° , with $a_g = -5.79$ and $a_g = -3.41$, respectively. In the case of the S2 profile, the ranges were 43.3° and 52.8° , and 148.5° and 180° , with $a_g = -1.26$ and $a_g = -2.66$.
- For all the ranges identified with a negative a_g , the second and third condition of galloping related to $u > V_c$, and $\xi s + \xi a < 0$ were also fulfilled.
- The C1 combination proposed by the standard were found to cover the sum of the static effects considering a radial ice deposit and the dynamic effects considering the complex shapes for all the profiles, rime, glaze S1, and glaze S2, and for all the reliability levels. In average, the C1 combination were found to overpredict the total load by a factor of 2.61, 1.39, and 1.35 for the rime, S1, and S2 profiles, respectively. In addition, the dynamic effects for a free stream velocity of $u = 10$ m/s were found to be small compared with the static load effects calculated from the hazard contours, except for the rime ice profile in the 50-year reliability level, where the dynamic effects represented 46% of the total load.
- The C2 combination unpredicted the static and dynamic effects for all the profiles and reliability levels tested. The t -year return period ice load, related to the C1 combination, increases a lot compare to the t -year return period wind speed, related to C2. The ice accretion data pair for a 50, 150, and 500-year reliability level corresponds to $R_{eq} = 12.52, 19.65, \text{ and } 33.27$ cm. Assuming $p_i = 900$ kg/m³ recommended in the standard, the ice load resulted in 476, 1173, and 3364 kN, respectively. This corresponds to an increasing factor of 2.46 from the 50-year to the 150-year reliability level, and 2.86 from

the 150-year to the 500-year reliability level. The wind speed data dominant pair, on the other hand, is not increasing as much as the ice dominant data pair. The wind speed values are 36.71, 39, and 41.47 m/s for the three reliability levels. These values resulted in 64, 98, and 162 kN. This corresponds to an increasing factor of 1.5 from the 50-year to the 150-year reliability level, and 1.65 from the 150-year to the 500-year reliability level. Furthermore, the contribution to the total tension of the ice load compare with the wind load is considerably greater. For this reason, C1 seems to be the accurate combination to take into consideration for the structural design of the system for the studied site of interest.

4.3 Future work

- Further analysis to improve the peak predictions of the wind speed values is recommended. This can be done using data sets from different sources than in the present thesis, including relative humidity as one of the inputs, as it has been observed to be a good predictor for this kind of analysis. Moreover, more weather stations with complete records are recommended to be used for training the network. In addition, other machine learning algorithms such as random forest, which has been applied in previous studies (Veronesi et al., 2016) for wind speed estimations can be performed and compared with the network performance.
- It is pertinent to mention that galloping produces oscillatory motions which may lead to failure for fatigue, and it seems worthy to conduct further research in this topic.
- Aerodynamic analysis for wind speeds greater than 10 m/s are also recommended to be tested to estimate the increasing rate of the dynamic tension as function of the free stream velocity. An aerodynamic analysis considering a bundle conductor is also recommended.

- Recommendations of more complex methods to estimate aerodynamic instabilities such as a finite element model to perform 2-way fluid-structure interaction using LES simulations are proposed. In this way, more detailed time-history analysis can lead to more complete conclusions of the wind and ice effects on the system.

4.4 References

Agustsson, H., & Nygaard, B. E. (2016). *Long Lake transmission line, British Columbia, Canada: Calculation of climatic loads* (KVT/HA/2016/R025; p. 20). Kjeller Vindteknikk.

Den Hartog, J. P. (1932). Transmission Line Vibration Due to Sleet. *Transactions of the American Institute of Electrical Engineers*, 51(4), 1074–1076. <https://doi.org/10.1109/T-AIEE.1932.5056223>

Fu, P., Farzaneh, M., & Bouchard, G. (2006). Two-dimensional modelling of the ice accretion process on transmission line wires and conductors. *Cold Regions Science and Technology*, 46(2), 132–146. <https://doi.org/10.1016/j.coldregions.2006.06.004>

Makkonen, L. (2000). Models for the growth of rime, glaze, icicles and wet snow on structures. *Philosophical Transactions of the Royal Society of London. Series A: Mathematical, Physical and Engineering Sciences*, 358(1776), 2913–2939. <https://doi.org/10.1098/rsta.2000.0690>

National Standard of Canada, (2010). *Design criteria of overhead transmission lines* (CAN/CSA-C22.3). Ontario, Canada

Poots, G., & Skelton, P. L. I. (1995). Simulation of wet-snow accretion by axial growth on a transmission line conductor. *Applied Mathematical Modelling*, 19(9), 514–518. [https://doi.org/10.1016/0307-904X\(95\)00012-9](https://doi.org/10.1016/0307-904X(95)00012-9)

Veronesi, F., Grassi, S., & Raubal, M. (2016). Statistical learning approach for wind resource assessment. *Renewable and Sustainable Energy Reviews*, 56, 836–850.
<https://doi.org/10.1016/j.rser.2015.11.099>

Appendices

Appendix A: Figures supporting the lapse rate and the most intense icing events from Chapter 2

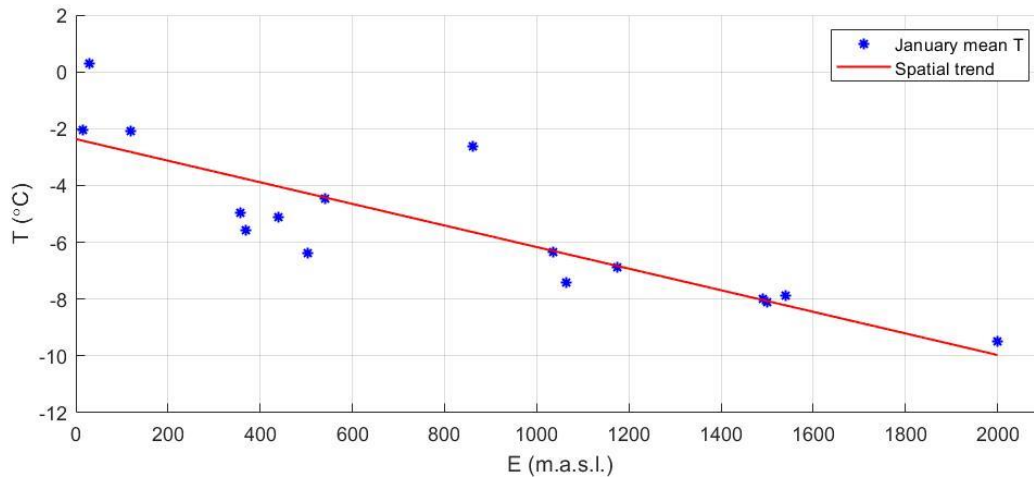


Figure A 1. Spatial trend and weather stations (blue dots) for the month of January ($L = 0.38\text{ }^{\circ}\text{C}/100\text{m}$), $r^2 = 0.73$.

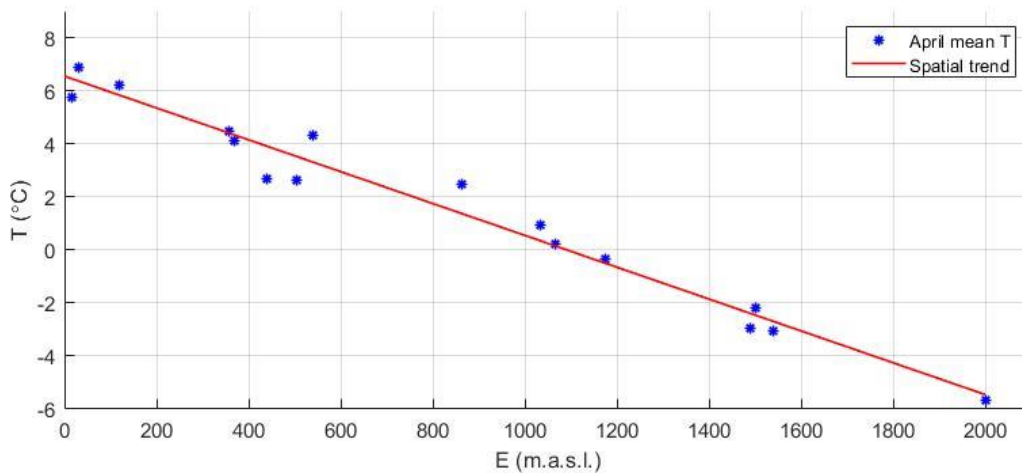


Figure A 2. Spatial trend and weather stations (blue dots) for the month of April ($L = 0.6\text{ }^{\circ}\text{C}/100\text{m}$), $r^2 = 0.97$.

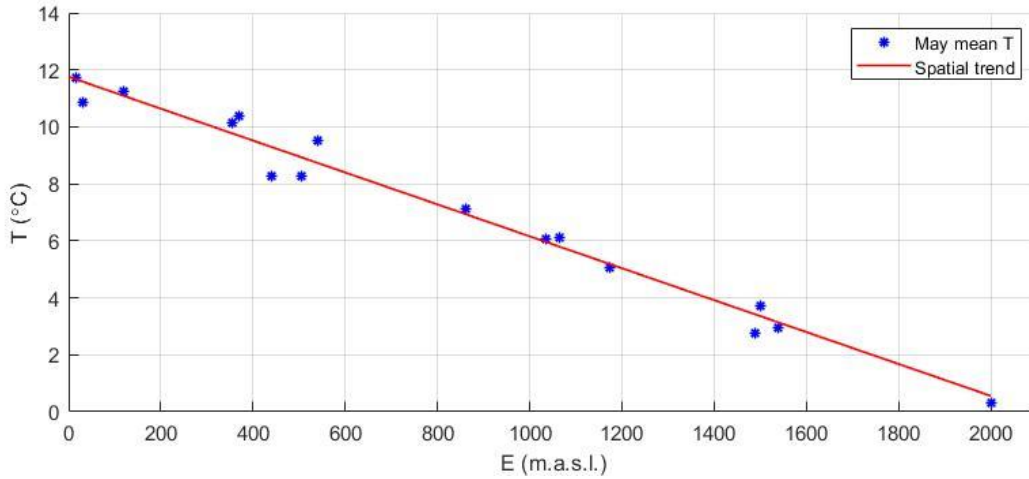


Figure A 3. Spatial trend and weather stations (blue dots) for the month of May ($L = 0.56 \text{ }^\circ\text{C}/100\text{m}$), $r^2 = 0.98$.

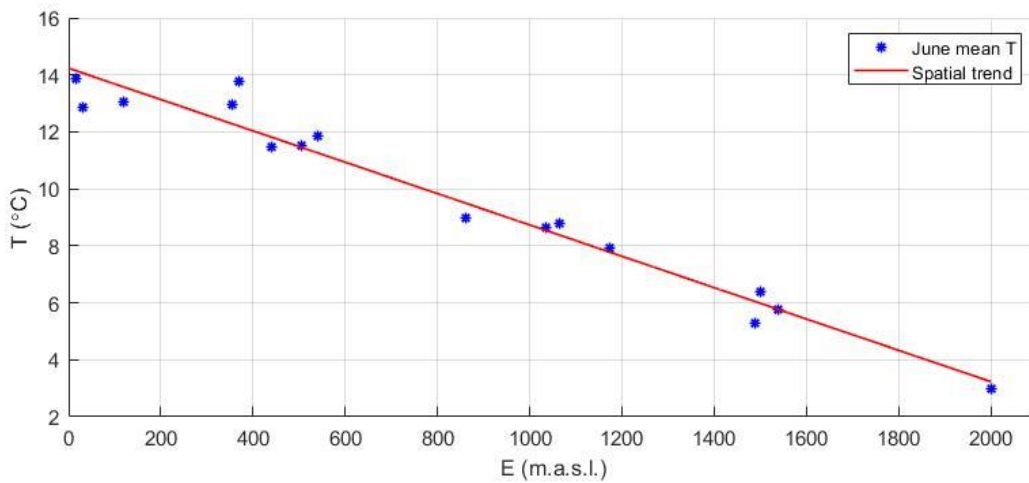


Figure A 4. Spatial trend and weather stations (blue dots) for the month of June ($L = 0.55 \text{ }^\circ\text{C}/100\text{m}$), $r^2 = 0.96$.

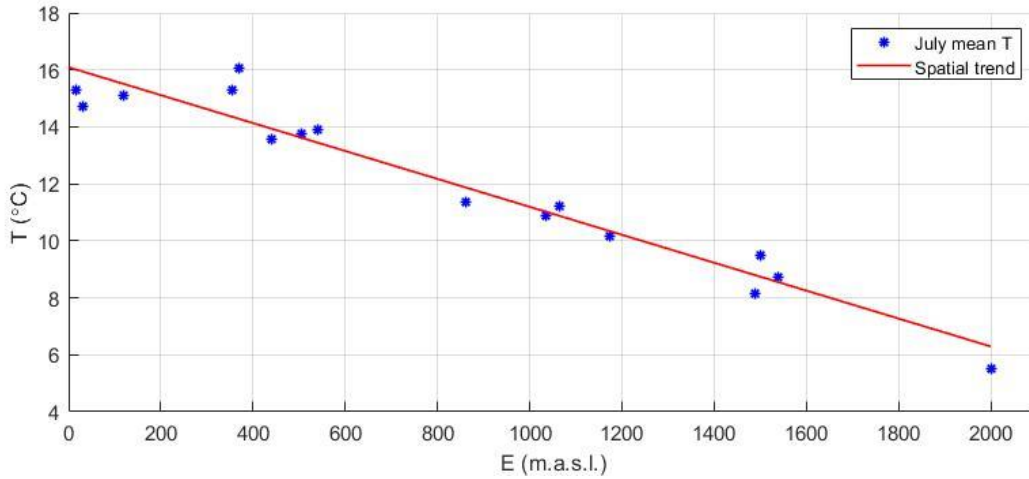


Figure A 5. Spatial trend and weather stations (blue dots) for the month of July ($L = 0.49\text{ }^{\circ}\text{C}/100\text{m}$), $r^2 = 0.94$.

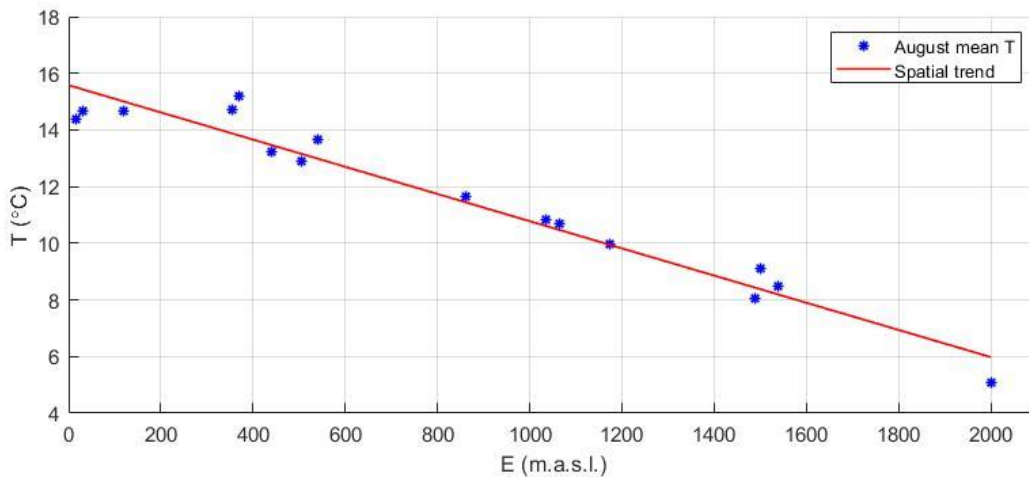


Figure A 6. Spatial trend and weather stations (blue dots) for the month of August ($L = 0.48\text{ }^{\circ}\text{C}/100\text{m}$), $r^2 = 0.95$.

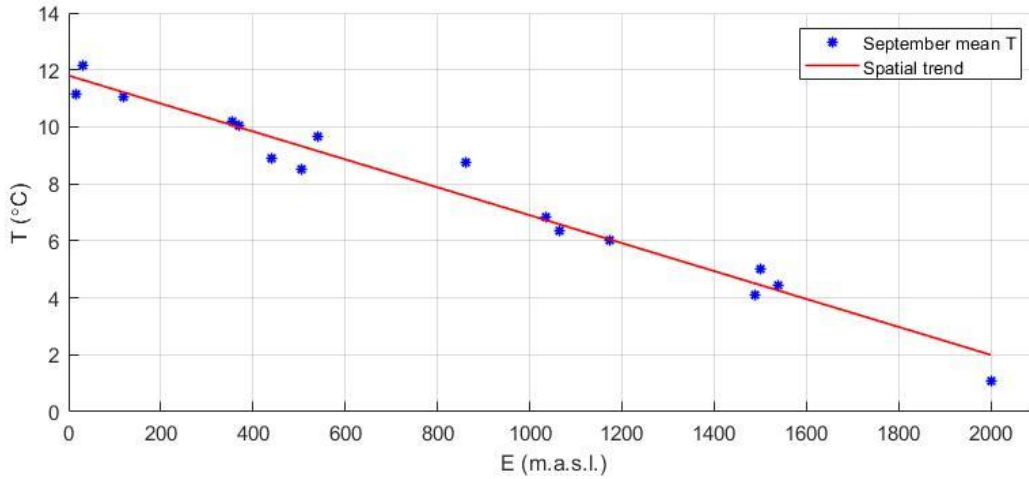


Figure A 7. Spatial trend and weather stations (blue dots) for the month of September ($L = 0.49\text{ }^{\circ}\text{C}/100\text{m}$), $r^2 = 0.97$.

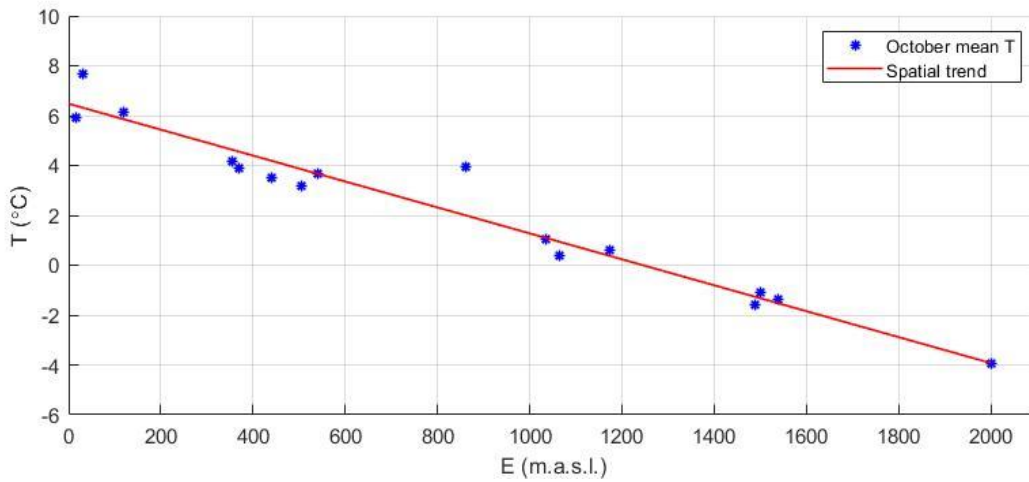


Figure A 8. Spatial trend and weather stations (blue dots) for the month of October ($L = 0.52\text{ }^{\circ}\text{C}/100\text{m}$), $r^2 = 0.95$.

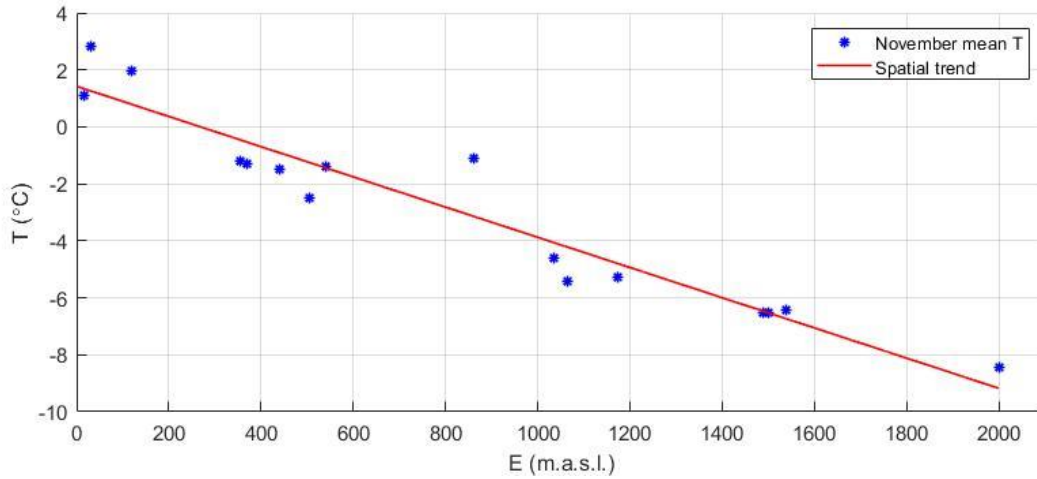


Figure A 9. Spatial trend and weather stations (blue dots) for the month of November ($L = 0.53 \text{ } ^\circ\text{C}/100\text{m}$), $r^2 = 0.92$.

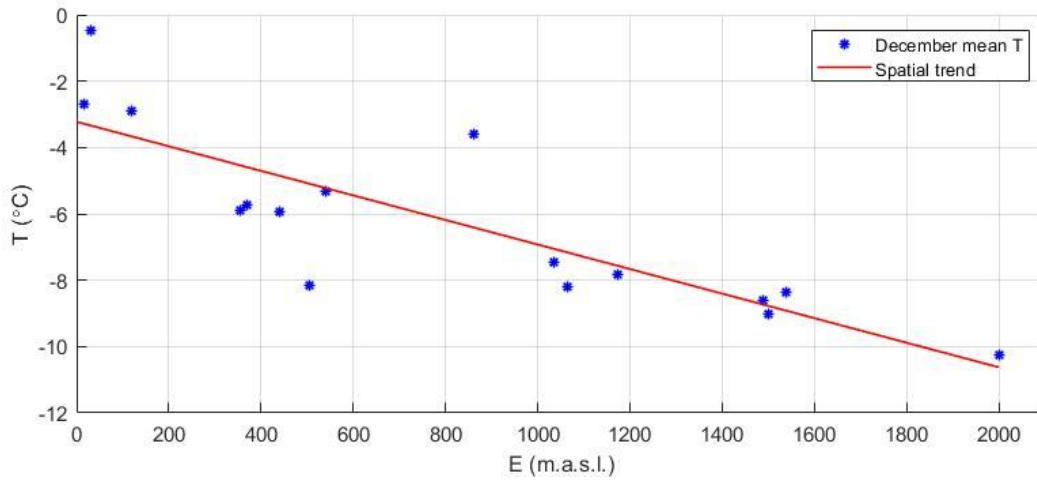
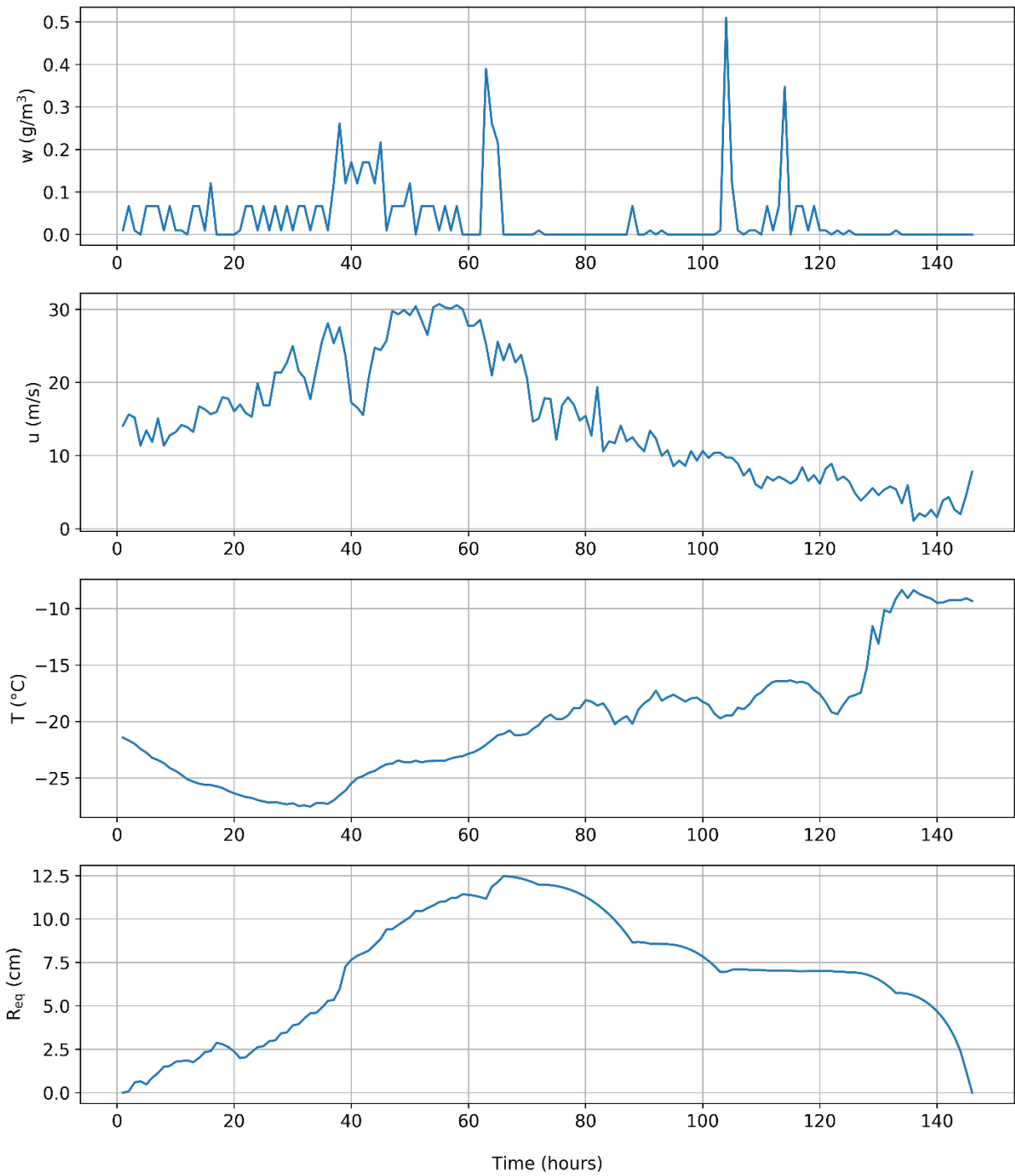
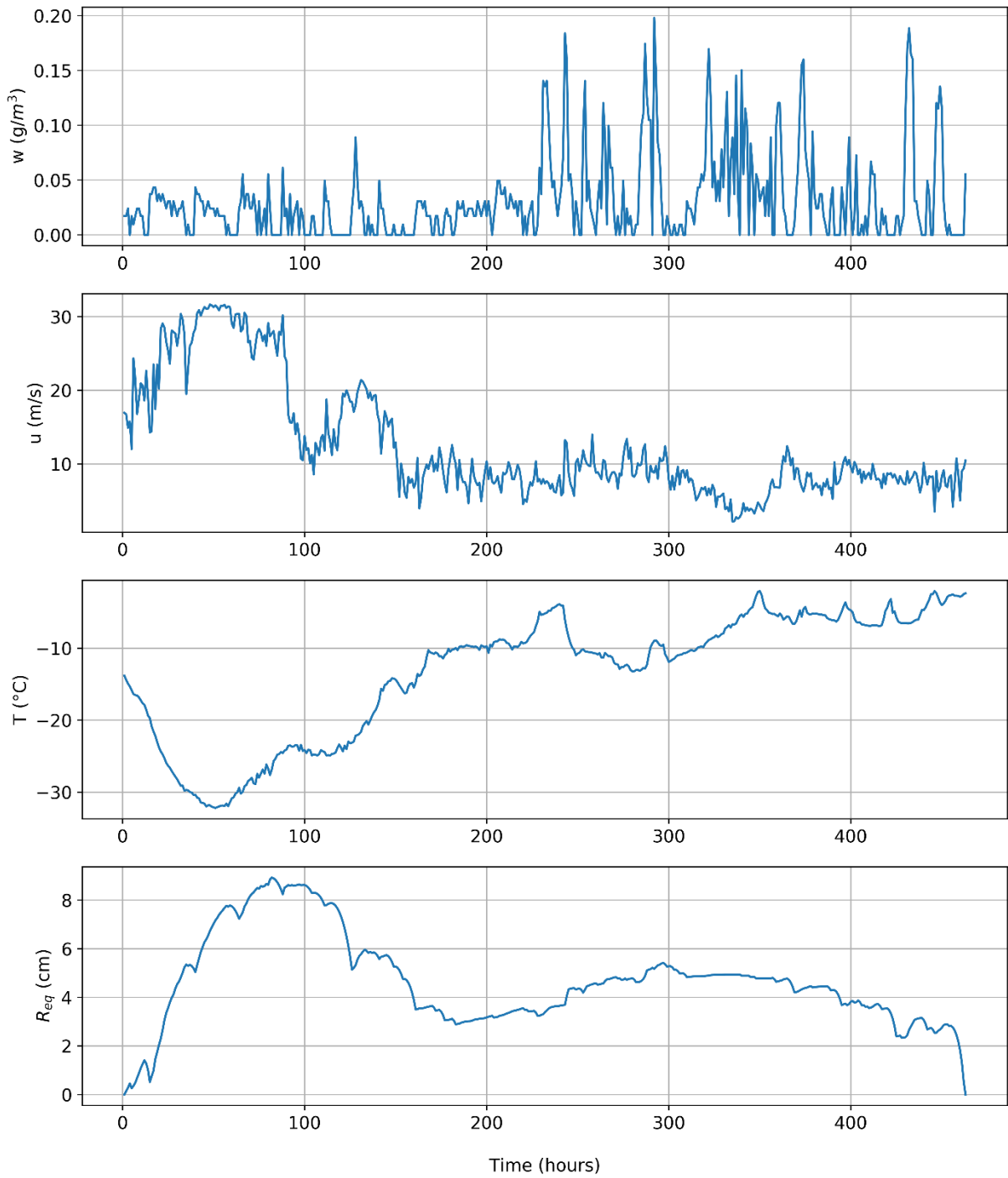


Figure A 10. Spatial trend and weather stations (blue dots) for the month of March ($L = 0.37 \text{ } ^\circ\text{C}/100\text{m}$), $r^2 = 0.71$.



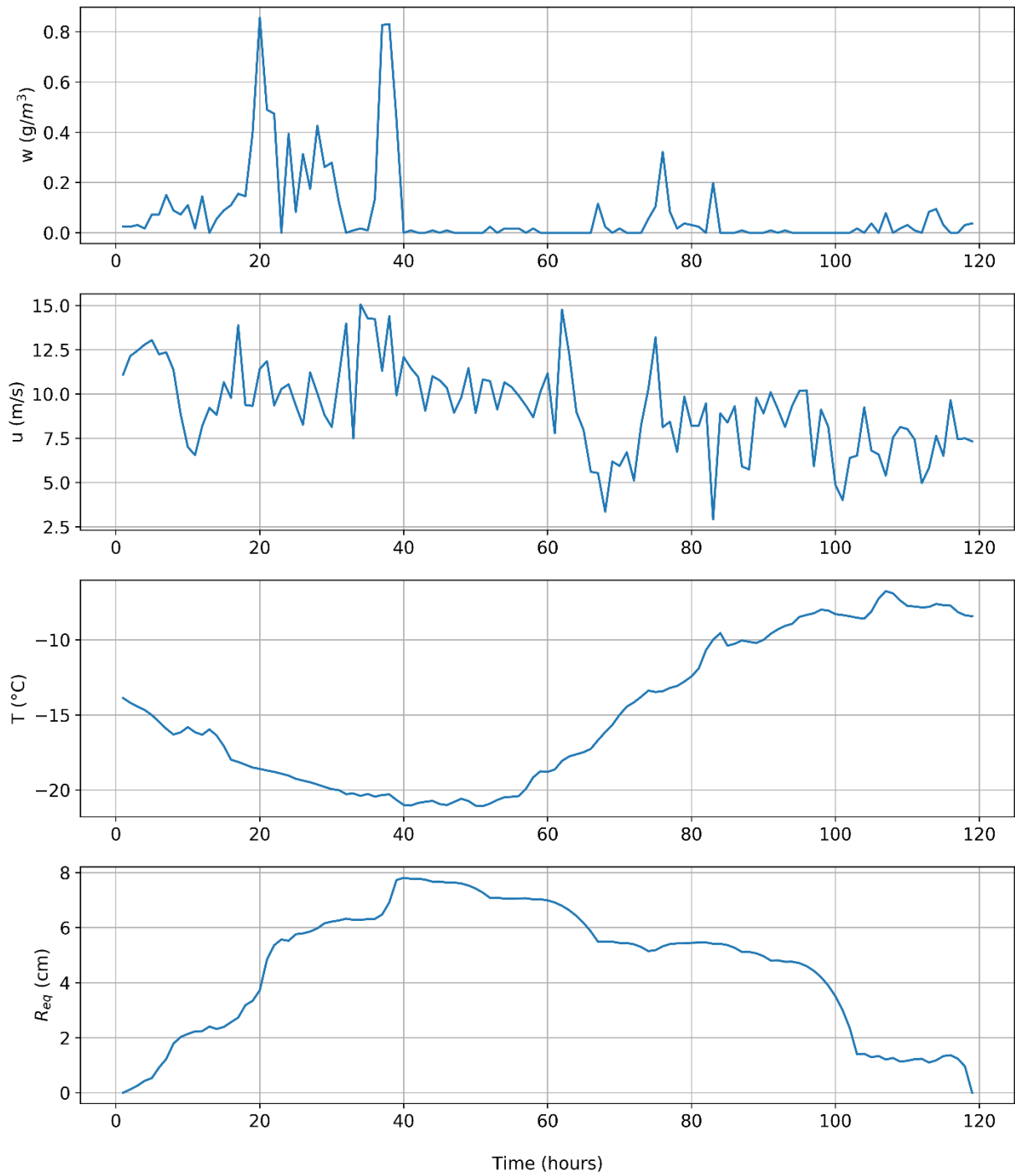
(From 2006-11-24 to 2006-11-30)

Figure A 11. Evolution of the first most intense icing event from Table 2.5. w) liquid water content, u) wind speed, T) temperature and R_{eq}) radial ice accretion.



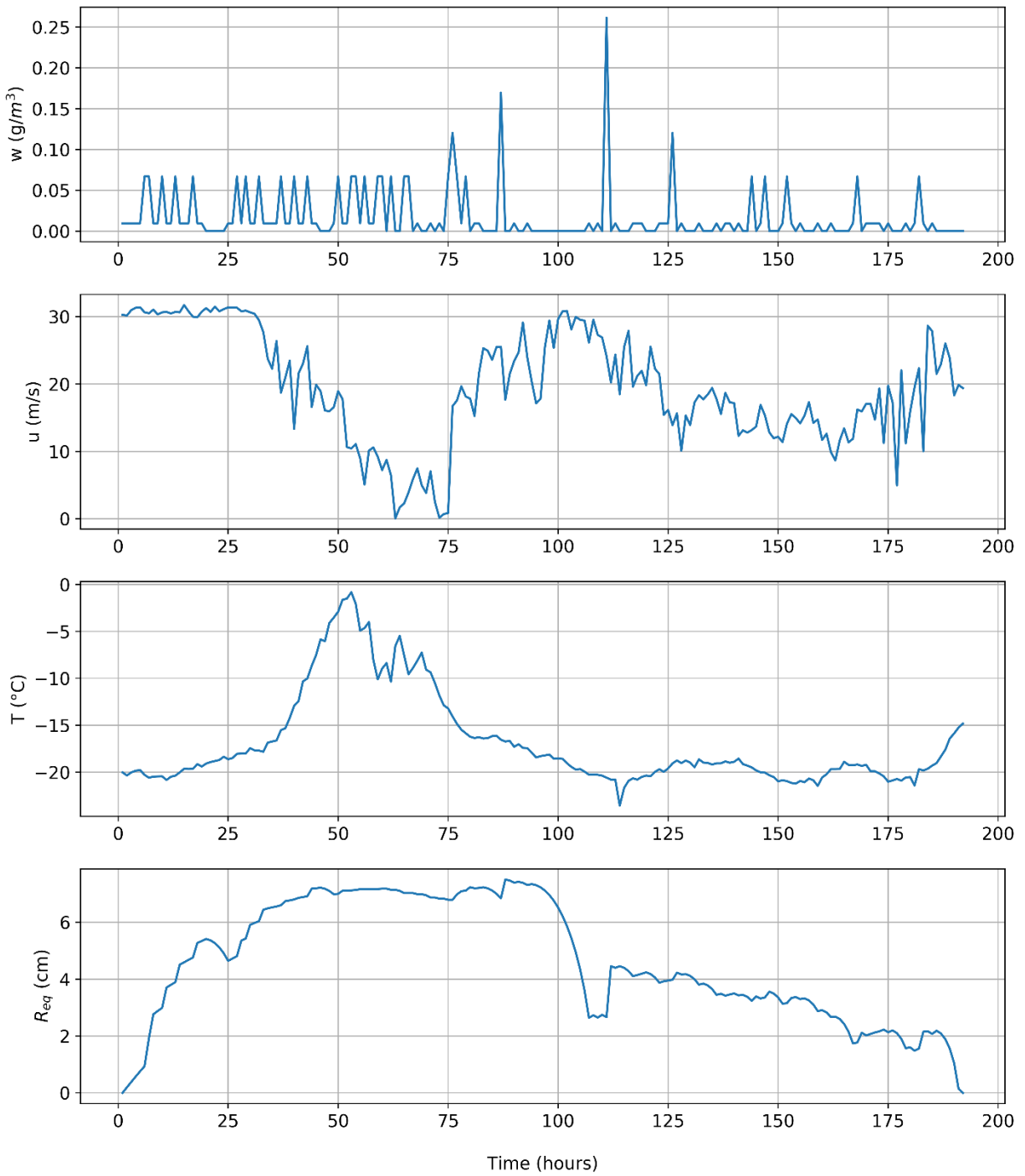
(From 2012-01-15 to 2012-02-03)

Figure A 12. Evolution of the second most intense icing event from Table 2.5. w) liquid water content, u) wind speed, T) temperature and R_{eq}) radial ice accretion.



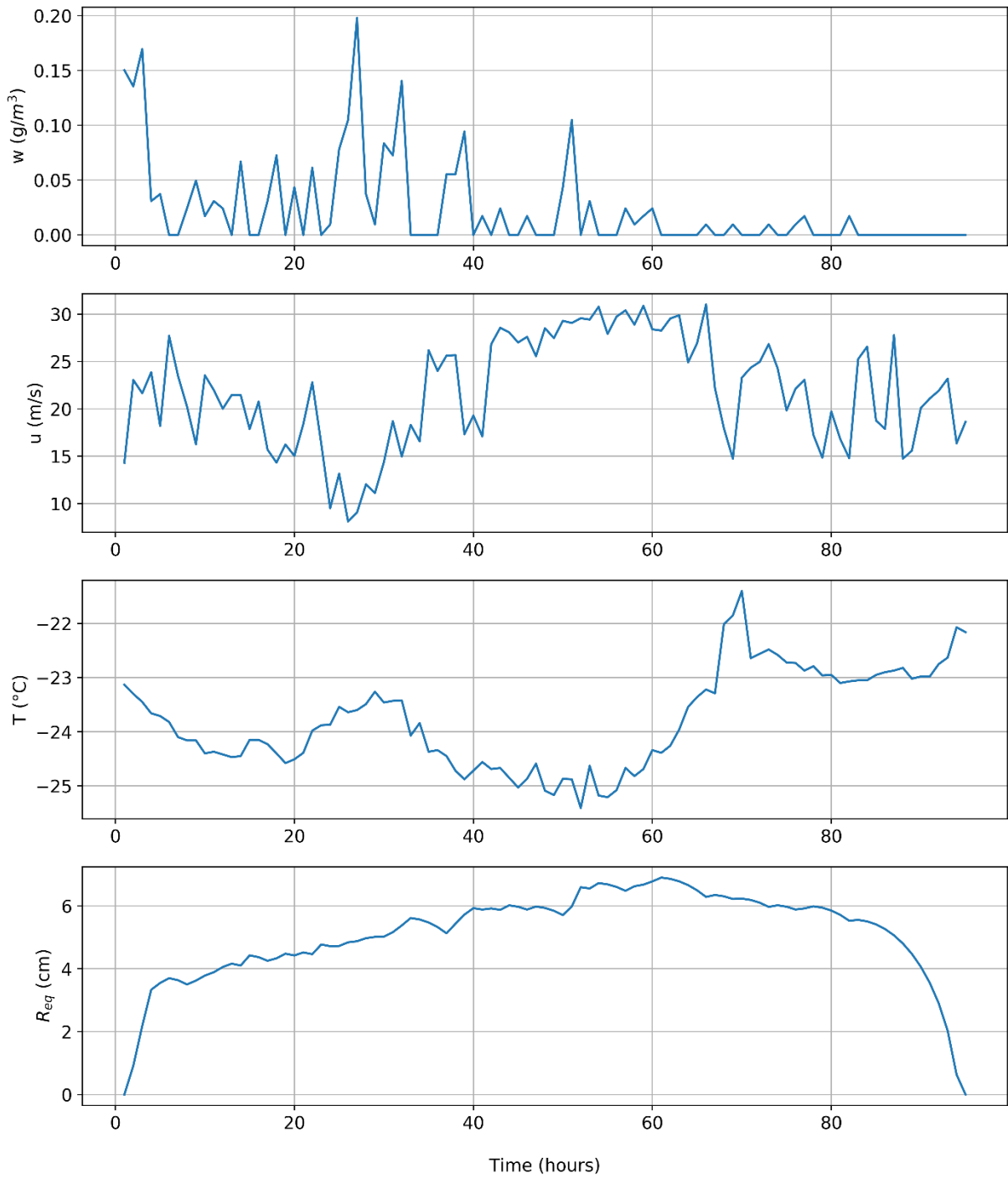
(From 2011-11-18 to 2011-11-23)

Figure A 13. Evolution of the third most intense icing event from Table 2.5. w) liquid water content, u) wind speed, T) temperature and R_{eq}) radial ice accretion.



(From 2008-12-13 to 2008-12-21)

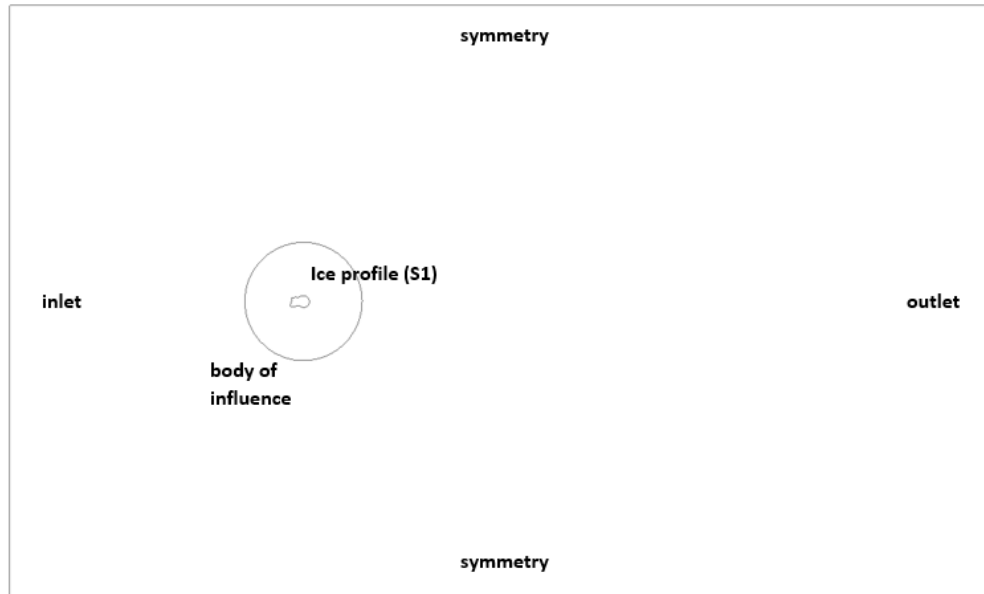
Figure A 14. Evolution of the fourth most intense icing event from Table 2.5. w) liquid water content, u) wind speed, T) temperature and R_{eq}) radial ice accretion.



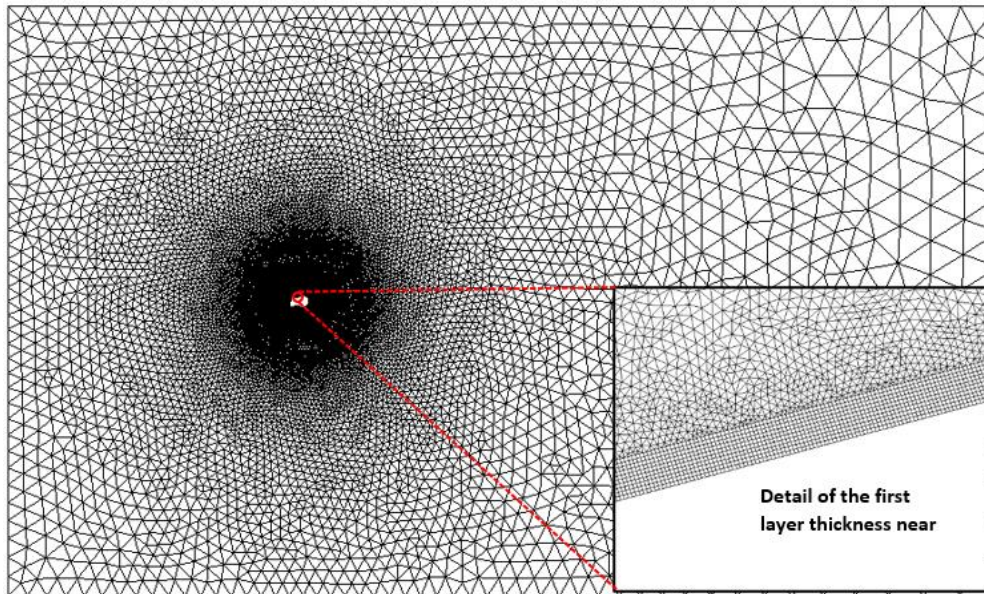
(From 2020-01-13 to 2020-01-17)

Figure A 15. Evolution of the fifth most intense icing event from Table 2.5. w) liquid water content, u) wind speed, T) temperature and R_{eq}) radial ice accretion.

Appendix B: Figures of the mesh and metrics for S1 and S2 profiles from Chapter 3

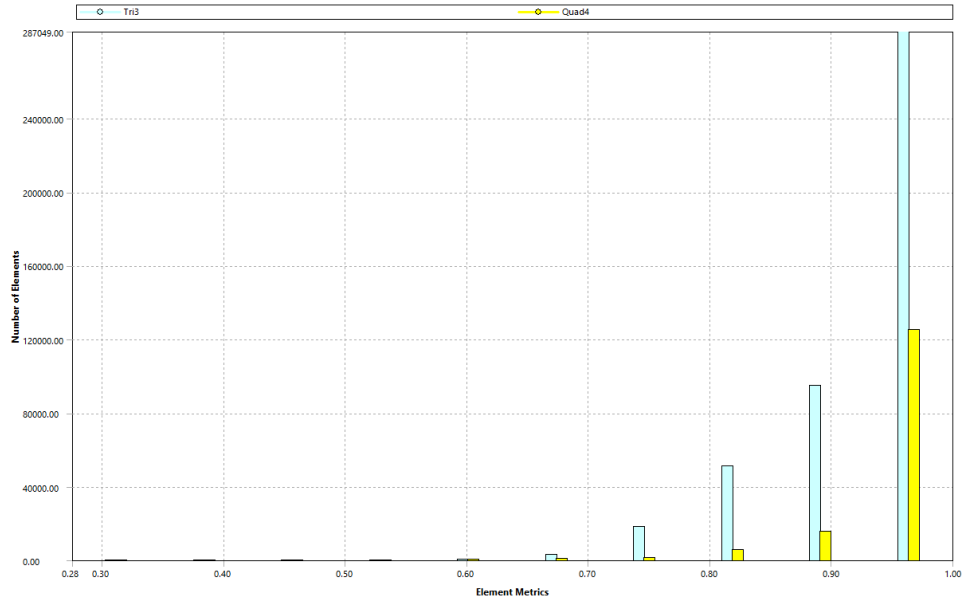


a)

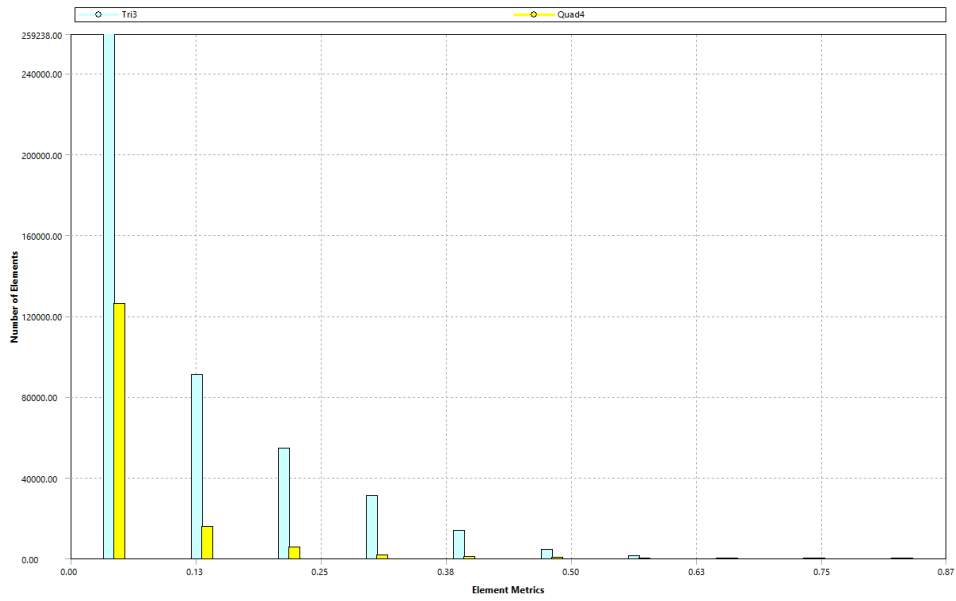


b)

Figure B 1. a) Boundary conditions and b) final mesh considered for the S1 profile with a total of $\approx 600,000$ elements, $y^+ = 10$, average element quality = 0.94, and average skewness = 0.09.

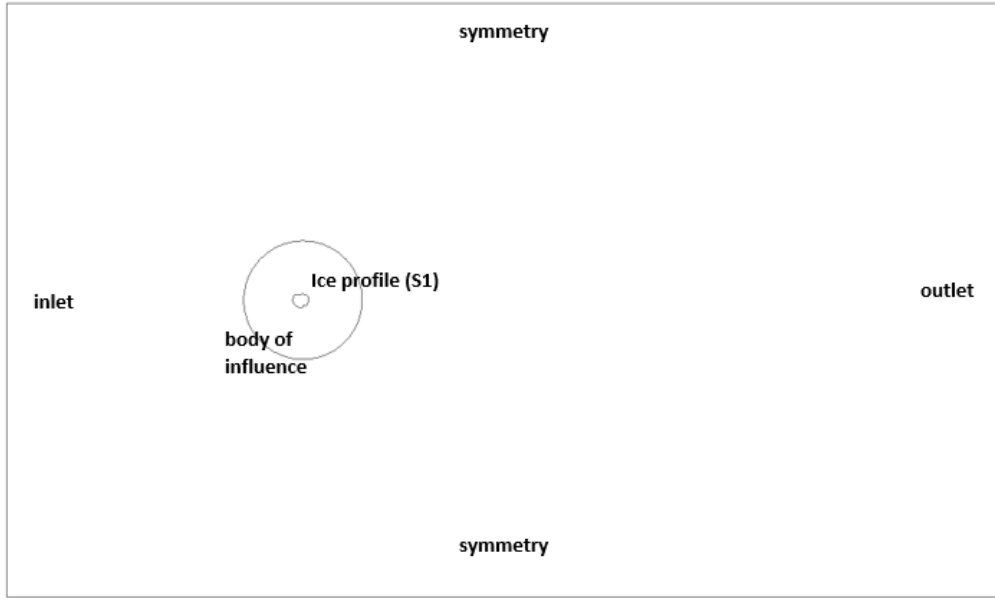


a)

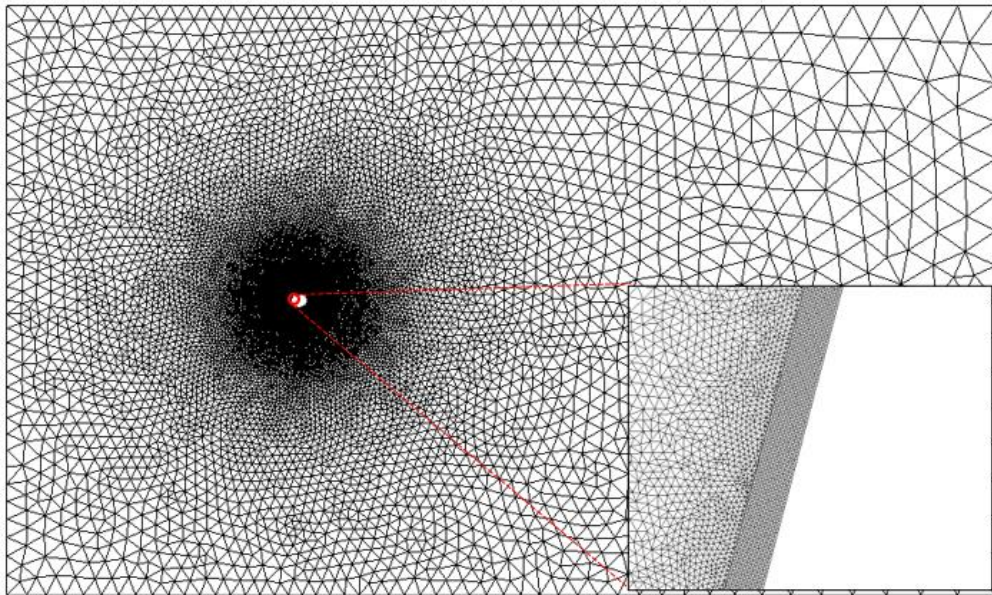


b)

Figure B 2 Mesh metrics for the rime S1 profile: a) Element Quality, and b) Cells Skewness.

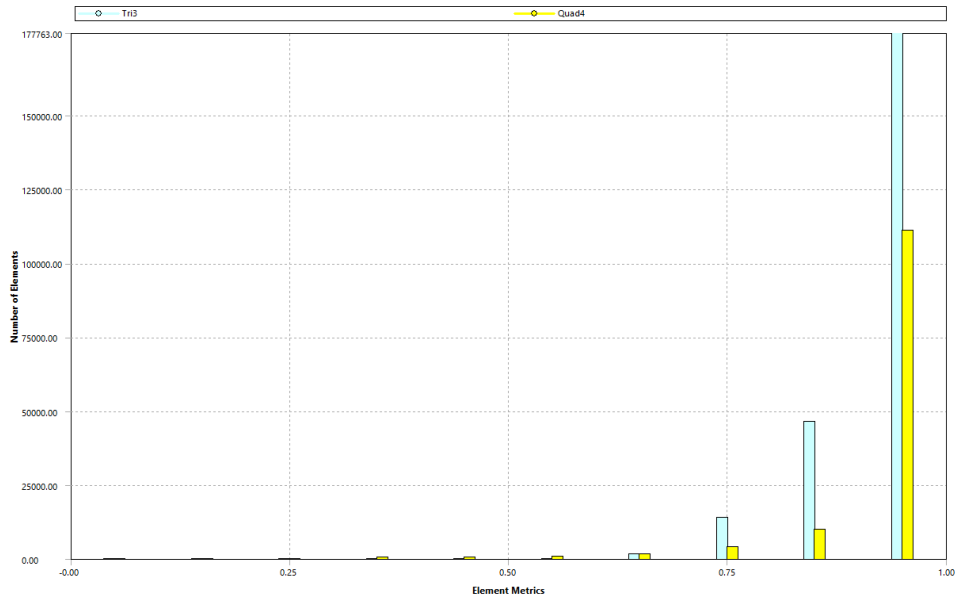


a)

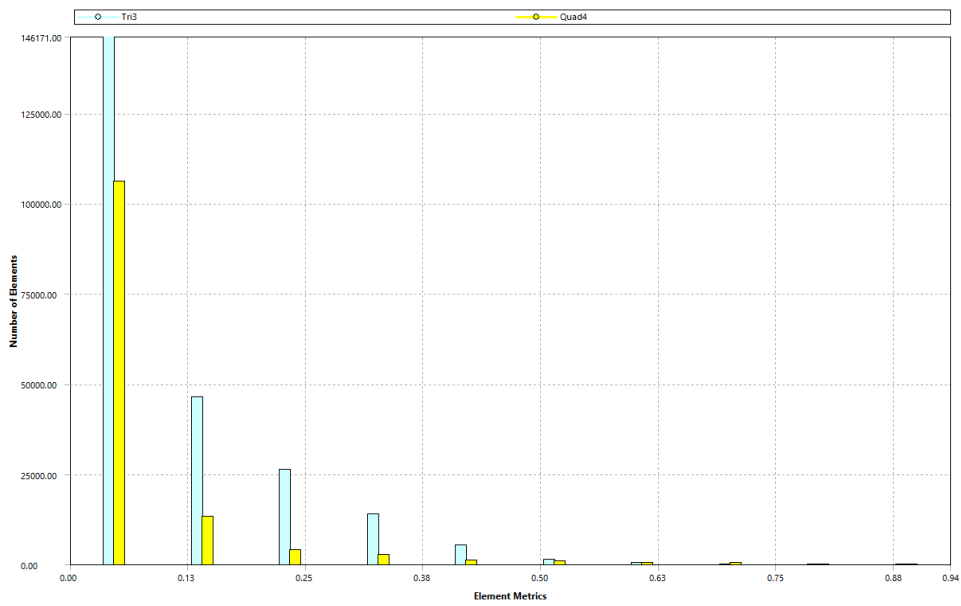


b)

Figure B 3. a) Boundary conditions and b) final mesh considered for the S2 profile with a total of $\approx 370,000$ elements, $y^+ = 10$, average element quality = 0.94, and average skewness = 0.09.



a)



b)

Figure B 4. Mesh metrics for the rime S2 profile: a) Element Quality, and b) Cells Skewness.